IMPACT OF UPPER TROPOSPHERIC JET-FRONT SYSTEMS ON THE MESOSCALE STRUCTURE OF THE TROPOPAUSE INVERSION LAYER AND CROSS-TROPOPAUSE TRANSPORT

Dissertation
zur Erlangung des Grades
„Doktor der Naturwissenschaften“
am Fachbereich Physik, Mathematik und Informatik
der Johannes Gutenberg-Universität
in Mainz

THORSTEN KALUZA
geboren in Heilbronn

Mainz, Juni 2021

ABSTRACT

The tropopause represents the transition region between the first two layers of the atmosphere, i.e., the troposphere and the stratosphere. It can be regarded as a quasi-permeable transport barrier that allows exchange and mixing of air only for certain processes. Such non-conservative processes cause material changes in the potential vorticity, a fluid-dynamic conservation property for air parcels that are generally approximated as closed thermodynamic systems. Thus, the transition from characteristic tropospheric to stratospheric potential vorticity and vice vera is equatable with transport of air through the tropopause. The significance of dynamic instability and turbulence as a non-conservative mixing process varies depending on the underlaying synoptic situation. In this context, the role of the tropopause inversion layer is not finally understood. This layer is defined based on a local maximum in static stability, a quantity which to a large degree determines the vertical distribution of potential vorticity in the tropopause region. On one hand, much of what is known about the tropopause inversion layer and its relation to the dynamic stability of the flow is based on numerical model studies where the results depend significantly on the degree of idealization as well as on the representation of the physical processes that induce dynamic instability. On the other hand, there is a lack of high resolution in situ measurements specifically dedicated to the investigation of the relation between troposphere-stratosphere exchange and the tropopause inversion layer, and thus, also the validation of the numerical models. The present work adresses this issue with the central aim to investigate mixing processes at the tropopause, particularly in relation to the tropopause inversion layer. For this a set of analyses on different spatial and temporal scales is performed. The analyses range from individual case studies based on measurements from the airborne research campaign WISE that took place during 2017 over the North Atlantic, to model-based process studies of baroclinic life cycles, up to climatological scales based on ten years of northern hemispheric reanalysis data.

The analyses across all scales reveal that turbulent mixing occurs particularly in regions which are characterised by a pronounced tropopause inversion layer. The underlaying dynamic instability is forced by a layer of strong vertical wind shear which is located closely above the tropopause. On synoptic scales the wind shear layer and the tropopause inversion layer emerge simultaneously in ridges of baroclinic waves. Furthermore, each layer exhibits a distinct mesoscale variability which is linked to differences in the mechanisms that influence the evolution of each layer. The wind shear layer as a tropopause-based phenomenon occurs on global and climatological scales. For latitudes that are not dominated by baroclinic wave dynamics, several regions have been identified that favor the occurrence of strong wind shear near to the tropopause: Over the Asian continent and associated with the subtropical jet stream, over the Indian Ocean and associated with the Asian summer monsoon circulation, and over the maritime continent and associated with the El Niño Southern Oscillation ocean–atmosphere coupling.

The occurrence of the tropopause wind shear layer is associated with low Richardson numbers in the lower stratosphere, and thus, an increased potential for dynamic instability. In the midlatitudes these preconditions for turbulent mixing occur in regions of high tropopause altitudes like ridges of baroclinic waves, i.e., a region that has gained comparatively little attention in the context of research on stratosphere-troposphere exchange. The vertically confined occurrence of the tropopause wind shear layer within the first 1–2 kilometers above the local tropopause indicates a relation to the extratropical transition layer. The extratropical transition layer is defined based on distinct trace gas gradients which are shaped by mixing processes, and its occurrence is limited to the same vertically confined region. Furthermore, the analysis highlights the significance of the mesoscale variability of both static stability and wind shear, despite the global scale and climatological character of the tropopause inversion layer and the wind shear layer.

In summary, the analysis narrows down the significance of shear-induced turbulent mixing in the lower stratosphere. The preconditions for local small-scale turbulent mixing in the tropopause region are frequently met from the tropics up to high latitudes, which is associated with the dominant tropospheric large scale dynamics within each meridional region. This in turn affects the chemical composition of the tropopause region which can have a significant impact on the global radiative budget.

ZUSAMMENFASSUNG

Die Tropopause bildet die Grenzregion zwischen den beiden untersten Atmosphärenschichten, der Troposphäre und der Stratosphäre. Sie kann als quasipermeable Transportbarriere betrachtet werden, durch die durch das Auftreten gewisser Prozesse Austausch stattfinden kann. Entsprechende nicht-konservative Prozesse bewirken materielle Änderungen der potenziellen Vortizität, einer fluid-dynamischen Erhaltungsgröße für Luftpakete die als abgeschlossene Systeme betrachtet werden können. Die Änderung der potenziellen Vortizität von charakteristisch troposphärisch zu stratosphärischen Werten und vice versa ist daher gleichzusetzen mit Transport durch die Tropopause. Die Signifikanz von dynamischer Instabilität und Turbulenz als nicht-konservativer Mischungsprozess variiert dabei abhängig von der synoptischen Situation. Die Funktion der Tropopauseninversionsschicht ist in diesem Kontext nicht abschließend erforscht. Die Tropopauseninversionsschicht ist über ein lokales Maximum der statischen Stabilität definiert, welches in die Berechnung der potenziellen Vortizität einfließt und somit deren vertikale Verteilung in der Tropopausenregion dominiert. Bisherige Erkenntnisse bezüglich dem Zusammenhang zwischen der Tropopauseninversionsschicht und der dynamischen Stabilität basieren zum einen auf numerischen Modellstudien deren Ergebnisse maßgeblich vom Idealisierungsgrad abhängen, sowie der Repräsentation der physikalischen Prozesse welche dynamische Instabilität bedingen. Zum anderen mangelt es an hochaufgelösten Messungen die dezidiert auf den Zusammenhang zwischen Stratosphären-Troposphären Austausch und der Tropopauseninversionsschicht abzielen und somit auch auf die Validierung der Modellprognosen. Die vorliegende Arbeit setzt an diesem Punkt an mit dem Ziel Mischungsprozesse von Luftmassen an der Tropopause und insbesondere die Rolle der Tropopauseninversionsschicht zu untersuchen. Dafür werden Analysen auf verschiedenen Raum- und Zeitskalen durchgeführt. Dies umfasst Fallstudien während der 2017 über dem Nordatlantik durchgeführten flugzeuggetragenen Messkampagne WISE, Modelldaten-basierte Prozessstudien barokliner Lebenszyklen, sowie eine klimatologische Betrachtung über zehn Jahre auf der Nordhemisphäre.

Die Analysen über alle Skalen zeigen dass turbulentes Mischen von troposphärischer und stratosphärischer Luft in den mittleren Breiten insbesondere in Regionen auftritt welche durch eine stark ausgeprägte Tropopauseninversionsschicht charakterisiert sind. Die dem Mischungsprozess zugrunde liegende dynamische Instabilität wird forciert durch eine Schicht stark ausgeprägter

Windscherung unmittelbar über der Tropopause. Auf synoptischer Skala entstehen die Windscherungsschicht und die Tropopauseninversionsschicht systematisch zeitgleich in Rücken barokliner Wellen. Beide Schichten weisen eine ausgeprägte individuelle mesoskalige Variabilität auf, was auf Unterschiede in den einflussnehmenden Prozessen zurückgeführt werden kann und letztendlich erheblichen Einfluss auf die dynamische Stabilität der unteren Stratosphäre hat. Die Windscherungsschicht als ein Tropopausen-basiertes Phänomen tritt auf globaler und klimatologischer Skala auf. Für geographische Breiten welche nicht von barokliner Wellendynamik dominiert sind, wurden bevorzugte Regionen für das Auftreten von ausgeprägter Windscherung in der Tropopausenregion identifiziert: Über dem asiatischen Kontinent und in Zusammenhang mit dem subtropischen Jetstream, über dem Indischen Ozean und im Zusammenhang mit der großskaligen Zirkulation des asiatischen Sommermonsuns, sowie über dem Maritimen Kontinent und im Zusammenhang mit der Phase der El Niño Southern Oscillation.

Das Auftreten der Windscherungsschicht geht einher mit niedrigen Richardson Zahlen in der unteren Stratosphäre und somit einem erhöhten Potenzial für das Auftreten von dynamischer Instabilität. In den mittleren Breiten treten diese Voraussetzungen für turbulentes Mischen in Regionen mit hohen Tropopausen wie in Rücken von baroklinen Wellen auf, und somit in einer Region die bisher nicht im Fokus der Erforschung von Stratosphären-Troposphären Austausch stand. Das lokale Auftreten der Windscherungsschicht und des damit asoziierten Mischungsprozesses im Bereich von 1–2 Kilometern über der Tropopause weist auf eine Verbindung zur extratropischen Mischungsschicht hin. Diese wird durch Spurengasgradienten definiert welche von Mischungsprozessen geprägt sind und im selben Höhenbereich auftreten. Des Weiteren hebt die Analyse die Relevanz der mesoskaligen Variabilität von Tropopausen-basierten Maxima der statischen Stabilität und Windscherung hervor, trotz des globalen und klimatolgischen Charakters der Tropopauseninversionsschicht und der Windscherungsschicht.

Zusammenfassend wurde die Relevanz von scherungsinduziertem turbulenten Mischen in der unteren Stratosphäre näher eingegrenzt. Die Voraussetzungen für lokales kleinskaliges turbulentes Mischen in der Tropopausenregion sind von den Tropen bis zu hohen Breiten auf globaler und klimatologischer Skala gegeben, und stehen im Zusammenhang mit der dominierenden großskaligen troposphärischen Dynamik in den jeweiligen Breitengraden. Dies wiederum hat Auswirkungen auf die lokale Zusammensetzung der Luftmassen in der Tropopausenregion, mit potenziell nicht zu vernachlässigendem Einfluss auf das globale Strahlungsbudget.

CONTENTS

1 INTRODUCTION 1
  1.1 Current understanding of the tropopause region 1
    1.1.1 The tropopause and cross-tropopause transport 1
    1.1.2 The extratropical transition layer 5
    1.1.3 The tropopause inversion layer 7
    1.1.4 Turbulence in the tropopause region in the context of the planetary circulation 10
  1.2 Central questions and outline of this thesis 15
2 DATA AND METHODS 19
  2.1 The ECMWF Integrated Forecast System 19
    2.1.1 IFS versions, key features and physical parametrisation schemes 19
    2.1.2 Representation of thermodynamic UTLS features in the IFS 24
  2.2 The 2017 WISE campaign 26
  2.3 Analysis Methods 29
3 OBSERVATION OF SHEAR INDUCED MIXING IN NORTH ATLANTIC BAROCLINIC WAVES 31
  3.1 Shear induced mixing in a ridge of a baroclinic wave: WISE RF07 32
    3.1.1 Synoptic situation from 27 to 29 September 2017 over the North Atlantic 32
    3.1.2 Identification of small scale mixing above the tropopause during WISE RF07 on 28 September 2017 34
    3.1.3 Observation-based estimate of the depth of the mixing layer on the basis of a Kelvin-Helmholtz instability 42
  3.2 Small scale internal mixing within the TIL: WISE RF12 44
    3.2.1 The synoptic situation during WISE RF12 45
    3.2.2 Atmospheric flow properties in the ExTL during WISE RF12 and in IFS data 46
  3.3 Summary 48
4 COMPOSITE ANALYSIS OF THE TROPOPAUSE INVERSION LAYER AND THE TROPOPAUSE SHEAR LAYER IN EXTRATROPICAL BAROCLINIC WAVES 53
  4.1 Cyclone tracking and compositing method 54
  4.2 An exemplary analysis of a sequence of case studies 57
    4.2.1 Baroclinic life cycle with LC2 characteristics 57

4.2.2 Baroclinic life cycle with LC1 characteristics 61
4.3 Composite analysis of UTLS flow features 65
4.4 Summary 69
5 A 10 YEAR NORTHERN HEMISPHERE CLIMATOLOGY OF THE TROPOPAUSE WIND SHEAR LAYER 73
5.1 The ERA5 reanalysis and data handling 74
5.2 Exemplary single day analysis, 11 September 2017 75
5.3 Ten year climatology of strong vertical wind shear 77
5.3.1 Rossby waves and the tropopause wind shear layer . . . 82
5.3.2 The shear layer at the subtropical jet stream 88
5.3.3 Strong vertical wind shear at the tropical easterly jet . . 90
5.3.4 The Pacific winter Walker circulation cell 90
5.4 Summary 92
6 CONCLUSIONS AND OUTLOOK 99
6.1 Conclusion 99
6.2 Outlook 104
A SUPPLEMENTARY INFORMATION FOR CHAPTER 3 107
A.1 Geometric estimation of the Kelvin Helmholtz billow dimension 107

BIBLIOGRAPHY 111

List of Figures 125
List of Tables 138
Acronyms 139
Physical Symbols 142
List of Publications 144
Acknowledgements 146

1

INTRODUCTION

1.1 CURRENT UNDERSTANDING OF THE TROPOPAUSE REGION

The upper troposphere lower stratosphere (UTLS) region is the transition zone between the well mixed troposphere and the stably stratified stratosphere. It is roughly defined as the vertical region from 5 to 20 km altitude and spans from the tropics to each pole with, however, distinct differences between the tropics (Fueglistaler et al., 2009) and the extratropics (Gettelman et al., 2011). A central part of the UTLS is the so called tropopause, which can be regarded as a partly permeable transport barrier between the troposphere and the stratosphere (Hoinka, 1997). The tropopause can be regarded as a quasi two-dimensional layer where gradients of fluid-dynamical, thermodynamical and chemical variables are largest. Occasionally, transport occurs through the tropopause which is termed as cross-tropopause transport or stratosphere-troposphere exchange (STE). In the extratropics this transport is bidirectional (Holton, 1995; Stohl et al., 2003). STE is the consequence of the interplay of dynamical and thermodynamical processes at the tropopause and has consequences not only on the local trace species abundance but also on the global distribution of these species with potential effects on air quality (Zanis et al., 2003, e.g.,) and climate (Forster and Shine, 1997; Nowack et al., 2018; Banerjee et al., 2019). The dynamics leading to STE occur on a variety of scales and to fully understand the underlying processes it is required to study planetary to mesoscale dynamic features. Allthough the importance of STE is known since the 1960s' (e.g., Danielsen, 1968) with substantial effort undertaken in the following decades, many processes at the smaller scales are still only understood partially. This issue can be overcome trough synergistic approaches using high resolution observations at the tropopause in combination with fine resolution model data. Such an approach is undertaken in this thesis to study the occurrence of STE in the extratropics, particularly within baroclinic waves and due to associated sub-synoptic dynamical processes.

1.1.1 *The tropopause and cross-tropopause transport*

The tropopause is the central feature of the UTLS and can be regarded as a two dimensional layer, with different definitions based on gradients of fluid-

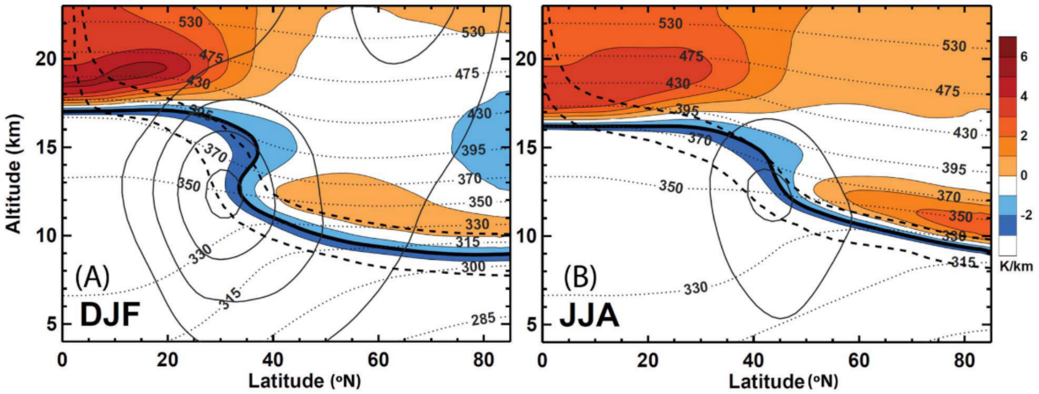

Figure 1.1: Schematic of the northern hemispheric UTLS and its key features, adopted from Gettelman et al. (2011). Seven year temporal and zonal average (2002–2008), a) Winter (DJF), and b) summer (JJA) season. Color contour shows vertical temperature gradient ($\partial T/\partial z$, in steps of 0.5 K km^{-1}). The solid black line indicates the location of the LRT, and the dashed black lines the dynamic tropopause based on the PV threshold values 2 pvu and 6 pvu. Dotted black lines show isentropes, and solid thin black lines zonal mean zonal wind (u, in steps of 10 m s^{-1}). Data basis for the thermal structure are GPS radio occultation (RO) measurements, PV and wind are derived from ECMWF ERA Interim reanalysis fields

dynamical properties in the region where it occurs. The World Meteorological Organization (WMO, 1957) defines the lapse rate tropopause (LRT) through a threshold of the lapse rate Γ, which is defined as $\Gamma = -\frac{\partial T}{\partial z}$, i.e., the negative gradient of the air temperature T with altitude z. The LRT is defined as the first level above the surface where Γ falls below 2.0 K km^{-1} with the condition that its mean value remains below this threshold between this level and all higher levels within 2 kilometer above. Another approach is the definition of the dynamic tropopause, which is based on the potential vorticity and its conservation properties. The dynamic tropopause can be defined through the maximum of the isentropic gradient of the potential vorticity (PV, Kunz et al. (2011)), or more commonly through a threshold value within the region of enhanced PV gradients (Hoskins et al., 1985). Following the definition of Ertel (1942) the PV can be written as

$$Q = \frac{1}{\rho}\vec{\eta} \cdot \vec{\nabla}\Theta, \qquad (1)$$

where ρ is the density of the medium, $\vec{\eta} = \vec{\nabla} \times \vec{u} + 2\vec{\Omega}$ the vector of the absolute vorticity $\vec{\eta}$ which is composed of the rotation of the three dimensional wind field $\vec{u}$ and the vector of the angular velocity of the earth $\vec{\Omega}$. The term $\vec{\nabla}\Theta$ is the gradient of the potential temperature

$$\Theta = T\left(\frac{p_0}{p}\right)^{\frac{R_d}{c_p}}, \tag{2}$$

with the temperature T, the pressure p and a reference pressure $p_0 = 1000$ hPa, the specific gas constant for dry air $R_d = 287.06$ J kg^{-1} K^{-1} and the specific heat capacity $c_p = 1004.5$ J kg^{-1} K^{-1}. The natural unit for the PV is the 'potential vorticity unit' (pvu), where 1 pvu equals 10^{-6} m^2 s^{-1} K kg^{-1}.

The definition of the LRT is motivated by the fact that the troposphere on average exhibits a vertical temperature gradient above the threshold $\Gamma = 2.0$ K km^{-1}, which allows the occurrence of convection and vertical stirring. The stratosphere is characterised by increasing temperatures with altitude, which inhibits vertical motion, and the sudden change in the lapse rate profile at the tropopause acts as a barrier between the two atmospheric layers. The dynamic tropopause on the other hand presents a more general transport barrier, which is due to the conservation properties of the PV. The material derivative of the PV is given by (Hoskins et al., 1985)

$$\frac{D}{Dt}Q = \frac{1}{\rho}(\vec{\eta}\cdot\frac{D\Theta}{Dt} + \vec{\nabla}\times\vec{F}\cdot\vec{\nabla}\Theta), \tag{3}$$

where the vector $\vec{F}$ denotes non-conservative forces, i.e., frictional, diffusive and turbulent processes. Thus, the PV of an air parcel is materially conserved in the absence of non-conservative forces and diabatic heating $D\Theta/Dt$, i.e., for adiabatic frictionless flow. The tropopause region is characterised by pronounced PV gradients which separate the troposphere with characteristic low PV from the stratosphere with characteristic high PV. Adiabatic and frictionless motion is a good first order approximation for atmospheric flow outside the boundary layer, therefore the dynamic tropopause is regarded as an efficient transport and mixing barrier.

PV is conserved to a large degree in the tropopause region, however, observational evidence exists that STE must occur to explain the trace species structure in the UTLS. Cross tropopause transport pathways can generally be classified into two groups. First, 'adiabatic' or 'quasi-isentropic' eddy-driven exchange through transport along isentropes that cross the tropopause and subsequent diffusive dissolution of the gradients, e.g. across the so-called middleworld which is defined based on isentropic surfaces that intersect with the tropopause (Fig. 1.1). The second group comprises 'diabatic' or 'cross-isentropic' mixing, where the exchange occurs locally at the tropopause through diabatic and non-conservative PV modification which results in a reassignment of tropospheric air to stratospheric air and vice versa. The relevance of these processes varies with the underlying synoptic situation.

Tubulence is a central non-conservative process that can effectively modify the PV of an air parcel in the tropopause region and thus, result in STE. The turbulent breakdown of flow results in an effective diffusive transport of momentum, heat and chemical constituents across background gradients. The diffusion of momentum modifies the vorticity of an air parcel, and the diffusion of heat equivalently the stratification, which can result in a material change of the PV of an air parcel. Recently, Spreitzer et al. (2019) provided evidence of the significance of non-conservative processes for PV modifications at the tropopause in a baroclinic life cycle case study, using the integrated forecast system (IFS) from the European Centre for Medium-Range Weather Forecast (ECMWF). Based on temperature and wind tendencies from physical parameterizations for large scale and convective clouds, radiation as well as vertical turbulence the authors showed that all of these processes contribute to PV modifications at the tropopause, with varying significance depending on the region within the baroclinic wave and its evolution stage. In particular, vertical and lateral shear-induced turbulent diffusion was identified as the dominating process for the erosion of a PV streamer downstream of the ridge, which agrees with observational studies (Danielsen, 1968; Shapiro, 1976, 1980). Furthermore, they identified turbulent diffusion associated with enhanced wind shear above the anticyclonic shear side of the jet streak as a significant contributor to STE, resulting in an effective lifting of the tropopause at above average tropopause altitudes in the ridge of the baroclinic wave. The regions of enhanced wind shear above the jet streak are susceptible to the generation of shear induced turbulence which has been observed e.g. by Whiteway et al. (2004) and Duck and Whiteway (2005). Numerical model-based research studies indicate that the occurrence of turbulence in this region is generally associated with the generation of gravity waves on different scales and their interaction with the background wind shear profile (Trier et al., 2020).

STE through diabatic heating can be achieved by radiative energy transfer which has been observed by (Zierl and Wirth, 1997), or the release of latent heat during cloud formation (Gray, 2006). Furthermore, convective injection of tropospheric air into the stratosphere can lead to STE (Homeyer et al., 2014).

STE is best analysed using Lagrangian methods (Wirth and Egger, 1999). A comprehensive STE climatology has been compiled by Škerlak et al. (2014) based on extensive trajectory calculations and ERA-Interim reanalysis data. This study manifests previous findings that STE occurs in several hotspot regions, i.e., the storm track regions over the North Atlatnic and the North Pacific, the Southern Ocean and the mountain chains in the subtropics. More so, also using a Lagrangian approach, Hoor et al. (2010) identified different time scale regimes for trajectories that cross the tropopause, revealing a vertical confined tropopause-following mixing layer, which is characterised by comparatively fast diabatic STE and subsequent dispersion within the layer.

1.1.2 *The extratropical transition layer*

The UTLS is a region where several trace species such as ozone (O_3), nitrous oxide (N_2O) or carbon monoxide (CO) show large vertical gradients (Fig. 1.2). This is the result of the regionally and seasonally varying strength of chemical source regions, chemical processing, photochemical production and removal, and transport and mixing, which results in characteristic lifetimes, and thus, characteristic vertical profiles for individual trace gasses. The transition from tropospheric to stratospheric trace gas mixing ratios at the tropopause contains information about the efficiency of the tropopause as a transport and mixing barrier and about the occurrence of STE. A common method of analysing high resolution trace gas mixing ratio measurements is to correlate the time series of a trace species with main sources in the troposphere and sinks mainly in the stratosphere (e.g., N_2O or CO) with a characteristic stratospheric trace species, i.e. with main sources in the stratosphere and sinks in the troposphere (e.g., O_3) (Fischer et al., 2000). In the absence of mixing between the two constituents, such tracer-tracer correlations form a characteristic L-shape, which connects the tropospheric slope with the stratospheric slope at the tropopause. The effect of STE and mixing manifests itself in the form of 'mixing lines' in the tracer-tracer correlation, which connect tropospheric and stratospheric air through branches that deviate from the L-shape at different starting points and slopes. The analyses of airborne mixing ratio measurements of trace gas species like ozone (O_3), carbon monoxide (CO), water vapour (H_2O) and nitrous oxide (N_2O) at midlatitudes revealed a quasi-ubiquitous, tropopause-following transition zone, which is characterised by mixing lines in the tracer-tracer space, and which defines a three-dimensional extratropical transition layer (ExTL, Hoor et al., 2002; Hoor et al., 2004; Pan et al., 2004; Hegglin et al., 2009).

The ExTL is an inherent feature of the lowermost stratosphere (LMS, Holton, 1995), a subregion of the extratropical lower stratosphere which extends from the tropopause up to the isentropic surface that corresponds with the tropical tropopause, i.e. $\Theta = 380$ K (Fig. 1.1). However, the ExTL exhibits a sharp upper edge, which separates it from the remainder of the LMS. The analysis of CO profiles in a tropopause-relative vertical coordinate system revealed a distinct 'kink' above the tropopause (Hoor et al., 2002), indicating a discontinuity in the transport and mixing efficiency of tropospheric CO into the lower stratosphere. Hoor et al. (2004) found the ExTL to cover the region

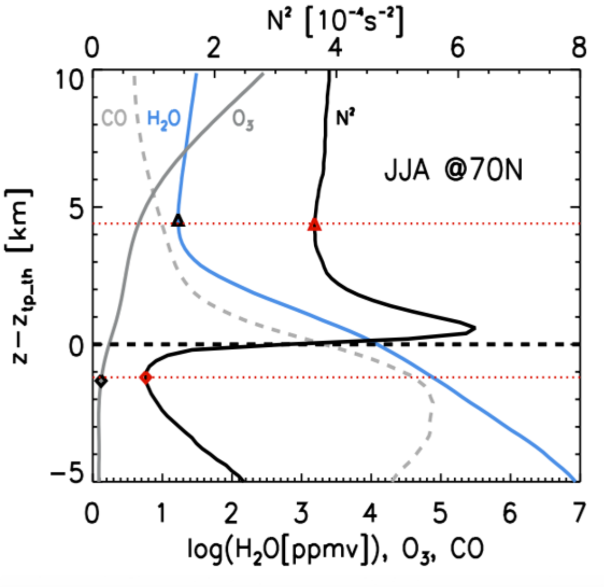

Figure 1.2: Zonal mean tropopause based averaged vertical profiles for JJA at 70° N, adopted from Hegglin et al. (2009). LRT relative vertical coordinate. Black line shows static stability (N^2, in 10^{-4} s^{-2}), blue line H_2O mixing ratio (ppmv, logarithmic as indicated), solid grey line O_3 (ppmv), and dashed grey line CO (ppmv, factor 20). For further details see Hegglin et al. (2009).

around the dynamic tropopause and to be limited to altitudes up to about 30 K above the local dynamic tropopause. In geometric space this translates to a distance of about 2–3 km from the local LRT (Pan et al., 2004). The ExTL as a global scale feature was analysed by Hegglin et al. (2009), who used CO-O_3 and H_2O-O_3 tracer-tracer correlations derived from Atmospheric Chemistry Experiment Fourier Transform Spectrometer (ACE-FTS) satellite data. The ExTL features derived from the two different tracer sets showed a general agreement outside of the tropics, with an increasing ExTL depth towards higher latitudes, and a weak seasonality characterised by a higher upper edge of the transition layer during summer and autumn in agreement with the findings from Hoor et al. (2004).

The chemical definition of the ExTL through tracer-tracer correlations is not unambiguous as it depends on the set of tracer species used and their conservation properties in the tropopause region. Hegglin et al. (2009) discuss differences between the analyses based on CO-O_3 and H_2O-O_3 tracer-tracer correlations due to the temperature dependency of the water vapour mixing ratio, as well as the limited chemical lifetime of CO particularly at the tropical tropopause. A generalisation of the location and extent of the chemically defined ExTL should therefore be considered with care, as the results from the multi-model and multi-measurement comparison study by Hegglin et al. (2010) show.

Berthet et al. (2007) show the existence of a vertically confined tropopause-following mixing layer in a tracer-independent approach, based on a maximum of the relative distribution of Lagrangian trajectories that crossed the tropopause within a certain time. This process-based approach was further expanded by Hoor et al. (2010), who linked the upper edge of the ExTL to a sharp change of the transport time scale regime, based on Lagrangian trajectories that entered the the stratosphere within less than 50 days, which is short compared to the transport timescales into the LMS above the ExTL.

A variety of known diabatic STE processes contribute to the formation and maintenance of the ExTL, i.e. shear induced turbulence within PV streamers (Škerlak et al., 2015) below the jet stream (Danielsen, 1968; Shapiro, 1980) as well as above the wind maximum (Whiteway et al., 2004; Duck and Whiteway, 2005), PV modification due to radiation (Zierl and Wirth, 1997) and due to latent heat release during cloud formation (Gray, 2006), as well as convective injection (Homeyer et al., 2014). Numerical models are able to reproduce central features of the ExTL (Konopka and Pan, 2012), i.e. a deep transition layer on the cyclonic shear side of the jet within baroclinic waves (e.g., Schäfler et al., 2021), as well as a comparatively sharp chemical transition on the anticyclonic shear side (Pan et al., 2007). Spreitzer et al. (2019) show that the significance of the diabatic processes varies strongly depending on the region within the baroclinic wave as well as its temporal evolution stage. They furthermore confirm the significance of turbulence concerning the overall STE budget.

Turbulence occurs as a result of dynamic instability, which can occur when vertical shear of the horizontal wind overcomes the stabilising effect of a stably stratified flow. The following subsection first gives an overview of the stratification in the tropopause region, its variability, and the processes responsible. Afterwards, Section 1.1.4 will revert to the concept of dynamic instability, and discuss the occurrence of enhanced wind shear and the resulting potential for turbulence in the tropopause region.

1.1.3 *The tropopause inversion layer*

The thermal definition of the tropopause builds upon an inversion of the vertical temperature gradient. This inversion is a global climatological feature (Birner, 2006), which however varies strongly in its strength and occurrence on a large spectrum of spatial and temporal scales (Pilch Kedzierski et al., 2015; Gettelman and Wang, 2015). The climatological maximum in the vertical temperature gradient $\partial T/\partial z$ above the LRT as well as its seasonality are indicated in Fig. 1.1. The tropopause inversion layer (TIL, Birner et al., 2002) is commonly defined on the basis of the resulting localised maximum in the vertical profile of the static stability (Fig. 1.2)

$$N^2 = \frac{g}{\Theta} \cdot \frac{\partial \Theta}{\partial z}, \tag{4}$$

with g being the gravitational acceleration. The static stability N^2 is also refered to as the Brunt-Väisälä frequency, which defines the oscillation frequency of a vertically displaced air parcel in a stable background stratification. The TIL represents a maximum in static stability and as such strongly damps vertical motion. However, the interrelation between the TIL and the ExTL as inherent features within the LMS is complex (Hegglin et al., 2009; Schmidt et al., 2010; Kunkel et al., 2016) and an ongoing topic of research. The complexity arises from the broad spectrum of processes that are involved in the formation and maintenance of both the TIL and the ExTL on different temporal and spatial scales, as well as due to the bidirectional influence. The following paragraphs present an overview of the processes that are known to affect the evolution of the TIL, ordered from large to small scales.

The downwelling motion of the stratospheric residual circulation as part of the Brewer-Dobson circulation during winter results in a temporally lagged large scale positive forcing on the lower stratospheric static stability (Birner, 2010; Wargan and Coy, 2016). The opposing vertical gradients of water vapour and ozone that maximise at the tropopause (also referred to as the hydropause and ozonopause) sharpen the vertical temperature profile around the tropopause on a large scale due to a resulting dipole radiative forcing (Randel et al., 2007), where seasonal, meridional and local variations in the mixing ratios result in a varying sharpening effect at the tropopause (Hegglin et al., 2009). Kunz et al. (2009) identified particularly the water vapor gradients to contribute significantly to the maintenance of the TIL. These processes substantially influence the large scale seasonality of the TIL. At polar latitudes for example, the TIL is significantly more pronounced during summer compared to the winter months (Birner, 2006; Randel et al., 2007), which agrees with the enhanced radiative forcing and enhanced tropospheric water vapour mixing ratios, and the resulting tropopause sharpening mechanism.

Baroclinic waves at midlatitudes influence the TIL on a synoptic scale, in accordance with the horizontal extent of these eddies, as well as on time scales of several days in accordance with their life time. Wirth (2004) identify a dynamic sharpening mechanism of the lower stratospheric temperature profile, based on the dominating term in the material change rate of the static stability N^2 for large horizontal scales and vertical scales below the associated scale height of the atmosphere:

$$\frac{DN^2}{Dt} = -N^2 \frac{\partial w}{\partial z}. \tag{5}$$

Thus, the vertical divergence of the vertical wind in upper tropospheric cyclones respectively the vertical convergence in anticyclones results in a synoptic scale dipole forcing of TIL strength enhancement in ridges and TIL strength weaking in troughs, which agrees with the results from idealised dry numeric simulations (Wirth, 2003; Wirth and Szabo, 2007). The breaking of baroclinic waves furthermore results in a persistent TIL evident in the zonal mean (Erler and Wirth, 2011).

The sub-synoptic scale appearance of the TIL is further modulated by processes on the mesoscale. Wirth and Szabo (2007) showed that these variations are already evident in simulations of dry barolinic wave experiments. Kunkel et al. (2014) discuss how inertia gravity waves emitted in jet exit regions in ridges of baroclinic waves have a transient effect on the TIL strength distribution, and how they also can persistently alter the thermal structure in the tropopause region if wave capture or turbulent breakdown occurs (Bühler and McIntyre, 2005; Plougonven and Snyder, 2005). Observational evidence for the interaction between the TIL and inertia gravity waves has been provided by Zhang et al. (2015, 2019), using spectral decomposition of radiosonde measurement perturbations from a background state. They find the TIL to inhibit upward propagation of tropospheric gravity waves, and at the same time as possibly being a source for stratospherically generated upward propagating gravity waves. Diabatic processes have a significant influence on the TIL evolution during baroclinic life cycles (Kunkel et al., 2016). Regions of enhanced static stability in the lowermost stratosphere emerge above strong tropospheric updrafts, such as convection or warm conveyor belts, due to vertical divergence of the vertical wind and the resulting convergence of the isentropes in the LMS. Furthermore, the associated occurrence of clouds in the regions of the updrafts have a radiative impact on the TIL. The water vapour transport and cloud formation associated with the updrafts which reach up to the LRT cause radiative cooling below the LRT, resulting in a stronger temperature inversion at the tropopause.

The occurrence of turbulence in the tropopause region results in a diffusive heat and momentum flux which works towards an erosion of the shear forces that cause the turbulence, as well as towards an adiabatic thermal stratification. Kunkel et al. (2016) identify an overall reduced TIL strength and variability in idealised baroclinic life cycle simulations with an active turbulence parametrisation.

The superposition of these various processes which are additionally often interrelated leads to the spatially and temporally variable occurrence of the TIL. Especially in the extratropics a substantial sub-synoptic scale variability is evident in the regions of baroclinic waves as a result of the complex interaction between dynamic and thermodynamic processes as outlined above.

1.1.4 *Turbulence in the tropopause region in the context of the planetary circulation*

Turbulence was introduced as a non-conservative process that can significantly contribute to the overall STE budget, due to the fact that it can materially alter the PV of an air parcel. The tropopause is defined based on a sudden increase in static stability, and thus, turbulence in this region is generally associated with dynamic instability within stably stratified shear flow. The following paragraphs first recapitulate the concept of dynamic instability as the central mechanism responsible for the occurrence of turbulence in the tropopause region. Following this, an overview of flow conditions that favour the evolution of dynamic instability is presented, from the planetary circulation down to small scale wave perturbations that eventually result in turbulence and STE.

1.1.4.1 *Dynamic instability and turbulence*

According to linear wave theory, the dynamic stability of the flow can be evaluated on the basis of the non-dimensional Richardson number

$$Ri = \frac{N^2}{S^2}, \tag{6}$$

which is defined as the ratio between static stability N^2 and vertical shear of the horizontal wind S^2. The vertical shear of the horizontal wind is defined as

$$S^2 = \left(\frac{\partial u}{\partial z}\right)^2 + \left(\frac{\partial v}{\partial z}\right)^2, \tag{7}$$

i.e., the squared vertical gradient of the horizontal wind components u and v. Throughout this work, vertical shear of the horizontal wind will be referred to as vertical wind shear. The Richardson number describes the ratio between the suppression of turbulent kinetic energy due to buoyancy and the production of turbulent kinetic energy due to shear forces. Dynamic instability in stably stratified flow can occur when the shear forces prevail, resulting in Richardson numbers below a critical threshold of $Ri_c = 1/4$ (Miles, 1961). A descriptive example is the Kelvin-Helmholtz instability (KHI), where the shear induced shift of a vertically displaced air parcel, e.g., due to a wave perturbation, results in a local convective instability in an otherwise stably stratified flow with potential wave overturning and turbulent breakdown. The resulting effect on a background scalar field is commonly assumed to approximately follow the gradient diffusion hypothesis, which states that the turbulent flux off the scalar ϕ is proportional to the mean scalar gradient, and thus, satisfies the diffusion equation

$$\frac{\partial \phi}{\partial t} = K_\epsilon \frac{\partial^2 \phi}{\partial z^2}, \tag{8}$$

with the eddy diffusivity K_ϵ (in $\mathrm{m^2 s^{-1}}$). Thus, turbulence caused by shear-induced dynamic instability acts as a diffusive transport of heat and momentum that effectively erodes the underlaying momentum and temperature gradients. From this consideration it is clear how turbulence can modify the PV and result in STE.

1.1.4.2 *The occurrence of wind shear in the UTLS region; planetary to synoptic scale*

The tropopause marks the transition from the on average weakly stably stratified troposphere with a mean static stability of the order of $\overline{N^2} = 1 \cdot 10^{-4}\ \mathrm{s}^{-2}$, to the strongly stably stratified stratosphere which is characterised by mean static stability values of the order of $\overline{N^2} = 4 \cdot 10^{-4}\ \mathrm{s}^{-2}$. The TIL is furthermore defined based on a local maximum in static stability N^2 about an order of magnitude larger than the tropospheric values. Therefore, the Richardson number criterion has two implications for the flow in the tropopause region, or rather two different viewpoints on the same issue. First, exceptional vertical wind shear is necessary for dynamic instability to emerge in the tropopause region. Second, exceptional vertical wind shear can be sustained by the stably stratified flow before the onset of turbulent erosion of the momentum gradients. The following paragraphs describe how this issue is reflected in the atmospheric circulation, with a focus on the UTLS region.

On the largest scales, the occurrence of wind shear is governed by the jet streams. These atmospheric bands of enhanced flow velocity exhibit a synoptic to planetary scale extent in flow direction of up to several thousands of kilometers, with lateral shear zones of hundreds of kilometers and vertical shear zones spanning over several kilometers. The differential solar heating between the equator and the poles due to the earths surface curvature results in a meridional temperature gradient, and the associated pressure gradient force drives equalising currents, the jet streams. Scale analysis of the physical forces involved shows that the jet stream particularly at midlatitudes can be approximated as a geostrophic wind, i.e. driven primarily by a balance between the Coriolis force and the pressure gradient force. The geostrophic wind $\vec{v}_g$ can be written as

$$\vec{v}_g = \frac{1}{f}\vec{k} \times \vec{\nabla}_p \Phi \tag{9}$$

with the Coriolis parameter f, the horizontal gradient operator $\vec{\nabla}_p$ on an isobaric surface, the geopotential $\boldsymbol{\Phi}$, and the orthogonal vertical unit vector $\vec{k}$ on the isentropic surface. Furthermore, the pressure gradient force changes with altitude, due to the baroclinicity of the atmosphere, which results in a vertical shear of the geostrophic wind that is described by the thermal wind equation.

It is derived from the vertical derivative of the geostrophic wind with respect to the atmospheric pressure, under the assumption of hydrostatic equilibrium.

$$\frac{\partial \vec{v}_g}{\partial ln(p)} = -\frac{R_d}{f}\vec{k} \times \vec{\nabla}_p T \tag{10}$$

The meridional temperature gradient between the equator and the poles is not uniform, but rather exhibits local maxima that are largely forced by large scale dynamics as well as differential heating. At midlatitudes, these maxima of baroclinicity are associated with baroclinic waves, the evolution of cyclones and anticyclones, and the emergence of localised jet streaks that are referred to as the eddy-driven or polar-front jet (PFJ). The PFJ wind speed maximum is located at around 250–300 hPa altitude, and the upper tropospheric front is associated with exceptional horizontal temperature gradients, which in turn causes enhanced vertical wind shear according to the thermal wind equation. Endlich and McLean (1965) describe a general agreement between the observed wind shear and the thermal wind shear derived from simultaneous temperature measurements, particularly for the region of the upper tropospheric front above the level of maximum wind speed. However, it should be considered that the thermal wind equation does not factor in inertial forces which can lead to a significant underestimation or overestimation of the wind shear compared to the actual wind field, depending on the curvature of the flow (Newton and Persson, 1962).

The subtropical jet (STJ) is located at lower latitudes compared to the PFJ, as well as at higher altitudes around 200 hPa. It is regarded as an inherent part of the Hadley circulation, where it is forced by the upper tropospheric equalising currents of the planetary circulation cell and the Coriolis force, the temperature gradient at the subtropical tropopause break, and by the conservation of angular momentum during the poleward migration of air masses (Holton, 1995). The STJ and the PFJ exhibit a pronounced seasonality (Koch et al., 2006), with maximum jet occurrence frequencies during winter (DJF) and minimum occurrence frequencies during summer (JJA) when the meridional temperature gradient is least pronounced. This is indicated in Fig. 1.1. The STJ and the polar jet appear as a single wind maximum in the long year zonal average, which is largely due to the variability in the occurrence frequency, latitude, and strength of the polar jet, as well as due to the fact that the two jets are not always clearly distinguishable.

The equatorial region is characterised by large scale convective upwelling and equalising upper tropospheric easterlies and westerlies, forming the Walker circulation cells. These circulation cells are influenced by large scale oscillations like the El Niño Southern Oscillation (ENSO) ocean–atmosphere coupling on yearly timescales, or the Madden Julian oscillation (MJO) on weekly to monthly timescales (Webster, 2020). During the summer months from June to September, the tropical easterly jet (TEJ) emerges as an inherent part of the East Asian summer monsoon circulation (EASM). It is defined through upper tropospheric easterlies up to maximum wind speeds around 40 ms^{-1} located at altitudes of about 150 hPa and centred above the Indian Ocean (Krishnamurti and Bhalme, 1976).

1.1.4.3 *The occurrence of wind shear in the UTLS region; sub-synoptic scale*

The large scale background wind shear provided by the planetary circulation and the jet streams is further modulated by smaller scale processes. Liu (2017) performed a spectral decomposition of wind shear features in numerical data from the NCAR Whole Atmosphere Community Climate Model (WACCM), and confirmed the importance of processes on a large spectrum of scales. On the mesoscale, flow deformation, convergence and differential temperature advection can result in the formation of frontal zones and enhanced wind shear according to the thermal wind equation (Ellrod and Knapp, 1992).

Gravity waves play an important role in the generation of dynamic instabilities. The jet exit region of tropospheric jet streaks is a common source for gravity waves as they are spontaneously emitted where the flow deviates from geostrophic balance (e.g., O'Sullivan and Dunkerton, 1995; Zülicke and Peters, 2006; Plougonven and Zhang, 2014). Fronts, shear zones and convection are features of baroclinic development, and they are another common source for gravity waves. The intrinsic frequency spectrum of the emitted waves reaches from the order of the inertial limit (inertia gravity waves, IGW) up to small high frequency waves (Zülicke and Peters, 2006). These waves can interact with the background flow in several ways (e.g., Trier et al., 2020). Wave perturbations in regions where $Ri < Ri_c$ can result in the generation of KHI and turbulence. Furthermore, turbulence can be initiated due to wave breaking at critical levels, i.e., regions where the background wind speed approaches the horizontal phase velocity of a propagating gravity wave (e.g., Dörnbrack et al., 1995). In the aviation sector this issue has gained substantial attention in the context of clear air turbulence (CAT), which is defined as turbulence that is not associated with clouds or thunderstorms. The underlaying mechanism is shear-induced dynamic instability, and throughout the history of research on it, CAT has been identified to be largely a gravity wave phenomenon (Reiter, 1964; Sharman et al., 2012).

In the tropopause region above the jet stream wind maximum, gravity waves can deform the flow that is already characterised by enhanced wind shear. Kunkel et al. (2014) performed idealised numeric simulations of dry baroclinic life cycles and showed how mesoscale gravity waves with an intrinsic frequency close to the inertial limit significantly enhance the wind shear in the tropopause region within the ridge of the baroclinic wave. Gravity waves can furthermore interact with the tropopause region, as according to linear wave theory the leap in static stability presents a maximum of the refractive index, which can result in wave refraction and a characteristic shift in the frequency spectrum, as well as partial or total wave reflection. Recently, Bense (2019) found the transmission coefficient and the shift of the wave spectrum to exhibit a rather complex dependency on the wavelength, the angle of the wave vector, the strength and depth of the TIL, and the background wind shear profile. A case study on orography-induced gravity waves furthermore showed how critical level filtering in the tropopause region resulted in a pronounced local wind shear enhancement caused by non-linear wave-mean-flow-interaction. The overall significance of this mechanism however remains to be quantified.

The superposition of the background shear associated with the jet stream and smaller scale gradient sharpening mechanisms like gravity wave perturbations or local flow convergence can result in subcritical Richardson numbers, with eventual growth of small scale perturbations due to dynamic instabilities. Turbulent breakdown then results in a homogenisation of the turbulent layer, effectively eroding vertical gradients in the momentum and potential temperature profile, and mixing trace gases across gradient structures like e.g. at the tropopause. The homogenisation of the wind profile within the turbulent layer can result in gradient sharpening in the vertically adjacent regions, which in turn can lead to a vertical succession of momentum gradients (Reiter, 1969). This consideration conceptually resembles the results of the direct numerical simulations (DNS) performed by Fritts et al. (2013) and subsequent research studies by the authors (Fritts et al., 2016, 2017). In their DNS setup, the phase relation between a large scale vertically propagating gravity wave and a static small scale background perturbation wave results in vertical regions of turbulence and gradient erosion, with adjacent gradient sharpening. Fritts et al. (2013) take up the phrase "sheet and layer" structure, with layers of reduced gradients, and sheets of enhanced gradients which exceed the background values by up to an order of magnitude. During the evolution, the sheets can become dynamically unstable as well, resulting in Kelvin-Helmholtz instabilities.

The occurrence of atmospheric processes that force wind gradient sharpening together with the fact that the flow in the tropopause region can sustain exceptional wind shear is reflected in the climatological vertical and geographic distribution of enhanced vertical wind shear. Enhanced values of S^2 in the tropopause region were described in several studies that analyse flow properties in in vertical coordinates based on the distance from the LRT. In the early research studies on the occurrence of the TIL, Birner et al. (2002) describe a sharp peak of S^2 right above the LRT, derived from tropopause-based averaged radiosonde measurement profiles at Munich (48.1° N, 11.6° W), Germany. The S^2 maximum is most pronounced during the winter months (DJF) and minimises during summer (JJA), which agrees with the results from Idaho (43.6° N, 116.2° W) from Zhang et al. (2015). Another important finding from the study by Birner et al. (2002) is the fact that the maximum in vertical wind shear is not well represented in the ECMWF ERA-Interim reanalysis data, which is mainly due to to the limited vertical resolution of the model data in the UTLS region. The analysis of a larger set of radiosonde data showed that the occurrence of enhanced vertical wind shear in the tropopause region exhibits a meridional dependency, being most pronounced in the tropics where it shows a bi-annual seasonality and maximum mean values of S^2 during JJA and DJF (Zhang et al., 2019). At polar latitudes, the mean vertical wind shear at tropopause altitudes shows no strong maximum throughout the year. The equatorial summer maximum is associated with the emergence of the TEJ during the summer monsoon months from June to September (Vasantha et al., 2002; Sunilkumar et al., 2015).

1.2 CENTRAL QUESTIONS AND OUTLINE OF THIS THESIS

This work investigates the tropopause inversion layer and its relation to atmospheric dynamics in the tropopause region, with a focus on turbulent mixing and possible consequences for the evolution and maintenance of the extratropical transition layer. Figure 1.3 shows a schematic of the relevant processes in midlatitudes, particularly in ridges of baroclinic waves, recapitulating the central information from Section 1.1.

The trace gas gradients at the tropopause define the ExTL. The interrelation between the TIL and the ExTL is in many regards bidirectional, and the cause-effect relationship is not finally understood. Several studies suggest a causal relationship between STE and the occurrence of the TIL (Kunz et al., 2009; Gettelman and Wang, 2015; Kunkel et al., 2016) based on observations and on numerical model studies. Small scale diabatic processes that influence the TIL can involve STE (Kunkel et al., 2016), and the modification of trace gas profiles and the resulting change in radiative forcing in turn can influence the TIL (Randel et al., 2007). Furthermore, the relation between the TIL and gravity waves is bidirectional, where the N^2 maximum modifies the frequency and amplitude of the waves (Bense, 2019), and the wave perturbations give rise to modifications in the temperature- and dynamic structure in the tropopause region (Kunkel et al., 2014). Eventual wave breaking and turbulent breakdown again involves mixing of air masses as well as the modification of temperature and momentum profiles (Zhang et al., 2015, 2019).

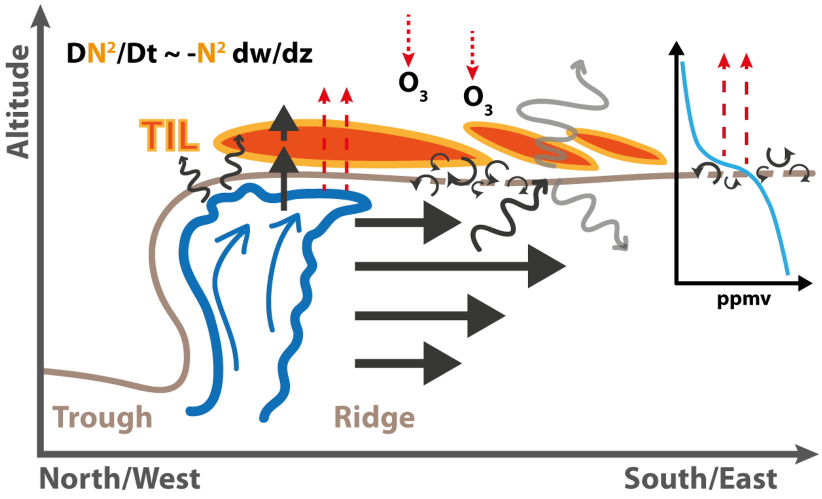

Figure 1.3: Schematic of the tropopause region in baroclinic waves, to illustrate the key processes and the central issue of this work. The TIL is indicated in orange, above the tropopause (thick silver line). The tropospheric ridge is dominated by the jet streak, large scale uplifting, and high reaching clouds. Gravity waves (emitted, reflected, refracted) are indicated as wavy arrows. Turbulence is indicated by circular arrows. An exemplary vertical profile of a tropospheric trace gas mixing ratio is shown at the right edge. Dashed (dotted) red arrows show long (short) wave outgoing (incoming) radiation. The dependency of the material change rate of N^2 on the vertical divergence of the vertical wind is stated in the top left corner.

Much of what is known about the TIL, its fine scale structure, and its relation with the ExTL is based on theoretical considerations and idealised numerical simulations. They rely on a realistic representation of e.g. non-resolved parametrised processes like turbulent diffusion, as well as on a realistic implementation of the synergy of different processes that influence the thermodynamic and chemical structure in the tropopause region. It is important to compare in-situ measurements to the theory based perception of the TIL. During the WISE measurement campaign, a number of research flights were specifically dedicated to study the chemical composition and thermodynamic structure of the tropopause region during different stages of baroclinic waves. The analysis of these in-situ measurements in the context of STE and the TIL presents a key part of this work. Therefore, the first analysis chapter focusses on the following central question:

- *How well does high resolution ECMWF IFS output represent the thermal and dynamic structure of the tropopause region in comparison to airborne observations?*

Baroclinic waves dominate the flow in the midlatitudes, and they influence the evolution of the TIL through a variety of processes on a large spectrum of scales, from adiabatic synoptic scale dynamic forcing (Erler and Wirth, 2011), down to embedded meso- and microscale processes associated e.g. with cloud formation or turbulence (Kunkel et al., 2016). Simultaneously, baroclinic waves are associated with jet streaks and a large scale background profile of enhanced wind shear, particularly in the upper troposphere, which is further modulated by smaller scale processes like e.g. gravity waves. The interrelation of these flow features defines the dynamic stability in the tropopause region, and therefore the potential for STE and mixing within baroclinic waves. Contemporary ECMWF IFS model data present a realistic representation of the atmospheric state at high temporal and spatial resolution, with the model being able to resolve key flow features in the tropopause region. One central goal of this work is to use state of the art numerical weather prediction model output to present a comprehensive analysis of the TIL evolution during baroclinic life cycles in a non-idealised setting, and in the context of the dynamic stability at the tropopause. The second analysis chapter discusses the following question:

- *Does the TIL exhibit similar evolution stages during individual baroclinic life cycles, how do they relate to the evolution of the wind field, and what are consequences for the dynamic stability particularly in the tropopause region?*

Due to the dynamic stability criterion, the stably stratified stratosphere and the TIL in particular can sustain enhanced values of wind shear compared to the troposphere. Several research studies have shown that this is reflected in the mean vertical profile of the vertical wind shear (Birner et al., 2002; Birner, 2006; Sunilkumar et al., 2015; Zhang et al., 2015, 2019). This is of interest, because on one hand the occurrence of enhanced wind shear can be an indicator for the processes that force enhanced momentum gradients like the thermal wind forcing or gravity wave perturbations of the flow. Furthermore, regions of frequent occurrence of enhanced wind shear in the tropopause region are susceptible to the generation of dynamic instability with the potential for turbulent mixing and STE. To the authors knowledge a comprehensive analysis of enhanced vertical wind shear in the context of the planetary circulation and on climatological time scales does not yet exist. A subset of ten years of northern hemispheric data from the ERA5 reanalysis is used to approach this matter. The third analysis chapter focusses on the following central issue:

- *How does the occurrence of strong vertical wind shear relate to the planetary circulation; what are the forcing mechanisms for the wind shear; and what are possible consequences for cross tropopause transport?*

The thesis is organised as follows. Chapter 2 introduces the model data used and the underlying numerical model specifications. It furthermore presents an overview of the scientific objectives of the WISE campaign, how they were approached, and what measurement data were collected. Then, a set of analyses on different spatial and temporal scales is presented, from individual case studies to climatological considerations. In Chapter 3, measurements from two research flights which were conducted during the 2017 airborne WISE campaign are analysed, with the focus on mixing and STE within the ridge of baroclinic waves and in context of the TIL evolution. In Chapter 4, a composite analysis of breaking baroclinic waves over the North Atlantic is presented, based on a cyclone tracking algorithm and using a five year data set of operational ECMWF IFS analysis fields. The approach is closely linked to the results from Chapter 3 and therefore focusses on the TIL evolution as well as the occurrence of strong wind shear and the resulting dynamic flow stability in the tropopause region. Chapter 5 expands the results from Chapter 4, with a 10 year northern hemispheric climatology for the occurrence of strong wind shear in the lower atmosphere, based on the ECMWF ERA5 reanalysis data set. Chapter 6 comprises a summary of the key results of this work as well as an outlook on future research questions that arise from these results.

2

DATA AND METHODS

2.1 THE ECMWF INTEGRATED FORECAST SYSTEM

The numerical weather prediction model data used in this study is from the Integrated Forecast System (IFS) from the European Centre for Medium-Range Weather Forecasts (ECMWF). Currently, the IFS is one of the most advanced state of the art numerical model representations of the atmosphere. It features a hydrostatic dynamical core with a semi-implicit and semi-Lagrangian numerical scheme, treating terms which are associated with fast processes like gravity waves with an implicit numerical scheme because of advantageous numerical stability properties. The IFS features a spectral transformation between spectral space, where the equations of motion are solved, and grid-point space, where the advection is calculated as well as the effect of the parametrisation of the physical processes. In the vertical dimension the model features a discretisation on hybrid pressure-sigma levels (ECMWF, 2016a). Several parametrisations for non-resolved physical processes are implemented (Fig. 2.1), including schemes for radiation, microphysical processes in large scale clouds, convection, subgrid turbulent exchange of heat, momentum and moisture, and orographic and non-orographic gravity wave drag (ECMWF, 2016b).

The following section gives an overview of the IFS versions used in this work and significant advancements that have been implemented in nupdated versions of the IFS that went operational over the course of the research that is presented in this thesis. It furthermore includes a brief description of the physical parametrisation schemes of the IFS model.

2.1.1 *IFS versions, key features and physical parametrisation schemes*

The output from several IFS versions is incorporated in this work. The choice of data used for each analysis was made based on requisition (spatial and temporal resolution for certain tasks), necessity (efficiency), and availability at the time of the analysis[1]. The IFS versions used in this work include cycle Cy36r2 to Cy40r1 (operational analysis fields, Chapter 4), Cy43r3 (short time forecast fields, Chapter 3), and the the ERA5 reanalysis (Chapter 5) which is based on

---

[1] The ERA-5 reanalysis data set was only starting to become available during the later stages of this work.

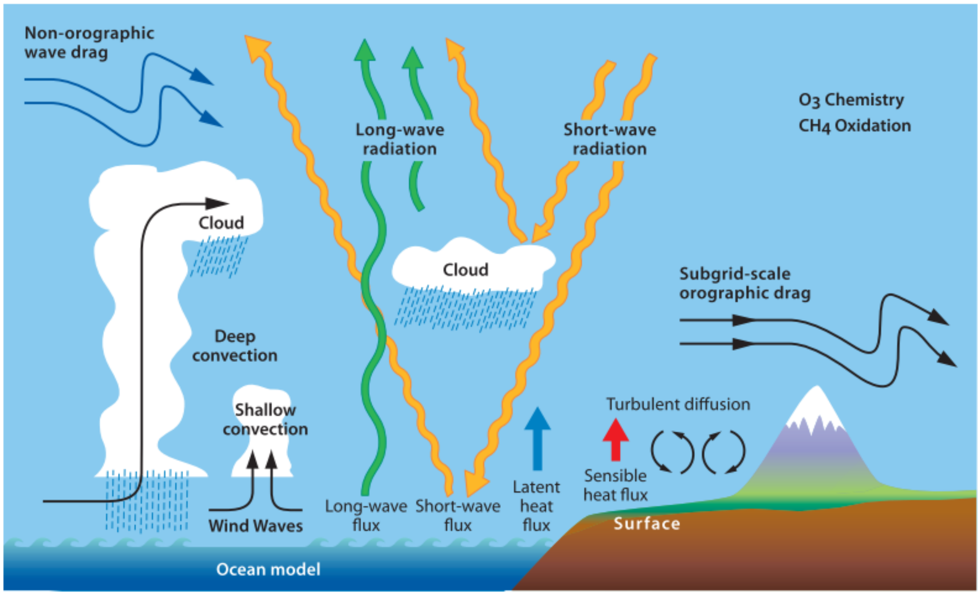

Figure 2.1: Schematic diagram of the physical processes implemented in the ECMWF IFS model. Figure adapted from ECMWF (2016b).

Cy41r2 (Table 1). The vertical resolution was increased from L91 to L137 with the implementation of IFS Cy38r2 in June 2013, enhancing the vertical hybrid sigma level count between the surface pressure and 1 Pa from 91 to 137. In the UTLS as the region of primary interest of this study, this translates to a similar vertical grid spacing for both vertical resolutions of about 300–400 m, depending on the elevation of the tropopause. A refined octahedral horizontal grid was implemented with Cy41r2 in March 2016, effectively increasing the horizontal grid spacing of the analysis and the high resolution forecast from 16 to 9 km. The ERA5 reanalysis is based on a spectral truncation of $\mathrm{T_L}639$, which corresponds to a horizontal grid spacing of about 31 km (Hersbach et al., 2020).

In the following paragraphs, the paramtrisation schemes of the IFS are introduced.

2.1.1.1 *Turbulence*

The turbulence parametrisation scheme in the IFS is implemented in form of tendency equations for the change rate of the prognostic variables associated with the horizontal momentum (u, v), heat (T), and moisture $(q, q_l, q_i$ for gaseous, liquid and frozen water). The tendency equations represent the turbulent diffusion due to non-resolved vertical turbulent mixing, and they are a function of the vertical gradient $\partial\phi/\partial z$, as well as an exchange coefficient K_ϕ

Version	Id.	Spectral truncation / grid used	Vertical lvl.	Δt
Cy36r2–Cy38r1	AN	T_L1279 / 0.25°	91 (surf.-1 Pa)	6 hrs.
Cy38r2–Cy40r1	AN	T_L1279 / 0.25°	137 (surf.-1 Pa)	6 hrs.
Cy41r2	ERA5	T_L639 / 0.25°	137 (surf.-1 Pa)	24 hrs.
Cy43r3	FC	O1280 / 0.125°	137 (surf.-1 Pa)	1 hr.

Table 1: Central features of IFS versions used in this work.

(in m^2 s^{-1}). The variable ϕ represents the quantities affected by the paramtrisation scheme (u, v, T, q). The choice of the turbulence closure that is applied depends on the height above the surface as well as on the local stratification. In the surface layer, i.e. the layer between the surface and the first hybrid sigma-pressure level, a first order K-diffusion approach based on Monin-Obukhov similarity theory is applied. In unstable boundary layers, the turbulence closure is extended to an Eddy-Diffusivity Mass Flux scheme, treating both local K-diffusion as well as non-local eddy mass transport through the boundary layer (Köhler et al., 2011). In the free atmosphere, the scheme distinguishes between unstable layers characterised by negative Brunt-Vaäisälä-frequencies $N^2 < 0$, where the exchange coefficient K_ϕ is determined according to Monin-Obukhov similarity theory, and stably stratified layers $N^2 > 0$, where K_ϕ is calculated based on a revised Louis scheme (Louis et al., 1982). Since this work focusses on the occurrence of shear-induced turbulence in the tropopause region, we will focus on the Louis scheme for stably stratified flow in the free atmosphere. The exchange coefficient K_ϕ generally depends on the vertical gradient of the transported constituent, as well as on a mixing length l. The Louis scheme introduces Richardson number dependent stability functions $f_{\mathrm{LTG},\phi}(Ri)$ as a factor of K_ϕ, which converge from 1 for $Ri = 0$ towards zero with increasing Richardson numbers. The resulting diffusion is nonzero even for above-critical Richardson numbers, acting towards a constant diffusive erosion of strong momentum and temperature gradients in regions of reduced Richardson numbers.

The core features of the turbulence parametrisation as described in the previous paragraph remained unchanged throughout the IFS versions that were used in this work. Several minor changes were implemented, however, mostly impacting the efficiency of the turbulent diffusion near the surface. Until IFS version Cy38r2, an altitude-dependent diffusive term with peak impact at 1 km height above the surface was implemented, to account for missing non-resolved shear that was identified via comparison with spectrally decomposed wind shear measurements. The exchange coefficient in the revised Louis scheme furthermore contained an altitude-dependent fractional contribution from the Monin-Obukhov and the revised Louis scheme stability functions, thus allowing a continuous transition between the boundary layer and the free atmosphere. The IFS version Cy41r1 simplified the turbulence scheme by removing both altitude-dependent terms, and reformulating the height dependency of the mixing length l (ECMWF, 2016b).

2.1.1.2 *Subgrid-scale orographic- and gravity wave drag*

The model furthermore includes a parametrisation scheme for unresolved orographic and non-orographic gravity wave drag on the mean flow. The subgrid-scale orographic drag is implemented as a turbulence induced momentum sink in the lower troposphere due to the non-resolved orography (< 5 km) (Beljaars et al., 2004), as well as a gravity wave drag due to absorption and reflection of vertically propagating gravity waves and a blocked flow drag due to the immediate blocking of the unresolved orography itself (Lott and Miller, 1997). The resulting drag is implemented in the form of additional momentum tendency terms for the horizontal wind components within the turbulence scheme.

The non-orographic gravity wave drag parametrisation scheme implements the effect of non-resolved gravity waves commonly caused by deep convection, frontal disturbances and shear zones. The scheme emits a globally uniform m^{-3} spectrum (with m being the vertical wave number) of non-resolved gravity waves upwards from the upper troposphere, with drag being applied to the mean flow when wave instability due to critical layers or reduced air density and non-linear dissipation occurs (Orr et al., 2010). Ultimately, the impact is implemented in the form of tendency terms $\partial\phi/\partial t$ caused by the divergence of the wave momentum flux, with ϕ representing the horizontal wind components (u, v) and the temperature (T).

2.1.1.3 *Convection*

Moist convection is implemented with an advanced version of the parametrisation scheme originally proposed by Tiedke (1989), adding tendency terms to the temporal evolution of heat, moisture, momentum, and chemical tracer distribution. The parametrisation makes use of different approaches for different cloud types, i.e. the removal of convective available potential energy (CAPE), the application of the large scale background vertical velocity, and the analysis of the moist static energy budget for the convective mass flux, for deep, mid-level and shallow convection. The parametrisation furthermore includes a simplified microphysics scheme to account for the effects of cloud and rain formation. The convection scheme is an important factor concerning the representation of the key variables N^2 and S^2 in the tropopause region as they influence the momentum and heat budget in outflow regions of deep convection through heat and momentum transport as well as through energy conversion.

2.1.1.4 *Clouds and large-scale precipitation*

The cloud and large-scale precipitation parametrisation represents processes like condensation, deposition, evaporation, collection, melting and freezing from and between different cloud water phases. The output of the scheme are prognostic equations for for different cloud water phases (cloud liquid, ice, snow water content and rain) as well as for a sub-grid fractional cloud cover (Tiedke, 1993; Forbes and Tompkins, 2011; Forbes and Ahlgrimm, 2014). The parametrisation furthermore allows the occurrence of supersaturation with respect to ice, as well as mixed phase clouds. The effect of latent heating due to condensation is implemented in the form of a temperature tendency term $\partial T/\partial t$.

2.1.1.5 *Radiation*

The radiation scheme implements the effect of short- and long-wave radiative fluxes independently, in the form of temperature tendency terms $\partial T/\partial t = f(\partial F/\partial p)$ as a function of the net vertical divergence of the radiative flux $\mathcal{F}$. The temperature tendencies due to radiative forcing can have a significant influence on the thermal structure in the UTLS and particularly in the tropopause region, due to pronounced vertical gradients of absorber trace gas species as well as clouds reaching up to the tropopause. The input for the scheme is a composite of the predicted temperature, humidity and clouds, as well as monthly mean climatologies for aerosols and trace gases that exhibit a significant radiative forcing. The scheme is based on the Rapid Radiation Transfer Model (RRTM, Mlawer et al. (1997) and Iacono et al. (2008)), and cloud-radiation interaction is implemented using the output from the cloud parametrisation and a Monte Carlo Independent Column Approximation (McICA) method (Morcrette et al., 2008). The long-wave scheme incorporates H_2O, CO_2, O_3, CH_4, N_2O as well as CFC11, CFC12 and aerosols as absorber, and performs the radiative transfer calculation over 16 spectral intervals between 10–3250 cm^{-1}. The short-wave scheme additionally considers O_2 as an absorber, and operates within 14 spectral windows between 800–50.000 cm^{-1}. The aerosol types are implemented following the climatology by Tegen et al. (1997), containing maritime, continental, urban, desert aerosol, as well as tropospheric and stratospheric background aerosol.

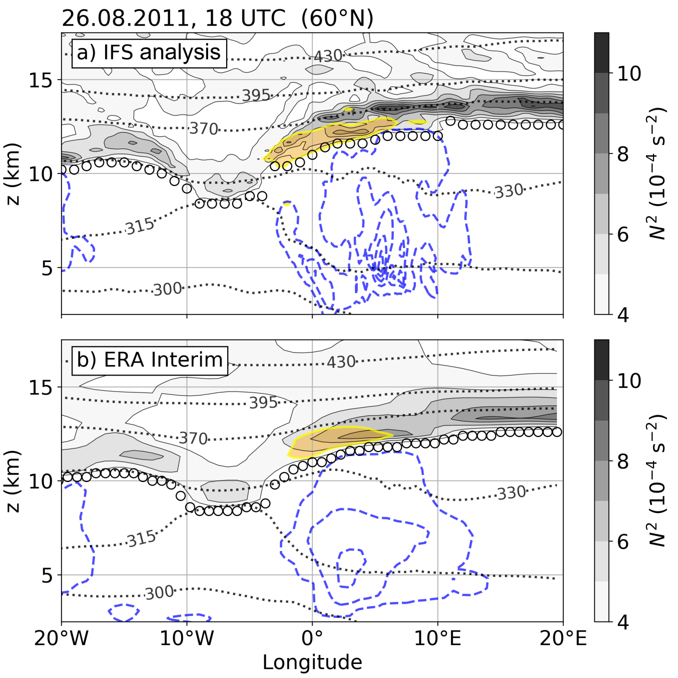

Figure 2.2: Exemplary vertical cross section at 60° N on 26 August 2011, 18 UTC. a) Operational IFS analysis data. b) ERA Interim reanalysis data. Greyscale filled contour shows static stability (N^2, in s^{-2}). Yellow shaded contour indicates intense vertical wind shear $S^2 \geq 4 \cdot 10^{-4}$ s^{-2}. Black dotted lines show isentropes (Θ, in K). Blue dashed lines show cloud ice water content (*ciwc*, in steps of 10^{-5} kg kg^{-1}). Black cirlce markers indicate LRT altitude.

2.1.1.6 *Surface parametrisation and chemistry parametrisation*

The IFS furthermore features a parametrisation for the surface fluxes of energy and water, as well as for ozone and methane chemistry. These parametrisation schemes however have no or a negligible direct effect on the thermodynamic structure in the UTLS as the region of interest in this work.

The IFS model output provided by the ECMWF that is used in this research will be introduced in Section 2.3, along with secondary derived quantities and central analysis methods.

2.1.2 *Representation of thermodynamic UTLS features in the IFS*

The representation of the thermodynamic structure in the UTLS from the IFS model depends on the model version and thus on the underlying vertical and horizontal grid spacing. Figure 2.2 illustrates this behaviour. It shows two vertical cross sections at the same time and location, comparing the representation of the TIL variability and related parameters in operational IFS analysis data with the same features in the ERA Interim data set. The ERA Interim data set has been used until recently, to derive climatological as well as synoptic scale features of the TIL (Gettelman and Wang, 2015), and it has been shown to reproduce central features of the TIL on these scales. However, in the following paragraphs it is briefly shown that ERA-Interim underestimates the occurrence of central flow features in the UTLS on the mesoscale. Since ERA5 was only available in the later stage of this thesis this then also was the motivation to use the operational analysis data for one study in this thesis.

The ERA Interim reanalysis is based on the Cy31r2 IFS version, which went operational in September 2006 (Dee et al., 2011). The horizontal grid spacing is approximately 80 km (T255 spectral), with Fig. 2.2a being based on a regular 0.75° latitude-longitude grid, and the model exhibits 60 levels in the vertical from the surface up to 0.1 hPa, which corresponds to a vertical grid spacing of about 1 km at tropopause altitudes. Figure 2.2b is based on operational IFS analysis fields from the Cy37r2 IFS version and used in this work, interpolated onto a regular 0.25° latitude-longitude grid. This model version exhibits a horizontal grid spacing of about 16 km (T_L1279), and 91 vertical level from the surface to 0.01 hPa. The vertical grid spacing at tropopause altitudes is much finer compared to ERA-Interim with about 300–400 m.

The comparison shows a stronger TIL in the high resolution model, as well as a more pronounced mesoscale variability particularly from 0° E eastwards, above the ridge that exhibits ice clouds reaching up to the elevated tropopause. These differences are expected, due to the better resolved thermodynamic structure on the finer vertical grid, as well as due to a more realistic implementation of the physical processes responsible for the fine scale structure in N^2, like e.g. the spectrum of resolved gravity waves. Advancements in newer versions can furthermore influence the representation of tropopause features like the TIL. This includes updates in the data assimilation procedure and a larger amount of incorporated observational data, as well as updates in the physical parametrisation schemes. For example, the implementation of the radiation scheme as described in Section 2.1.1 (see Morcrette et al. (2008)) presents one major update between the two model versions displayed in Fig. 2.2, exhibiting more accurate gas optical properties as well as the treatment of sub-grid cloud cover heterogeneity. Another example is the lack of a non-orographic gravity wave drag scheme in the Cy31r2 cycle. Generally, the advection scheme of numerical models erodes the gradients that define the tropopause sharpness with forecast lead time, which is counteracted by the parametrisation schemes of physical processes that sharpen the tropopause (Saffin et al., 2017). This indicates the importance of a realistic parametrisation of the non-resolved processes. Kunkel et al. (2016) show that the temporal evolution of the tropopause sharpness depends significantly on the individual process parametrisation that are incorporated in baroclinic life cycle simulations, as well as their interrelation. Developments in the parameterisation schemes consequently also affect the thermodynamic structure of the UTLS. Along with the increases in resolution of the model this reveals that the UTLS is best studied with the current state of the art model versions of the IFS.

2.2 THE 2017 WISE CAMPAIGN

One central aspect of this work is the occurrence of shear induced dynamic instability and turbulent mixing in the UTLS. The previous section introduced how non-resolved physical processes are implemented in the model through parametrisation schemes. These schemes present an approximation of each processes impact on the atmospheric flow. However, central aspects of these processes like e.g. their spatial and temporal characteristics or their transport efficiency through diffusive mixing are not finally understood, particularly in the UTLS as a comparatively remote region. Therefore, it is advantageous to use a synergistic approach and to build the analysis on numerical model output as well as in situ measurement data from the WISE field campaign, to validate key results and to compare observed processes with their representation in the model data.

The airborne measurement campaign WISE (Wave driven ISentropic Exchange) with the HALO (High Altitude LOng range) aircraft as measurement platform took place from September to October 2017, based in Shannon, Ireland, and with transfer flights from and to Oberpfaffenhofen, Germany. Several research institutions were involved, with the Jülich Research Centre (FZ Jülich) and the Johannes Gutenberg-University Mainz (JGU Mainz) as lead institutions. The different research groups supplied a sum of ten scientific instruments measuring trace gas distributions and meteorological state parameters with in situ and remote sensing techniques, contributing to the investigation of the four main research topics:

- Transport and mixing in the region of the ExTL and the influence of the TIL
- Role of Planetary wave breaking for water vapor transport into the extratropical lower stratosphere
- Role of halogenated substances for ozone and radiative forcing in the UTLS region
- Occurrence and effects of sub-visual cirrus (SVC) in the LMS

The first two topics focus on the impact of both the quasi-isentropic and the cross-isentropic cross-tropopause transport pathways on the chemical composition in the extratropical UTLS, and are thus also directly related with the topics to be addressed in this work.

The HALO is a modified Gulfstream G550 jet with a range of about 8000 kilometers, which makes it possible to investigate synoptic scale atmospheric features and conduct measurements in a large radius around the ground base.

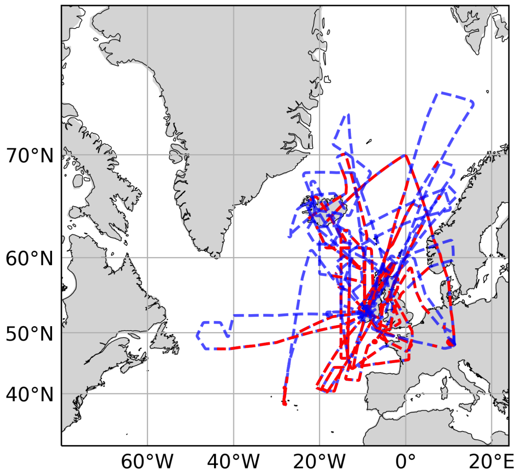

Figure 2.3: Flight paths of all 16 flights conducted during the WISE campaign from September–October 2017, including the transfer flights from and to Oberpfaffenhofen. Red dashed lines depict flight sections within 50 hPa vertical distance from the LRT, blue lines show the remaining flight sections.

Furthermore, the airplane can reach flight altitudes up to about 15 kilometers, i.e. $\Theta = 360 - 420$ K potential temperature, depending on season and location, which allows the investigation of both the upper troposphere and the lower stratosphere even above elevated tropopauses (in the extratropics). During WISE, a sum of 16 research flights were conducted (Table 2), mostly focussing on the tropopause region within large scale atmospheric wave patterns in the North Atlantic storm track region. Figure 2.3 shows the flight paths from all flights and indicates that a significant proportion of the flight legs were situated close to the tropopause. The HALO payload comprised of a variety of in-situ measurement systems for the determination of the abundance of different atmospheric trace gasses, as well as remote measuring systems like the Karlsruhe Institute for Technology (KIT) Gimballed Limb Observer for Radiance Imaging of the Atmosphere instrument (GLORIA). The atmospheric state parameters like temperature and air pressure during the flights were measured with the Basic HALO Measurement and Sensor System (BAHAMAS).

The JGU Mainz participated with the University of Mainz Airborne Quantum Cascade Laser Spectrometer (UMAQS). It obtains direct absorption spectra of air samples within a 76 m astigmatic multipass absorption cell. During WISE the spectrometer was calibrated for the simultaneous measurement of carbon monoxide (CO) and nitrous oxide (N_2O), with a total drift-corrected uncertainty for CO of 0.18 ppbv and 0.94 ppbv for N_2O (for further details on the measurement principle and the error estimation, see Müller et al. (2015) and therein).

Carbon monoxide and nitrous oxide are an established combination of trace gasses with tropospheric origin to determine tropospheric influence in the stratosphere and vice versa (e.g. Müller et al., 2015; Kunkel et al., 2019). Nitrous oxide is chemically inert in the troposphere and exhibits a comparatively long tropospheric lifetime of about 120 years, resulting in an almost homoge-

Flight date	No.	Flight objectives
31.08.2017	01	Electromagnetic compatibility flight
13.09.2017	02	Jet structure, TIL structure
18.09.2017	03	Rossby wave breaking, Asian Monsoon air
20.09.2017	04	Follow-on, decay of subtropical air mass
23.09.2017	05	TIL at edge of tropospheric intrusion, associated with gravity wave activity
27.09.2017	06	Outflow from North America, jet structure
28.09.2017	07	Highly structured tropopause
01.10.2017	08	Outflow form hurricane Maria and Asian Monsoon
04.10.2017	09	Filaments in decaying trough, SVC in outflow region of a warm conveyor belt
07.10.2017	10	Early stage of Rossby wave breaking over the Atlantic
09.10.2017	11	Follow-on, Rossby wave breaking in later stage
12.10.2017	12	Beginning occlusion within a Rossby wave, pronounced TIL and mixing
14.10.2017	13	Follow-on, decaying of filament in trough over Iceland
15.10.2017	14	Warm conveyor belt outflow and potential impact of hurricane Ophelia
19.10.2017	15	Sampling of air masses around hyperbolic point and related mixing effects
21.10.2017	16	Rossby wave breaking and transfer flight

Table 2: Overview of the research flights conducted during the WISE campaign. The flights which are analysed in Chapter 3 are highlighted in blue.

nous mixing ratio in the free troposphere remote from surface sources. The tropospheric mixing ratio exhibits a positive trend due to increasing emissions. For September and October 2017 the mixing ratio was determined to 330.375 ppbv and 330.575 ppbv on the Northern Hemisphere, according to the Combined Nitrous Oxide data from the NOAA/ESRL Global Monitoring Division (www.esrl.noaa.gov). In the stratosphere, N_2O is depleted via photolysis as well as the reaction with atomic oxygen $O(^1D)$, which results in decreasing mixing ratios with height above the tropopause. This makes it possible to determine a chemical tropopause based on the N_2O mixing ratio (Assonov et al., 2013). The tropospheric CO mixing ratio is determined by local sources like transport or biomass combustion processes, and it exhibits a pronounced variability

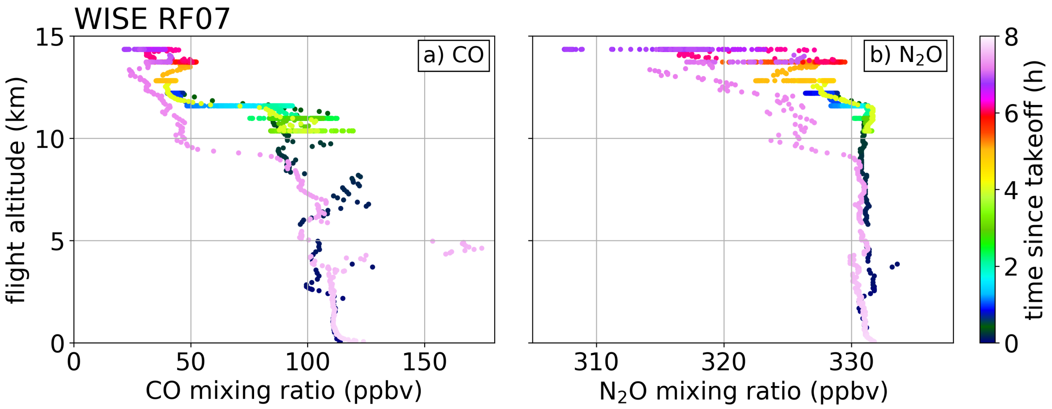

Figure 2.4: Vertical profiles of UMAQS trace gas mixing ratio measurements during WISE RF07 on 28 September 2017, for a) CO and b) N_2O. Colour code indicates flight time since takeoff in hours.

reaching from around 40 ppbv up to several hundreds of ppbv. In the stratosphere, CO is depleted via the reaction with OH radicals, and produced in the reaction cycle of the methane oxidation. In the absence of tropospheric input, the stratospheric CO mixing ratio decreases with height above the tropopause until it reaches a source-sink equilibrium value of about 10–15 ppbv (Flocke et al., 1999).

Figure 2.4 exemplarily illustrates vertical profiles of CO and N_2O mixing ratios, based on measurements performed during WISE research flight RF07, which took place on 28 September 2017. The troposphere is characterised by comparatively large ($\mathcal{O}(10^2$ ppbv$)$) and highly variable CO mixing ratios, as well as the well mixed N_2O background mixing ratio around 330 ppbv. After the ascend, the airplane approached the tropopause at altitudes of about 12 km, where the mixing ratios of both trace gas species decrease. During the descent at the end of the research flight, the tropopause was located at lower altitudes below 10 km, which is also apparent in the vertical profiles from both trace gas species.

2.3 ANALYSIS METHODS

The ECMWF IFS model data in this work is used and processed on the native vertical hybrid sigma model levels. In the horizontal dimension they are generally (if not noted otherwise) processed on a regular latitude-longitude grid with a 0.25° grid spacing.

Basic variables such as the temperature T, the three-dimensional wind (u, v, ω), the relative vorticity ζ_{rel}, and the cloud ice water content *ciwc* are directly provided by the ECMWF. Secondary quantities like the static stability N^2, the vertical wind shear S^2, or the potential vorticity Q are derived from the basic variables, and calculated on half levels (centred differences) to retain a maximum amount of information in the gradient based measures.

In Chapter 3, short time forecast data on an hourly basis with an enhanced horizontal grid spacing of 0.125° is linearly interpolated in space and time onto the flight path, where the altitude, latitude and longitude information from the BAHAMAS is used with 1 Hz measuring frequency. The short time forecast fields are favourable over the analysis fields, because the increased temporal resolution results in reduced root mean square error (RMSE) values when comparing the interpolated IFS data with the in-situ measurements of e.g. the zonal wind component. The BAHAMAS data in general (e.g. air temperature, pressure, wind components) as well as the UMAQS trace gas mixing ratio measurements are processed and analysed on a 1 Hz basis. The viability of the comparison of these high resolution in situ measurements with comparatively low resolution model data ($dx \geq 10$ km, $dt \geq 1$ h) is discussed throughout the analysis in Chapter 3.

The LRT altitude is determined according to the the WMO definition (WMO, 1957) as the first level in the vertical temperature profiles where the lapse falls below 2.0 K km^{-1} with the condition that it remains below this value between this level and all higher levels within 2 kilometer above.

The strength of the TIL in this work is defined as the maximum in static stability N^2 within 3 km vertical distance above the local LRT (as used by e.g. Erler and Wirth, 2011). Other definitions are possible and used in different research studies, like the average of N^2 over a defined vertical extent relative to the local LRT (Kunkel et al., 2014), or the first maximum in N^2 above the LRT and above a certain threshold (Gettelman et al., 2011). The definition used in this work was found to preserve most of the information on the horizontal variability of the TIL strength.

In Chapter 5 the analysis is partly built upon quantities on the dynamic tropopause that is provided by the ECMWF, i.e., the $Q = 2$ pvu surface (ECMWF, 2016c).

3

OBSERVATION OF SHEAR INDUCED MIXING IN NORTH ATLANTIC BAROCLINIC WAVES

During September and October 2017 the airborne measurement campaign WISE took place. One of the major objectives of the campaign was to investigate the tropopause inversion layer (TIL) with a focus on its evolution during baroclinic life cycles in the North Atlantic storm track region. This was motivated by a variety of preceding studies indicating a multitude of influencing factors on the TIL formation and maintenance, accompanied by a spatial and temporal occurrence variability on a broad spectrum of scales.

The tropopause inversion layer and the processes leading to its formation have been studied quite extensively with numerical, idealized models. Several studies exist which describe the TIL as a climatological feature and only a few others also analyse the processes that lead to the formation of the enhanced static stability in the lower stratosphere. The first analysis of this thesis aims to provide new observational insights into the TIL in the North Atlantic storm track. This will be achieved through analysis of individual flights from the WISE campaign which took place in 2017 mainly from Shannon, Ireland. The second major scientific question of the mission was to study the interrelation between the TIL and the ExTL, as previous studies had indicated a potential causal relationship between the occurrence of STE and the TIL. Section 3.1 and 3.2 present the analysis of two research flights, addressing the following central questions:

- *How well can models capture the TIL structure in the extratropical LMS?*
- *Are there causal relationships between the thermal and dynamic structure and the chemical composition in the extratropical tropopause region, in particular with the focus on the TIL and the ExTL?*

Parts of this chapter have been included in the following publication: Kunkel et al. (2019)

3.1 SHEAR INDUCED MIXING IN A RIDGE OF A BAROCLINIC WAVE: WISE RF07

Research flight RF07 aimed at the survey of the tropopause region during a pronounced baroclinic wave breaking process over the North Atlantic in late September. The following subsection first presents an analysis of the synoptic situation and flow features derived from IFS model data, followed by a description of the research flight as well as the measurements taken. Then, the ExTL trace gas signatures are put into context of the dynamic structure of the tropopause region derived from ECMWF IFS data, e.g. the coincidence between enhanced observed trace gas gradients and the model-derived tropopause, and mixing signatures in tracer-tracer correlations and indicators for the underlaying process in the model data.

3.1.1 *Synoptic situation from 27 to 29 September 2017 over the North Atlantic*

On 27 September 2017 a local minimum in the mean sea level pressure (MSLP) became evident east of Newfoundland, leading to the formation of a low pressure system. This system crossed the North Atlantic within 24 hours (Fig. 3.1), while intensifying rapidly and reaching a minimum mean sea level pressure of 973.22 hPa around 28 September 2017, 18 UTC. During the first hours the surface cyclone migrated along the enhanced isentropic PV gradient defining the border of the trough over the North Atlantic, eventually superimposing with the cyclonic wind field induced by the UTLS PV anomaly of the trough (Davis and Emanuel, 1991). The cyclone intensified and the PV signature became increasingly deformed by the rotational wind field, with the synoptic scale downstream ridge wrapping around the surface cyclone centre. During the following lysis stage of the cyclone, the trough and the ridge broke up into a filamented UTLS flow which was dominated by gradual irreversible mixing that worked towards restoring the background PV gradient structure.

Around the time of maximum surface cyclone intensity, the downstream ridge was characterised by a pronounced TIL, i.e. enhanced values of static stability $N^2 > 6 \cdot 10^{-4}$ s^{-2} in the LMS closely above the LRT (Fig. 3.2a). The upper tropospheric flow was dominated by a jet streak which was situated within the ridge at the upper tropospheric front, with maximum horizontal wind speeds between $50 - 60$ ms^{-1} reaching up to the tropopause (Fig. 3.2b). The TIL exhibited a synoptic scale dipole structure, with enhanced N^2 above the tropospheric ridge on the anticyclonic shear side of the jet streak, and comparatively low static stability of the order of the stratospheric background

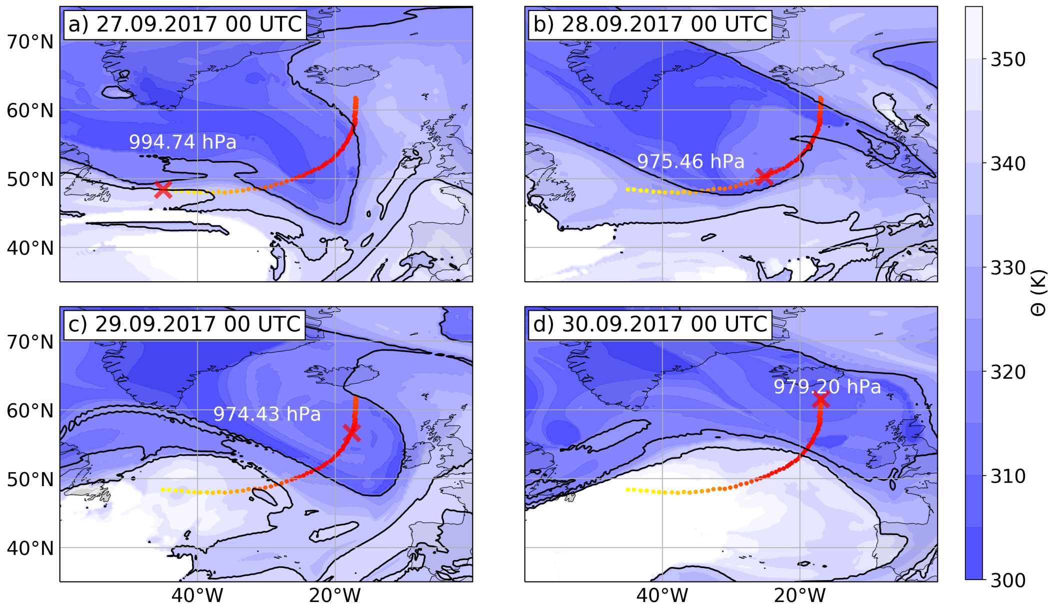

Figure 3.1: Potential temperature Θ on $Q = 2$ pvu dynamic tropopause, for four time steps during the evolution of the baroclinic wave. Contour lines for $\Theta = 320$ and 340 K are highlighted in black. Path of minimum surface pressure during the four days is shown in all four panels, with the current location indicated by the red x, and the $MSLP$ minimum colour coded from 994 hPa (yellow) to 973 hPa (red).

stratification $\overline{N^2}_{strat} = 4 \cdot 10^{-4}$ s^{-2} above the trough (not explicitly shown). This agrees with theoretical studies on the adiabatic large scale TIL forcing (Wirth, 2003, 2004) in idealised baroclinic life cycle simulations (Wirth and Szabo, 2007; Erler and Wirth, 2011). The mesoscale variability of the TIL within baroclinic waves is furthermore known to be influenced by enhanced gravity wave activity in this region (Wirth and Szabo, 2007; Kunkel et al., 2014) as well as diabatic processes like turbulence, cloud radiative forcing in the outflow region of warm conveyor belts, or the impact of latent heat release on ascending tropospheric airstreams (Kunkel et al., 2016).

The tropopause region where the TIL emerged was furthermore characterised by exceptional vertical wind shear $S^2 \geq 4 \cdot 10^{-4}$ s^{-2} (Fig. 3.2a) above the jet core and on its anticyclonic shear side (Fig. 3.2b). These regions of enhanced S^2 exhibit similar characteristics compared to the regions of enhanced N^2 concerning the mesoscale horizontal variability and the vertical location and extent above the tropopause. The localised enhacement of N^2 and S^2 shows no general co-occurence on the mesoscale but rather an occasional overlap. Therefore, the dynamic stability of the flow at the tropopause is highly variable with regions of Richardson numbers well above the critical threshold Ri_c, and regions

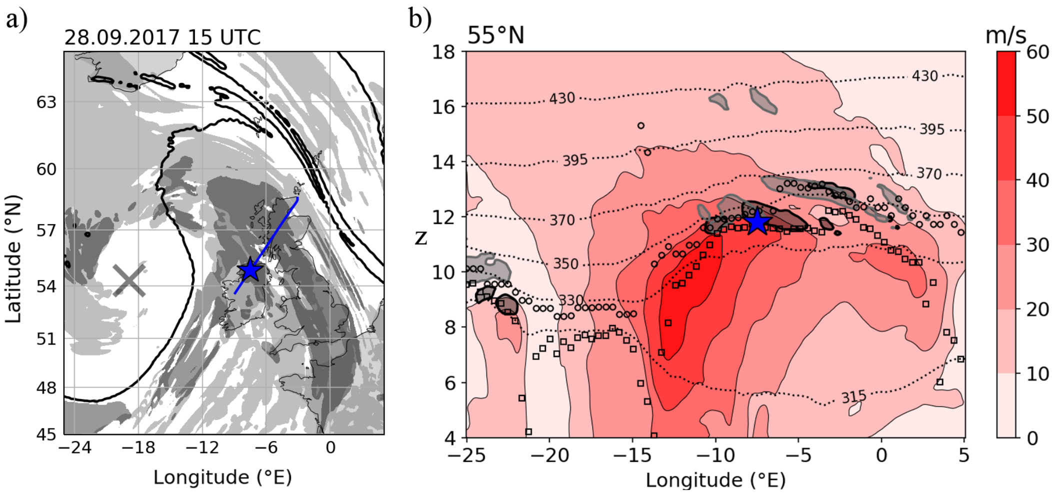

Figure 3.2: a) Selection of UTLS features on 28 September 2017, 15 UTC from ECMWF IFS forecast data. Solid black line indicates $\Theta(Q = 2 \text{ pvu}) = 320$ K dynamic tropopause potential temperature. Light grey filled contour indicates regions where the static stability N^2 in the LMS exceeds $6 \cdot 10^{-4}$ s^{-2}, dark grey filled contour where the vertical shear of the horizontal wind S^2_{max} exceeds $4 \cdot 10^{-4}$ s^{-2} within 1 km vertical distance from the local LRT. RF07 flight path from 14:20–15:15 UTC is indicated in blue, HALO location at 15 UTC by blue star, MSLP minimum by grey x. b) Vertical cross section at 55° N, filled contour shows horizontal wind speed, dotted lines isentropes, black dots LRT altitude, black squares dynamic tropopause altitude, and blue star location of the DLR HALO at 15 UTC. Black filled contour indicates $N^2 \geq 6 \cdot 10^{-4}$ s^{-2}, and grey filled contour regions of enhanced vertical wind shear $S^2 \geq 4 \cdot 10^{-4}$ s^{-2}

with reduced Richardson numbers. This situation conceptually resembles the findings of Kunkel et al. (2016), who describe the occurrence of turbulence and STE particularly in regions where a pronounced TIL emerges during idealised baroclinic life cycle simulations. This issue is the conceptual starting point for the measurements taken during research flight RF07, with the goal to study such regions and find signatures of mixing and turbulence related to these situation.

3.1.2 *Identification of small scale mixing above the tropopause during WISE RF07 on 28 September 2017*

The flight took place on September 28 with take-off time at 13:15 UTC, and the flight pattern consisted mainly of two flight legs across the downstream ridge, with each of them repeated three times at different flight altitudes around the

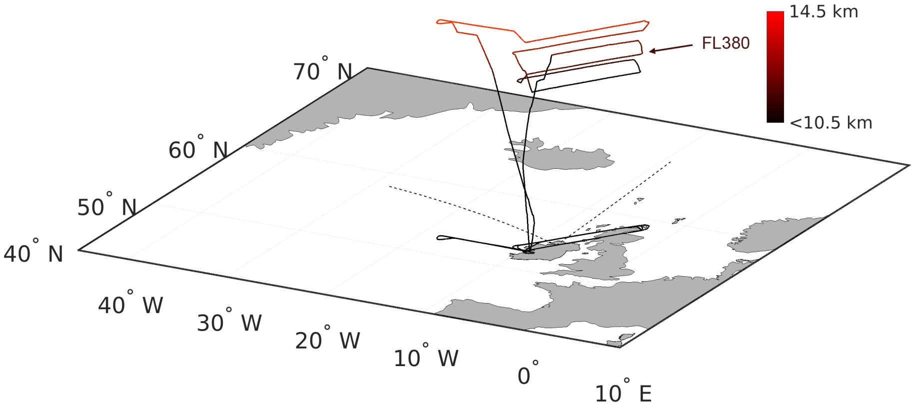

Figure 3.3: Flight pattern of research flight RF07. Colour code indicates flight altitude, black solid line shows surface projection of the flight path. The black dotted lines indicate the location, the viewing direction and the opening angle of photographies of Kelvin Helmholtz billows that were taken at 15:03 UTC and are analysed in Section 3.1.3.

tropopause (Fig. 3.3). The flight was concluded by a westward excursion into the occlusion close to the cyclone centre. The first leg was heading northeastward at FL410 which corresponded to about 12.4 km GPS altitude (Fig. 3.4a) at potential temperatures between 350–360 K (Fig. 3.4b). At that time the tropopause was located about 1–2 km below the airplane. The first flight leg was followed by a descent to FL380 (11.8 km respectively Θ =340–350 K) and a return to the southwestern edge of the staged legs. During the second flight leg from 14:20–15:15 UTC the airplane gradually approached the tropopause above the ridge of the baroclinic wave.

Figure 3.4b shows a comparison of in situ measured atmospheric state parameters, i.e., the horizontal wind components (u, v) and the potential temperature Θ, and IFS forecast data that was interpolated in time and space onto the flight path. The large scale wind and temperature features are resolved in the model, like the pronounced meridional wind peak of the jet streak that is crossed several times. The general agreement motivates a synergistic analysis based on in situ measurements and IFS forecast data. It becomes necessary to factor in model data due to the lack of three dimensional measurements and the consequential lack of measured gradient based quantities, i.e. static stability N^2 and vertical wind shear S^2. However, it should be considered that the interpolated model derived quantities remain an approximation, due to the limited temporal and spatial resolution of the model and, closely linked, its capability to realistically resolve relevant physical processes. This will be further discussed throughout the analysis.

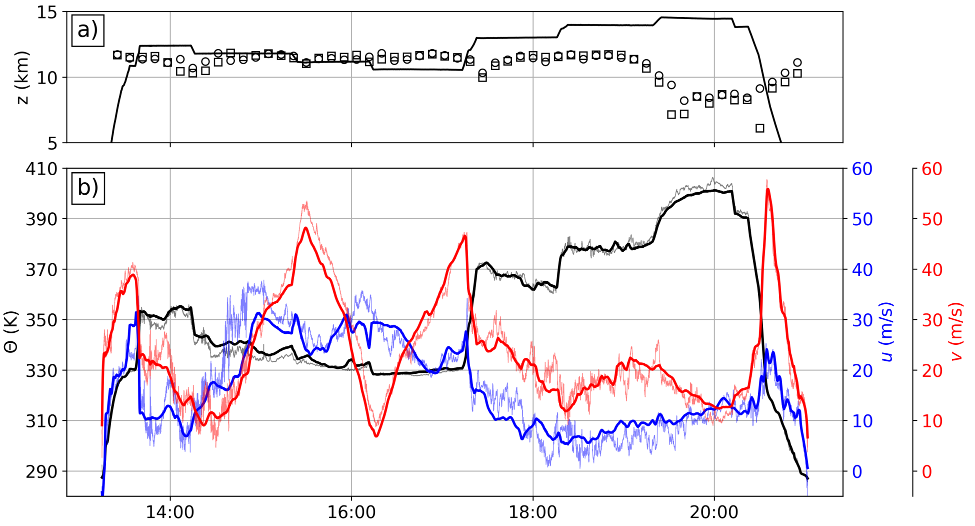

Figure 3.4: Time series of measured and model-derived quantities during WISE RF07 on 28 September 2017. a) Flight altitude (black solid, in km) and model-derived quantities from IFS forecast data, showing LRT altitude as black circle markers (z(LRT), in km), and $Q = 2$ pvu dynamic tropopause altitude as black square markers ($z(Q = 2$ pvu), in km). b) Black line shows potential temperature along flightpath (Θ, in K), blue line shows zonal wind component (u, in m s^{-1}), and red line meridional wind component (v, in m s^{-1}). Bright colors show IFS forecast data interpolated along the flight path, flat colors show in situ measured quantities.

During the tropopause approach at flight level FL380, the airplane crossed a region where the IFS forecast predicted enhanced static stability N^2 as well as enhanced vertical wind shear S^2 above the local LRT (Fig. 3.5a). The horizontal and vertical succession of these features resulted in a pronounced variability of the Richardson number along the flight path, with minimum values of the order of magnitude of $\mathcal{O}(1)$ at around 14:36–14:54 UTC (Fig. 3.5b). While Ri remained above the critical threshold Ri_c, the low values indicate a tendency towards dynamic instability and the gradual onset of efficient turbulent diffusion in the model due to the turbulence parametrisation.

The comparison of the IFS forecast with the in situ trace gas measurements shows a general consistency (Fig. 3.5c). The N_2O and CO volume mixing ratios increase with decreasing distance from the tropopause and stabilise at tropospheric background values after 14:54 UTC, where the NWP data indicate a distance of the airplane from the LRT of less than 300 meter. After 14:36 UTC and with decreasing Richardson numbers, the trace gas mixing ratios show an increase in variability, with a wave pattern that appears to break down into turbulent motion after 14:48 UTC, before eventually reaching stable tropospheric

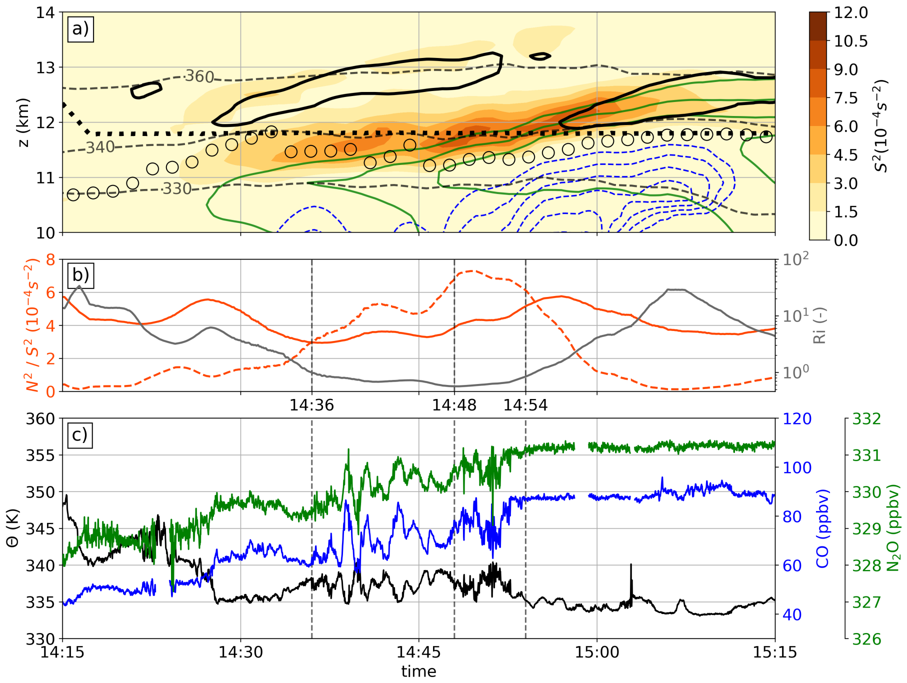

Figure 3.5: a) Height-time cross section along the flight path on FL380, derived from hourly IFS forecast fields, between 14:15 and 15:15 UTC on 28 September 2017. Vertical wind shear S^2 (color-coded), static stability isoline $N^2 = 6 \cdot 10^{-4}$ s^{-2} (black solid), flight altitude (black dotted), isentropes Θ (grey dashed), cloud ice water content *ciwc* (blue dashed in steps of $5 \cdot 10^{-6}$ kg kg^{-1}), horizontal wind speed $\sqrt{u^2 + v^2}$ (green solid, starting at 40 m s^{-1} and in steps of 10 m s^{-1}), and LRT altitude (black circles). b) Static stability N^2 (solid red), vertical wind shear S^2 (red dashed), and Richardson number Ri (black solid, logarithmic scale). Quantities along flight path derived from IFS forecast data. c) Measured potential temperature (black solid, BAHAMAS, in K), N_2O mixing ratio (green, UMAQS, in ppbv), and CO mixing ratio (blue, UMAQS, in ppbv).

background values after 14:54 UTC. Both the wave and the turbulent signal are also apparent in the measured potential temperature time series. These features are not resolved in the IFS.

The tracer-tracer correlation between the N_2O and the CO mixing ratio for the whole flight (Fig. 3.6) shows the expected behaviour. The troposphere is characterised by a pronounced CO variability on nearly constant N_2O background mixing ratios of about 331 ppbv (compare Fig. 2.4). The stratosphere exhibits an approximately linear correlation between both decreasing N_2O and CO. The trace gas measurements at 14:20–14:54 UTC during the tropopause approach of the airplane connect the tropospheric and the stratospheric branch on a distinct slope.

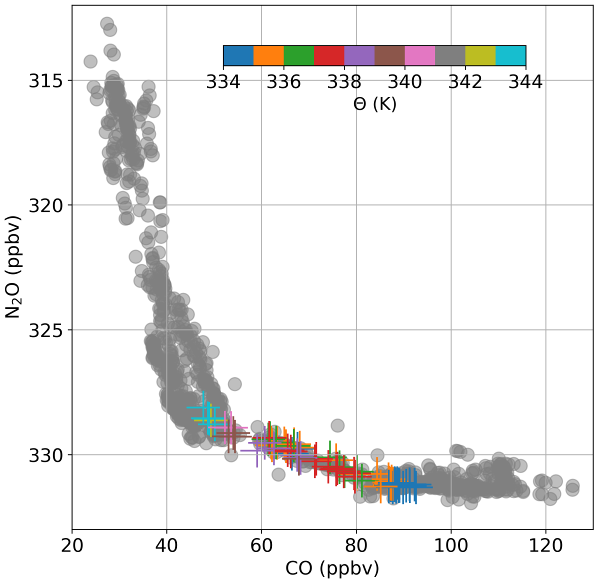

Figure 3.6: Tracer-tracer correlation of the mixing ratios of N_2O and CO that were measured during WISE RF07. Grey circle markers indicate mixing ratio pairs for the whole research flight, color coded cross markers show measurements for the time from 14:20–14:54 UTC, with the color indicating the measured potential temperature Θ.

The behaviour of the correlation between N_2O, CO and the potential temperature is further analysed for individual segments between 14:20–14:54 UTC. In the first part for times between 14:20–14:36 UTC an almost expected relationship between CO, N_2O and Θ is apparent. While CO and N_2O correlate, they anti-correlate with Θ (Fig. 3.7d). With decreasing potential temperature and thus decreasing distance from the tropopause, both N_2O and CO increase towards tropospheric values.

Inside the wave pattern at 14:36–14:48 UTC, the correlation becomes perturbed. The CO profile in vertical Θ-coordinates broadens (Fig. 3.7b) compared to the compact CO profile before the airplane crosses the wave pattern (Fig. 3.7a). Thus, individual isentropes now exhibit a larger span of CO mixing ratios between tropospheric and stratospheric background values. The tracer-tracer correlation reveals mixing lines on several isentropes (Fig. 3.7e). The trace gas mixing ratios of N_2O and CO still correlate, however, the anti-correlation with Θ vanishes. Individual Θ values between about 335–340 K exhibit an increased span of N_2O-CO-pairs, indicating an isentropic transition from stratospheric to tropospheric trace gas mixing ratios.

During the following 6 minutes after 14:48 UTC, both trace gasses as well as the potential temperature exhibit a high frequency variability, which can be interpreted as turbulent motion. Interestingly, the vertical profile of CO shows again a more compact structure (Fig. 3.7c), and the tracer-tracer correlation exhibits a rather strict anti-correlation between Θ and the correlated trace gas mixing ratios (Fig. 3.7f). A possible interpretation is that between 14:48–14:54 UTC the mixing process is still in progress and the trace gas mixing ratios are not yet homogenised across isentropes. The wave pattern that is crossed earlier

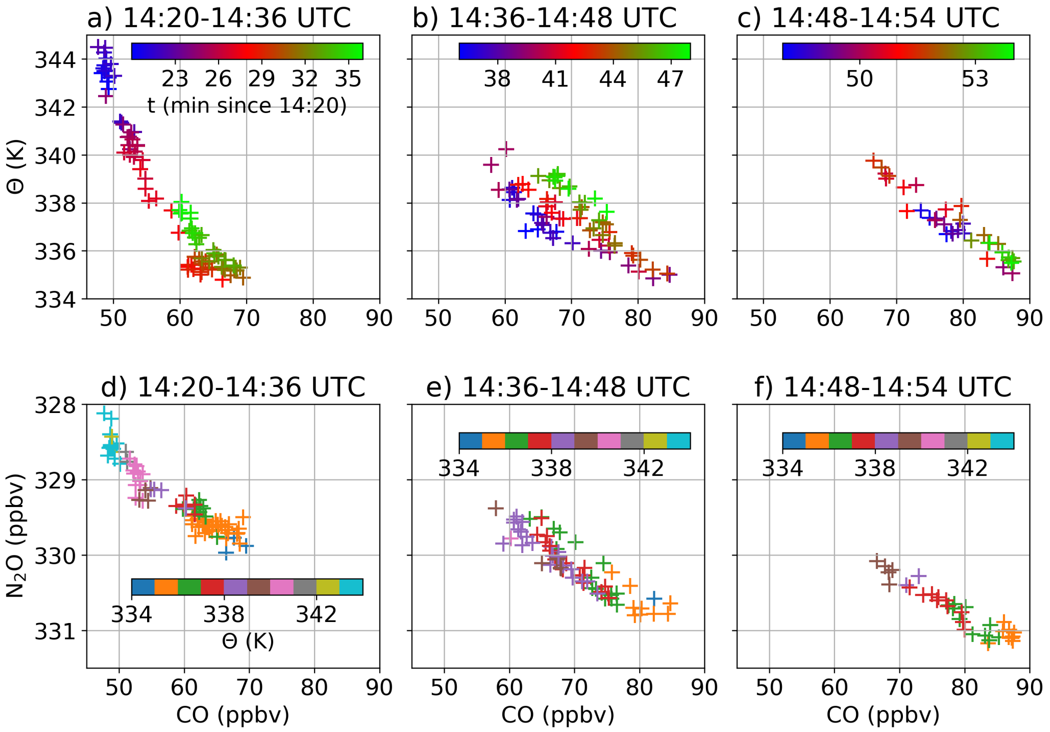

Figure 3.7: Correlation analysis of the measurements presented in Fig. 3.5c. a) - c): CO-Θ correlation for the three successive time periods during the flight leg on FL380, with the time since 14:00 UTC colour-coded. d) - f): CO-N_2O tracer-tracer correlation, with the colour code indicating the measured potential temperature Θ in K.

is located downstream of the flow, and the isentropic mixing lines could be the result of the mixing process upstream.

In summary, the IFS forecast predicts a dynamic situation which agrees with the in situ measurements, up to the point where horizontal and vertical resolution restrictions limit the capability of the model to resolve structures in the flow. Above the LRT within the ridge of the baroclinic wave a pronounced TIL emerges in accordance with the forcing mechanisms that are known from theoretical considerations and idealised numerical baroclinic life cycle simulations. In the same region, a layer of enhanced wind shear emerges, above the jet core and directly above the LRT. Exceptional vertical wind shear commonly occurs in this region, in accordance with the enhanced horizontal temperature gradients at the upper tropospheric front and the associated thermal wind shear forcing above the jet core.

Additionally, the layer of enhanced vertical wind shear in Fig. 3.5a shows a wave pattern with a horizontal wavelength in flight direction of about $\lambda_h = 150$

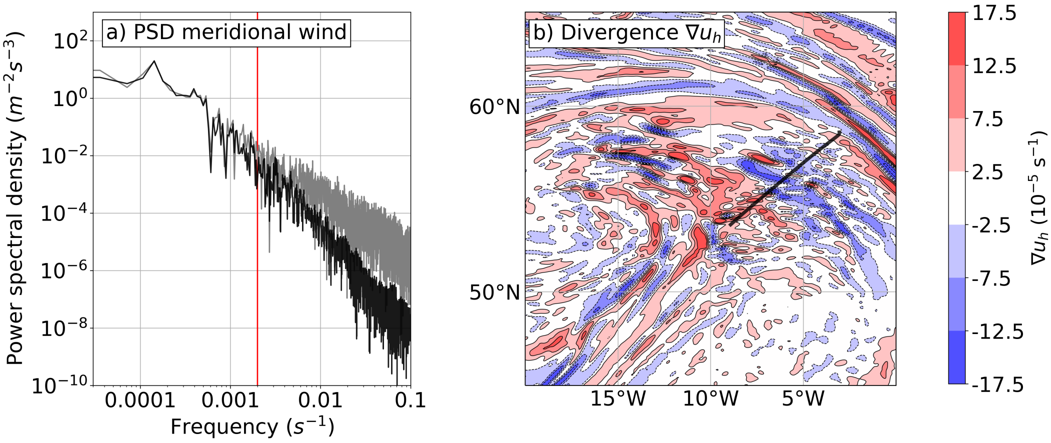

Figure 3.8: a) Power spectral density of the meridional wind along the flight path during WISE RF07, comparison between BAHAMAS measurements (grey solid) and IFS forecast data (black solid). Red line indicates $f = 2 \cdot 10^{-3}$ s^{-1}. b) Divergence of the horizontal wind $\vec{\nabla} \cdot \vec{u}_h$ at 11.5 km altitude on 28 September 2017, 15 UTC. Black line indicates the flight path of the research aircraft between 14:20–15:15 UTC.

km, estimated from the three S^2 maxima during 37 minutes flight time at an average speed of about 200 m s^{-1}. This mesoscale variability in S^2 could be associated with a gravity wave. The time series of the horizontal wind components along the flight path show a similar mesoscale wave signal (Fig. 3.4b), in the measurements, as well as with a reduced amplitude in the IFS data, particularly prior to 14:30 UTC since the wave structure that is evident in S^2 was not directly crossed. Research studies on the spectrum of resolved gravity waves in the ECMWF IFS have shown a reduced effective resolution due to the diffusive filter which is applied at the shortest scales to improve numerical stability (ECMWF, 2016a). Preusse et al. (2014) describe a distinct fall-off in the power spectrum of the temperature along latitude circles at about 220 km horizontal wavelength, which corresponds to a factor of about 9 compared to the horizontal grid spacing of 25 km in the IFS version used in the study. In the present case, the octahedral O1280 grid in the IFS Cy43r3 corresponds to a horizontal grid spacing of about 9 km. The power spectral density of the meridional wind along the flight path derived from the IFS forecast begins to decrease significantly compared to the measurements at frequencies below about $f = 2 \cdot 10^{-3}$ s^{-1} (Fig. 3.8a). This corresponds to a wavelength of $\lambda = 100$ km. The power density spectra differ between 100–200 km wavelength ($1 \cdot 10^{-3}$ s^{-1} $< f <$ $2 \cdot 10^{-3}$ s^{-1}), indicating that the model resolves wave features at this size range, however not necessarily realistically. Wave structures larger than $\lambda > 200$ km ($f < 1 \cdot 10^{-3}$ s^{-1}) are well represented in the model, up to the peak at about $f \approx 1.5 \cdot 10^{-4}$ s^{-1} which corresponds to the meridionally aligned jet streak that is crossed several times (compare Fig. 3.5b).

The divergence of the horizontal wind at 11.5 km altitude indicates pronounced gravity wave activity in the region of interest (Fig. 3.8b, compare e.g. O'Sullivan and Dunkerton (1995), Plougonven and Snyder (2005), and Kunkel et al. (2014)). The ridge of the baroclinic wave comprises several sources for the generation of gravity waves on a large spectrum of intrinsic frequency scales, like high reaching convection, cross-frontal circulation, and ageostrophic flow components in the jet-exit region. The representation of the wave spectrum in the IFS depends on the resolution capabilities of the model, as well as the implementation of the gravity wave source mechanisms. Overall, the mesoscale variability of the layer of enhanced wind shear is likely forced or at least influenced by gravity waves that are resolved in the IFS.

The identification of the layer of enhanced wind shear above the LRT proves to be a useful indicator for the potential of dynamic instability and turbulent mixing. The time series of N_2O, CO and Θ show small scale wave perturbations within the layer of enhanced wind shear, and below the resolution capability of the model. These small scale waves potentially become dynamically unstable, which can result in turbulent breakdown of the flow and vertical mixing across trace gas gradients. This is evident in the perturbed correlation between N_2O, CO and Θ. While the signal for quasi-isentropic mixing in the trace gas measurements remains a very localised spot measurement, the hypothesised scale transition from large scale background wind shear to mesoscale gravity wave induced gradient sharpening, and eventual small scale wave growth due to dynamic instability agrees with theoretical considerations on the occurrence of CAT and observations thereof (Sharman et al., 2012). One central result from the analysis presented is the identification of the layer of enhanced vertical wind shear and its distinct features, i.e., the region of occurrence, the vertical confinement, and the mesoscale variability, particularly in comparison to the TIL.

The IFS forecast predicts a region of reduced Richardson numbers in the LMS directly above the LRT, which is caused by the layer of enhanced vertical wind shear. Enhanced wind shear does not correlate well with the occurrence of turbulence (e.g. Knox, 1997), but it is a prerequisite for turbulence to occur in stably stratified flow. Figure 3.2b indicates that the occurrence of $S^2 \geq 4 \cdot 10^{-4}$ s^{-2} is limited to the region directly above the tropopause, which agrees with the fact that tropospheric flow generally can not sustain such wind gradients, according to the dynamic stability criterion. In the stratosphere, these gradients furthermore result in Richardson numbers of the order of magnitude of $\mathcal{O}(1)$, considering the average stratospheric static stability of $\overline{N^2}_{strat.} \approx 4 \cdot 10^{-4}$ s^{-2}. The diffusive turbulence parametrisation in the model acts towards the erosion of the gradients responsible for such low Richardson numbers, with the consequence that Ri approaching Ri_c is increasingly hard to sustain in the model. The significance of this effect is not quantified, and therefore should not be overestimated but rather generally considered. The fact that Ri remains above Ri_c shows that the model is not capable to resolve all processes that result in the observed mixing process. Overall, it proves to be useful to identify exceptional vertical wind shear above the LRT as a first indicator for the tendency towards dynamic instability.

Due to the previous considerations, the threshold value for the identification of the layer of enhanced vertical wind shear is set to $S_t^2 = 4 \cdot 10^{-4}$ s^{-2}. Using this value, the vertical extent of the layer of enhanced vertical wind shear within the ridge of the baroclinic wave (18° W–5° E, 45° N–65° N, compare Fig. 3.2a) averages $\overline{dz} = 511 \pm 206$ m (mean ± one standard deviation). In potential temperature this translates to $\overline{d\Theta} = 9.34 \pm 4.10$ K. The strength and size of the shear layer in the IFS should be regarded with care, since the vertical extent is of the order of the grid spacing at tropopause altitudes.

In conclusion, the layer of enhanced vertical wind shear $S^2 \geq S_t^2$ narrows down the region where shear-induced turbulent mixing can occur above the LRT, according to the IFS forecast. This result will be further expanded in the following analysis chapters.

3.1.3 *Observation-based estimate of the depth of the mixing layer on the basis of a Kelvin-Helmholtz instability*

During WISE RF07 and shortly after the approach of the airplane on the tropopause, Kelvin-Helmholtz billows on top of the cloud deck inside the ridge of the baroclinic wave were observed and photographed (Fig. 3.9a). The mission PI on board took two photographs of the wave train at the same viewing angle of $\phi = 90° + 20 \pm 2°$ relative to the the airplane heading at 15:03 UTC, and with a time offset of $\Delta t = 4 \pm 1$ s between the photographs. This allows an estimation of the horizontal and vertical extend of the billows based on the Exif data of the camera in combination with an analysis of the background flow, inspired by the approach of Reiss and Corona (1977).

At that time where the photographs were taken the airplane was heading 218° from true North and traveling at a true airspeed of $TAS = 235 \pm 5$ m s^{-1} (Fig. 3.9b). The measured wind direction was 50° from North and therefore approximately opposed to the airplane heading. The estimation of the Kelvin-Helmholtz billow size is made under the assumption that the wind measured at the airplane describes the background flow in the vicinity of the airplane and therefore also the orientation of the Kelvin-Helmholtz wave. We furthermore

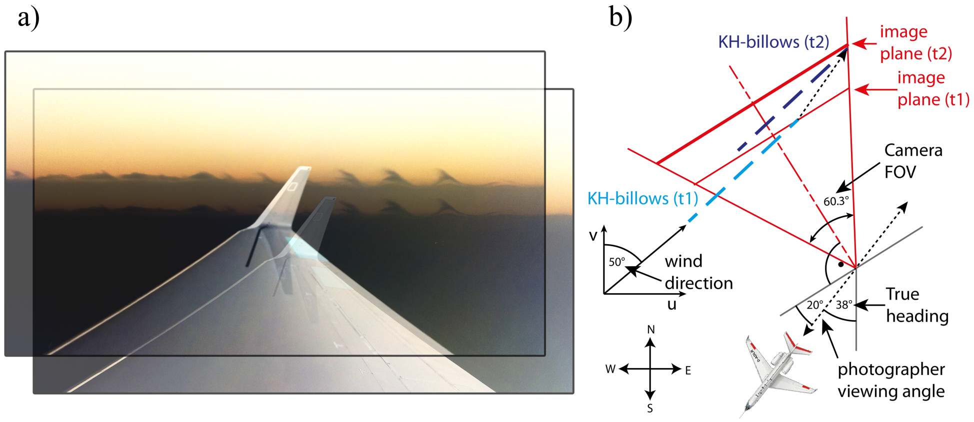

Figure 3.9: a) Composite of the the two post-processed photographs taken at 15:03:43 and 15:03:47 UTC. The displacement is such that the Kelvin-Helmholtz billows align horizontally. b) Schematic of the geometric analysis. Red lines show the cameras field of view and the image plane, blue dashed lines indicate the Kelvin-Helmholtz billows at two time steps.

assume that the dynamics of the wave (e.g. its group velocity relative to the assumed background flow) are negligible with regard to the time step of 4 seconds. The relative horizontal displacement of the wave train in the two photographs is therefore in first-order approximation solely due to to the traveling speed of the airplane relative to the background flow, which is given by the TAS. The two photographs were taken with a horizontal field of view of the camera of $\Phi = 60.3°$ (corresponding to a 31 mm lens on a 35 mm equivalent film/sensor). From the geometric point of view described in this paragraph and depicted in Fig. 3.9b we estimate a horizontal size of the image plane at the location of the wave train of 15 ± 5 km (see Appendix A for further details), which implicates a distance between the Kelvin-Helmholtz billows and the research aircraft of 12.91 ± 4.30 km and a Kelvin-Helmholtz wavelength of $\lambda = 1.26 \pm 0.42$ km. The mixing height of the breaking Kelvin-Helmholtz billows is approximately 0.5λ, based on a geometric estimation in the photographs. The vertical extent of KHI billows relative to the wavelength varies between $0.5 - 0.2\lambda$ in observations and theoretical studies (Fritts and Palmer, 1996; Geerts and Miao, 2010). The estimation of $z = 0.5\lambda$ in Fig. 3.9a translates to a mixing height of 630 ± 210 m.

The mixing height derived from the vertical extent of the KHI billows in the photographs (630 ± 210 m) lies within the range of the vertical extent of the layer of enhanced vertical wind shear in the IFS forecast data (511 ± 206 m, Section 3.1.2). The identification of this layer furthermore proved to be a good indicator for the region that was exposed to quasi-isentropic mixing according to the trace gas measurements. The mixing signal in the trace gas mixing ratios was apparent over a potential temperature range of about 5 K, which is also barely outside the range of $\overline{d\Theta}_{shearlayer} = 9.34 \pm 4.10$ K in the IFS forecast. Thus, the two independent analyses provide a coherent estimate of the height of the mixing. In both cases the underlaying process is shear induced dynamic instability within a layer of enhanced vertical wind shear in the stably stratified flow at the tropopause. The large scale background wind shear is an inherent feature of the jet streak associated with the baroclinic wave, and the mesoscale variability of S^2 is likely forced by enhanced gravity wave activity within the ridge.

3.2 SMALL SCALE INTERNAL MIXING WITHIN THE TIL: WISE RF12

The analysis of the dynamic situation that resulted in the observed quasi-isentropic mixing during WISE RF07 relied on the inclusion of IFS forecast data, due to the lack of vertical gradient measurements of flow properties in the region of interest. The IFS forecast predicted a layer of enhanced vertical wind shear at the tropopause and in the region where a pronounced TIL emerged. This resulted in Richardson numbers of the order of magnitude of $\mathcal{O}(1)$, indicating the potential for dynamic instability, in agreement with the mixing signal in the trace gas measurements as well as the KHI billows that were observed shortly thereafter. However, the analysis indicated that the IFS was barely able to realistically resolve the mesoscale variability of the vertical wind shear in the horizontal, as well as the vertical extent of the layer of enhanced vertical wind shear. The mesoscale variability of S^2 showed dominant structures at scales of the order of the assumed effective horizontal resolution of the IFS, i.e., about 10^2 km. The vertical extent of the layer of enhanced vertical wind shear exhibiting $S^2 \geq S_t^2$ was of the order of the vertical grid spacing of the IFS at LRT altitudes.

Motivated by these limitations of the previous analysis, this Chapter presents a second, similar case study, i.e., a tropopause approach of the research aircraft from above the ridge of a baroclinic wave that was surveyed during WISE RF12. Several well placed flight level changes open up the possibility to derive in situ measurement based quasi-vertical profiles during ascents and descents of the airplane. This allows the comparison of gradient based flow properties in the IFS and in the measurements, i.e., static stability N^2 and vertical wind shear S^2.

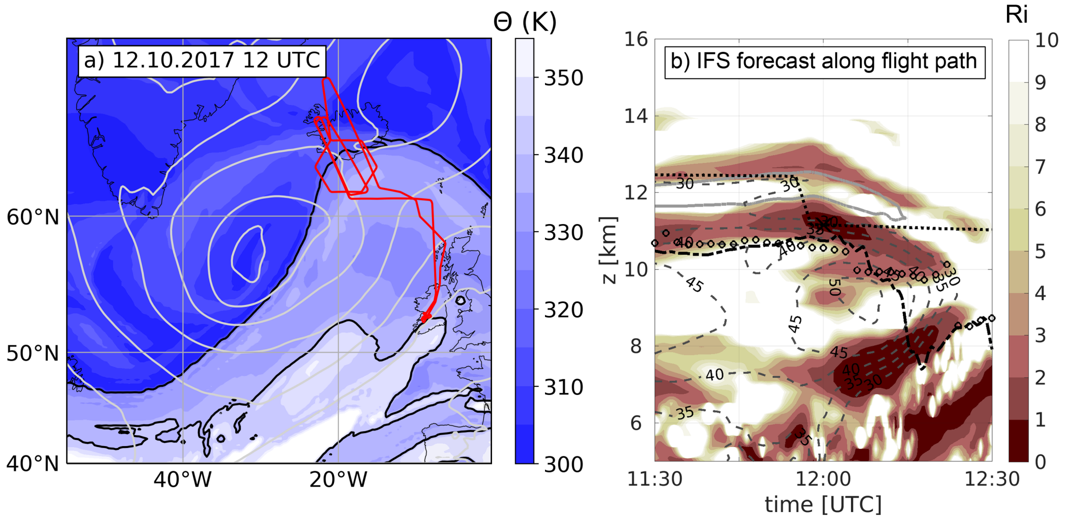

Figure 3.10: Excerpt of the synoptic situation during WISE RF12. a) Potential temperature Θ on the $Q = 2$ pvu dynamic tropopause, on 12 October 2017, at 12 UTC. Contour lines for $\Theta = 320$ and 340 K are highlighted in black. Mean sea level pressure overlay in grey contour lines (MSLP, beginning at 965 hPa in the cyclone centre and in steps of 10 hPa). Flight path of WISE RF12 indicated in red. b) Height-time cross section along the flight path, indicating the Richardson number (Ri, color coded), flight altitude (z_{HALO}, black dotted line), dynamic tropopause ($z(Q = 2$ pvu), black dash-dotted), LRT altitude (z(LRT), circle markers), an isoline of the static stability ($N^2 = 6 \cdot 10^{-4}$ s^{-2}, grey solid line), and isolines of the horizontal wind (u_h, in m s^{-1}, grey dashed lines). All quantities derived from IFS forecast data.

3.2.1 *The synoptic situation during WISE RF12*

On 12 October 2017, the ridge of a baroclinic wave over the North Atlantic reached northward up to Iceland. It was associated with a pronounced surface cyclone southeast of Iceland, with an MSL pressure below 965 hPa (Fig. 3.10a). The first part of the flight path of WISE RF12 comprised of two orthogonal flight legs, first heading northward and then westward, to reach the upper tropospheric front which was situated just south of Iceland. During the westward flight leg, the airplane was flying at FL410 (12.3 km altitude), which according to the IFS forecast was located in the LMS right above a pronounced TIL associated with the ridge (Fig. 3.10b). Before heading northwestwards across the tropopause break at 11:55 UTC, the airplane descended approximately 1 km downwards to FL380, and crossed the TIL structure. The IFS predicted a layer of enhanced vertical wind shear and small Richardson numbers of the order of magnitude of $\mathcal{O}(1)$ located between the tropopause and the TIL, and above the tropospheric jet streak.

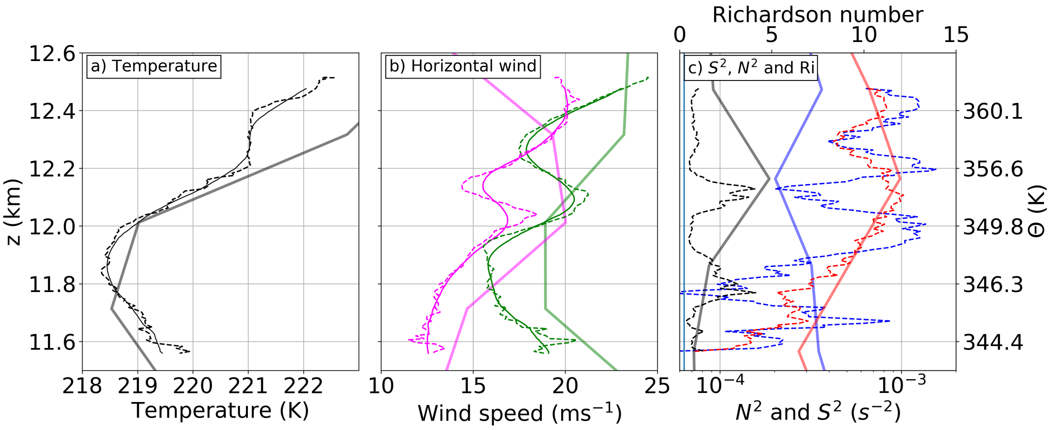

Figure 3.11: Quasi-vertical profiles during the descent from 11:55 to 11:57 UTC during WISE RF12. Solid thick lines show IFS forecast profiles, dashed lines measurements or measurement-derived variables, and solid thin lines 20 second running mean of measurements. a) Air temperature (T, in K). b) Horizontal wind components, u in green, v in magenta ((u/v), in m s^{-1}). c) Vertical shear of the horizontal wind in blue (S^2, in s^{-2}) and static stability in red (N^2, in s^{-2}), on a logarithmic scale. Richardson number in black (Ri, dimensionless). Vertical blue line indicates $Ri = 0.25$. The potential temperature derived from the BAHAMAS measurements is indicated on the rightmost vertical axis.

3.2.2 *Atmospheric flow properties in the ExTL during WISE RF12 and in IFS data*

The (slanted) quasi-vertical profiles from the descent at 11:55 UTC allow the comparison of the in situ measured quantities like the air temperature T and measurement-derived secondary gradient based measures like N^2 and S^2 with the IFS forecast data. Figure 3.11a shows such a comparison of vertical profiles for the air temperature. The basic vertical structure compares well between the IFS and the in situ measurements, however, the BAHAMAS temperature exhibits a more pronounced fine scale structure. The isothermal layer above 12.2 km altitude is the most striking deviation. It exhibits a vertical extent of 200 meter, and results in a local minimum of the static stability N^2 (Fig. 3.11c). Aside from this minimum, the altitude, extent and strength of the N^2 maximum which defines the TIL is well represented in the IFS data, especially when considering the vertical resolution of the model at these altitudes.

The isothermal layer is an indicator for a preceding turbulent mixing event, that took place within the larger scale TIL structure. Turbulent gradient erosion works towards a neutral stratification, i.e., a vanishing vertical potential temperature gradient. The tracer-tracer correlation of N_2O and CO shows a

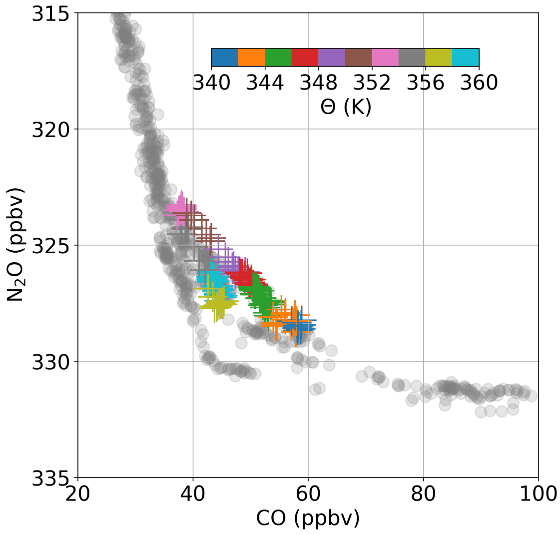

Figure 3.12: Tracer-tracer correlation plot for CO and N_2O during WISE RF12. Grey markers show all measurements within the axis limits, color coded markers only measurements during the descent from 11:55:00 to 11:57:51 UTC. Color code indicates potential temperature at the location of each mixing ratio measurement (Θ, in K).

distinct mixing signal, for the potential temperature range from about 356–360 K, where the isothermal layer is situated (Fig. 3.12). The trace gas mixing ratios clearly deviate from the stratospheric and the tropospheric branch, indicating mixing between the two separated air masses. They furthermore deviate from the mixing line that is apparent in the tracer-tracer correlation for the remainder of the descent, i.e., for the potential temperature range from 340 to about 354 K.

Therefore, the TIL in this region is characterised by a layered structure of two distinct mixing signals in the tracer-tracer correlation, which is also apparent in the vertical temperature profile. This is an important result in the context of the central question of this thesis, i.e., the relation between the TIL and the mixing processes that form and maintain the ExTL. The TIL encountered during WISE RF12 at 11:55–11:57 UTC is quite pronounced, with a a maximum in static stability of $N^2 = 10 \cdot 10^{-4}$ s^{-2} in the measurements as well as in the IFS forecast (compare e.g. the range of the TIL strength within baroclinic waves Pilch Kedzierski et al. (2015) identified in GPS-RO measurements). Thus, the TIL presents a conceptual transport barrier, inihibiting both vertical motion as well as dynamic instability due to strong buoyant forces. Still, the TIL does not exhibit a clear separation between tropospheric and stratospheric tracer-tracer pairs, but instead distinct mixing lines which connect the troposphere and the stratosphere. The TIL emerges within the ridge of a baroclinic wave, a region which is simultaneously exposed to exceptional vertical wind shear at the tropopause, and thus, an enhanced potential for the occurrence of dynamic instability and turbulent mixing. The tracer-tracer correlation of CO and N_2O (Fig. 3.12) exhibits two distinct mixing lines in the tracer-tracer correlation during the descent of the airplane, spanning over $\Delta\Theta = 20$ K in the potential temperature. This further validates that the TIL in this region is and/or was subjected to a spatial and/or temporal succession of turbulent mixing processes.

The vertical profiles of the horizontal wind components give further indications for the potential for turbulent mixing within the TIL. The meridional and the zonal wind profiles exhibit a wave signal with an amplitude of about 2 m s^{-1} and a vertical wave length of 300–400 m. This wave is not resolved in the IFS, and thus, the vertical profiles of S^2 and Ri deviate significantly from the vertical profiles derived from the measurements. The phase relation between the two wind components results in a vertical succession of minima and maxima in S^2, and the according anti-correlated sequence in the Ri profile. Throughout large parts of the TIL, the Richardson numbers approach the critical limit Ri_c. This is for example the case for a layer centred at about 12 km altitude (349.8 K) which exhibits a vertical extent of about 100 m. It is conceivable that the mixing event that took place between 12.2–12.4 km was forced by localised exceptional wind shear within such a small scale wave. However, this remains hypothetical since the measurements remain a snapshot in time with the descent of the airplane taking just about 2.5 minutes, thus only reflecting momentary indicators for preceding and ongoing mixing.

The analysis indicates that the TIL is exposed to a temporal and spatial sequence of internal mixing events on vertical scales of the order of 10^2 m. Intense shear layers that result in dynamic instability can generate small scale gravity waves (Plougonven and Zhang, 2014) which can sharpen the wind gradient in adjacent layers, potentially forcing subsequent dynamically unstable layers. The role of the TIL as a maximum of the refractive index for these internal waves remains to be investigated in the context of the results from Bense (2019).

Finally, it is important to note that while the TIL is largely realistically resolved in the IFS forecast, the vertical wind shear is significantly underestimated due to the small scale wave feature in the wind profiles not being resolved in the model. This implicates an underestimation of the potential for dynamic instability in the LMS.

3.3 SUMMARY

Two central questions were addressed in this chapter:

- *What is the relation between the TIL and the ExTL, and what processes are responsible?*
- *How well does high resolution ECMWF IFS data represent the thermal and dynamic structure of the tropopause region in comparison to airborne observations?*

To approach these questions, two case studies were presented, based on research flights that took place during the WISE campaign and aimed towards these issues. Both research flights surveyed the TIL structure within ridges of baroclinic waves, a region where a strong TIL commonly evolves (Pilch Kedzierski et al., 2015), in agreement with the mechanisms that force a pronounced temperature inversion above the tropopause in this region (Wirth, 2004; Erler and Wirth, 2011; Kunkel et al., 2016).

During the second flight leg of WISE RF07, a tilted tropopause structure above the ridge of the baroclinic wave was approached horizontally from within the stratosphere. At potential temperatures of 335–340 K, the measured trace gas mixing ratios of N_2O and CO indicated quasi-isentropic exchange across mixing lines that connected the tropospheric and the stratospheric branch in the tracer-tracer correlation. The dynamic situation that led to mixing was analysed via a synergistic approach based on in situ measurements as well as high resolution IFS forecast data. The IFS predicted a layer of exceptional vertical wind shear closely above the LRT, which was crossed by the airplane. The enhanced vertical wind shear was associated with the jet streak within the baroclinic wave. The large scale background wind shear was modified by a mesoscale wave perturbation, which was interpreted to be forced by a resolved gravity wave in the model with a horizontal wavelength of the order of the effective resolution of the IFS forecast, i.e., about 10^2 km. The TIL exhibited a mesoscale variability similar to the layer of enhanced vertical wind shear. Enhanced N^2 and enhanced S^2 showed no general co-occurrence, which resulted in a pronounced variability of the Richardson number Ri along the flight path. Ri exhibited a local minimum of the order of magnitude of $\mathcal{O}(1)$ in the region where mixing was evident in the trace gas measurements.

Under consideration of the average stratospheric static stability of $N^2 = 4 \cdot 10^{-4}$ s^{-2} and the dynamic stability criterion the layer of enhanced vertical wind shear above the LRT was identified based on a threshold of $S_t^2 = 4 \cdot 10^{-4}$ s^{-2}. The mixing signal in the trace gas measurements was situated within this layer, which indicated a general agreement between the measurements and the IFS forecast. The mean vertical extent of the layer exhibiting $S^2 \geq S_t^2$ in the IFS forecast was determined to $\overline{dz} = 511 \pm 206$ m respectively $\overline{d\Theta} = 9.34 \pm 4.10$ K. This is of the order of the vertical grid spacing of the IFS at tropopause altitudes, which should be considered when analysing the dynamic stability in this region (compare e.g. the results from Birner et al. (2002) for the ERA Interim reanalysis).

The viability of $S^2 \geq S_t^2$ as an indicator for the potential for dynamic instability was further confirmed through the observation of KHI billows on a cloud deck shortly after the mixing signal in the trace gas measurements. Based on a geometric analysis of two photographs of the KHI billows, their vertical extent was estimated to 630 ± 210 m which is within the range of the height of the layer of enhanced vertical wind shear in the IFS. Despite the good agreement between the different analyses, it was shown that the mesoscale variability and the vertical extent of the layer of enhanced vertical wind shear approached the limit of the resolution capabilities of the IFS.

During WISE RF12 a synoptic situation similar to the one encountered during RF07 was surveyed, and a vertical descent of the research aircraft closely above the LRT through a pronounced TIL allowed the comparison of in situ measured N^2 and S^2 profiles with profiles in the IFS forecast. The analysis revealed that the measured static stability maximum of $N^2 = 10 \cdot 10^{-4}\ \mathrm{s}^{-2}$ which defined the TIL was realistically resolved in the IFS forecast. The vertical wind shear however was significantly underestimated in the model, due to a gravity wave of 300–400 m vertical wavelength that was not resolved in the IFS. Intense vertical wind shear caused by the phase relation between the horizontal wind perturbations resulted in Ri locally approaching Ri_c, indicating the potential for dynamic instability. The tracer-tracer correlation of N_2O and CO revealed a distinct mixing line spanning over the greater part of the vertical profile surveyed, indicating mixing between tropospheric and the stratospheric air. An isothermal layer of 200 m vertical extent was furthermore interpreted as a remainder of a preceding turbulent mixing event within the TIL, which was further confirmed by a second, distinctly separate mixing line in the tracer-tracer correlation.

The analysis of WISE RF07 showed that turbulent mixing and STE occurs within ridges of baroclinic waves, in a region which is characterised by a pronounced TIL. The key result from the analysis of WISE RF12 is that turbulent mixing occurs within the TIL, connecting tropospheric and stratospheric air directly through the maximum of static stability. This puts the results from Kunkel et al. (2016) into a real-life context, who identify the occurrence of enhanced turbulent kinetic energy in the region where a pronounced TIL emerges during idealised baroclinic life cycle simulations. The maximum of static stability that defines the TIL inhibits vertical motion due to the buoyant restoring force that acts on up or downwards displaced air parcels, e.g. through inertial overshooting of tropospheric air at cloud decks which reach up to the tropopause. Furthermore, within the TIL exceptional shear forces are necessary for dynamic instabilities to evolve. Therefore, a pronounced TIL is often thought of as an effective transport barrier between the troposphere and the stratosphere.

In the context of research on STE and the significance of different exchange pathways, the cyclonic shear side of the jet stream is considered to be the dominating region (Pan et al., 2007; Konopka and Pan, 2012), because of the reduced static stability within throughs, PV-streamers and stratospheric intrusions. This agrees with the significantly deeper chemical transition zone observed on the cyclonic side of the jet (Schäfler et al., 2021). The anticyclonic shear side of the jet has gained less attention in this context, since it is associated with a pronounced TIL and thus a strong conceptional transport barrier. It is furthermore characterised by a more abrupt chemical transition between the troposphere and the stratosphere (Pan et al., 2007), which indicates less deep STE. The two case studies presented in this thesis show that turbulent mixing occurs in this region, forced by exceptional wind shear on the anticyclonic shear side of the jet, as well as mesoscale and sub-mesoscale flow perturbation due to gravity waves emitted from source regions like high reaching clouds, cross-frontal circulation, and ageostrophic flow components of the jet streak. The overall significance of turbulent mixing above ridges and within the TIL remains to be quantified. Generally, baroclinic waves are a common feature in the extratropics, where they dominate the large scale flow in the UTLS. During WISE RF07, the IFS forecast predicted enhanced vertical wind shear $S^2 \geq S_t^2$ at the tropopause over large areas of the ridge, as well as pronounced gravity wave activity which was identified based on the divergence of the horizontal wind. Thus, the preconditions for occasional and scattered small scale mixing as observed during WISE RF07 and RF12 are given over large areas, which could contribute significantly to the overall STE budget. Furthermore, it should be considered that mixing at low tropopause altitudes (e.g. Shapiro, 1980) affects a different range of potential temperatures compared to turbulent mixing at elevated tropopause altitudes above ridges. Another important factor is the varying ratio between troposphere-stratosphere transport (TST) and stratosphere-troposphere transport (STT) in different regions and at different altitudes (Sprenger and Wernli, 2003), and the resulting impact on the chemical composition in the troposphere respectively the stratosphere.

4

COMPOSITE ANALYSIS OF THE TROPOPAUSE INVERSION LAYER AND THE TROPOPAUSE SHEAR LAYER IN EXTRATROPICAL BAROCLINIC WAVES

Chapter 3 presented an analysis of the occurrence of a layer of strong vertical wind shear $S^2 \geq 4 \cdot 10^{-4}$ s^{-2} in the region where a pronounced TIL commonly evolves at midlatitudes, i.e., above the tropopause within ridges of baroclinic waves. The observed synoptic scale dipole structure of enhanced (reduced) lower stratospheric static stability above ridges (troughs) agreed with the balanced dynamical forcing mechanism described by Wirth (2004) and further implemented and identified in idealised numerical baroclinic life cycle simulations (Wirth and Szabo, 2007; Erler and Wirth, 2011). The embedded mesoscale variability of the TIL above the ridge was attributed to enhanced gravity wave activity and perturbation of the thermal structure at the tropopause (Kunkel et al., 2014), as well as diabatic processes associated with large scale ascending airstreams (e.g. WCB) and cloud formation up to the tropopause, radiative cooling at the cloud deck, and resulting strenghtening of the temperature inversion which defines the TIL (Kunkel et al., 2016). The occurrence of turbulence and the resulting diffusive erosion of potential temperature gradients can reduce the TIL strength locally, which Kunkel et al. (2016) identified to significantly influence the overall TIL evolution during barclinic life cycle simulations. Despite the agreement of the assumed processes and the observed TIL variability, much of what is known about the temporal evolution of the TIL during baroclinic life cycles is based on idealised numerical simulations of baroclinic waves (Wirth and Szabo, 2007; Erler and Wirth, 2011; Kunkel et al., 2014; Kunkel et al., 2016). This issue is the starting point for the analysis presented in this chapter.

Turbulence can occur as a result of dynamic instability, which evolves above the tropo-pause when strong wind shear overcomes the stabilising buoyant forces associated with the stable stratification in the stratosphere and particuarly whithin the TIL. The analysis of the two case studies of WISE RF07 and RF12 revealed that shear induced turbulent mixing occurs around and within the TIL. The IFS resolved central dynamic features that resulted in dynamic instability, i.e., enhanced large scale background thermal wind shear associated with the jet streaks in the regions of strong baroclinicity as well as the mesoscale variability of the layer of enhanced wind shear which was mainly attributed to resolved gravity waves in the model. The occurrence of intense wind shear in the tropopause region within baroclinic waves is the second central issue of this chapter.

The following Chapter presents a generalised approach to analyse baroclinic life cycles in association with strong surface cyclones in the North Atlantic storm track region, based on IFS analysis data. The analysis fields provide a maximum agreement with the assimilated measurement data, and the analysis presented in this Chapter was identified to not depend the enhanced hourly temporal resolution of the forecast fields, which motivated the choice of the data. The time period analysed spans from beginning of September to the end of November, for the years 2010–2014. The analysis was initiated during the preparation phase for the WISE campaign, which took place during SON over the North Atlantic.

The central question adressed in this chapter is as follows:

- *Does the TIL exhibit similar evolution stages during individual baroclinic life cycles, how do they relate to the evolution of the wind field, and what are consequences for the dynamic stability particularly in the tropopause region?*

First, the cyclone tracking algorithm and the compositing method are explained. Second, a sequence of consecutive case studies is presented, specifically an LC2 wave breaking event (life cycle 2, Thorncroft et al. (1993)), followed by an LC1 wave breaking event which eventually results in a cut-off of stratospheric air. Third, a five year composite analysis of North Atlantic cyclones for the SON season from 2010 to 2014 is presented.

Parts of the following analysis have been published in Kaluza et al. (2019). However, while the focus in Kaluza et al. (2019) is more on the evolution of the TIL in baroclinic life cycles and whether this evolution is similar to predictions from idealised models, the focus of this chapter is additionally on the evolution of the shear layer and its impact on the generation of turbulence.

4.1 CYCLONE TRACKING AND COMPOSITING METHOD

UTLS flow features during breaking baroclinic waves and the evolution of surface cyclones are inherently linked (e.g., Thorncroft et al., 1993). The idea of tracking the UTLS flow feature evolution based on the location of the surface cyclone centre is the core concept of this chapter. A variety of methods have been tried and tested to track surface cyclones, e.g. identifying maxima in the middle or upper troposphere relative vorticity, or local minima in the MSLP field. The IMILAST project (Neu et al., 2013) showed that several methods achieve comparable and reliable results. A testing phase of different approaches eventually led to the MSLP identification algorithm as most appropriate method in terms of accurracy and computational speed for the data used in this analysis. MSLP minima are more unambiguously to identify than minima in the relative vorticity in the high resolution IFS analysis data due to the MSLP field being more smooth. The tracking algorithm is based on Hanley and Caballero (2012), and is adapted to fit the limitations and demands of the geographically limited high resolution data set used. The following paragraphs in this section describe the three central steps of the algorithm: 1) The smoothing of the MSLP fields. 2) The identification of minima. 3) The connection of individual minima from consecutive time steps to identify cyclone tracks in space and time.

A local minimum in the MSLP field is defined as a grid point exhibiting a lower MSLP than its neighbouring 8 grid points. The MSLP fields in this study are processed in a regular latitude longitude grid with 0.25° horizontal grid spacing. Two problems arise from this specification. First, the MSLP often exhibits a pronounced small scale variability and several local minima within one cyclone centre. Second, the latitude-longitude grid is irregular in geometric space due to the convergence of the meridians with increasing latitude. To counteract the first difficulty, the MSLP fields are smoothed by applying a Cressman filter (Cressman, 1959), averaging each grid point in the field with its neighbouring grid points within a radius $r < r_0$ (r_0 being 500 km), using weights of $(r_0^2 - r^2)/(r_0^2 + r^2)$. To work around the second problem, the filtered fields are projected on an area preserving Lambert projection centred at the North Pole, and interpolated onto a regular geometric grid with 28 km horizontal grid spacing, which corresponds to the 0.25° resolution in the latitude-longitude grid at the equator. The algorithm then identifies and saves local minima in the filtered and projected fields, and translates them back to the original MSLP field. Two further criteria are applied: 1) All minima with MSLP $>$ 1007.25 hPa are neglected. This criterium further reduces the amount of local small scale minima in the MSLP field, and replaces the pressure gradient criterium applied in Hanley and Caballero (2012), since the geographical restriction of the data used makes it difficult to consistently calculate pressure gradients. 2) All minima in the MSLP field at a location where the orographic elevation is higher than 1500 m are neglected. This is motivated by the results from the IMILAST project (Neu et al., 2013), as the pressure reduction from high altitudes to mean sea level involves some uncertainty and can produce artificial local minima.

The remaining minima are then connected to cyclone tracks by searching for an associated minimum in consecutive time steps within a certain search radius. For minima associated with a new formed cyclone the search radius in the second time step is 720 km from the position where the cyclone first

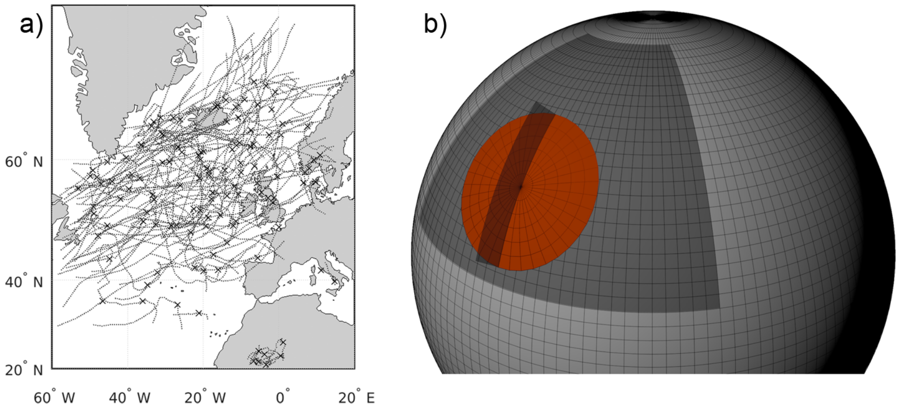

Figure 4.1: a) All 139 cyclone tracks identified in the analysed region. Crosses indicate the location of MSLP along each track. b) Schematic of the size of the analysed region (dark grey) in comparison to the full sphere, as well as the size of a rotated spheric polar coordinate system (orange) with $\Phi_{max} = 15°$ radius. The dark grey semi-transparent upright plane illustrates (with exaggerated vertical extent) the vertical cross-section aligned from north to south as displayed in Fig. 4.11c and d.

appears. Tracks consisting of two time steps or more are extended using a 'first guess' approach (Wernli and Schwierz, 2006), where the first guess is a linear continuation of the preceding track in the regular latitude-longitude grid:

$$\vec{x^*}(t_{n+1}) = \vec{x}(t_n) + 0.75[\vec{x}(t_n) - \vec{x}(t_{n-1})]. \tag{11}$$

Wernli and Schwierz (2006) introduce the factor of 0.75 because cyclone movement tends to get slower during a cyclone's life cycle. The corresponding MSLP minimum is then defined as the closest minimum from $\vec{x^*}(t_{n+1})$ within a radius of 840 km. For more information concerning the values of the search radii and the first guess approach see Hanley and Caballero (2012) and Wernli and Schwierz (2006). Following yet another result from the IMILAST experiment (Neu et al., 2013) only cyclones with a lifetime of at least 24 hours are further considered which translates to at least five 6-hourly time steps in the IFS analysis data. The algorithm furthermore neglects cyclones with less than two time steps before and/or after the global minimum in MSL pressure along their path to make sure that the actual intensification period is covered by the data.

Figure 4.1a shows all tracks identified by the algorithm. The set of tracks consists primarily of extratropical cyclones in the North Atlantic storm track region. The Mediterranean Sea features very few tracks, which is probably due to the upper MSLP threshold of 1007.25 hPa and the fact that cyclones in this region hardly exhibit pronounced MSLP minima. This study focusses on the North Atlantic storm track region, the tracks over North Africa and the Mediterranean Sea are therefore sorted out by a geographical criterium.

The cyclone tracks are ultimately utilised to analyse mean flow features in the UTLS at comparable stages and locations during baroclinic life cycles. For this, composites of the tracks at the time of maximum surface cyclone intensity (defined by global minimum MSLP along the track) are calculated. To work around the irregularity of the original latitude-longitude grid, several measures of interest are interpolated onto a new polar spheric coordinate system with the pole rotated onto the cyclone centre. The new coordinate system exhibits a horizontal grid spacing of 0.25° and a spherical cap radius of $\Phi_{max} = 15°$ (Fig. 4.1b). The rotation of the new coordinate system onto the cyclone centre is performed following Bengtsson et al. (2007), who provide a detailed description of the rotation matrix in their appendix. In such a way, three dimensional data is interpolated onto a pillar centred over the cyclone centre, with an LRT based relative coordinate system and a vertical spacing of $dz = 100$ m, defining the LRT altitude as the zero level and negative (positive) altitude values below (above). A possible tilt of the vertical axis from the surface anomaly up to the LRT is neglected, as well as a potential rotation of the cyclonic structure as a whole based on the direction of migration of the cyclone (e.g., Bengtsson et al., 2007; Catto et al., 2010). The composites are then calculated by averaging over the data from subsets of the pillars of data from the individual cyclones. The mean absolute vertical coordinate is restored by calculating the average LRT altitude at each location in the new polar spherical coordinate system. In the case of quasi-horizontal fields in the UTLS like e.g. the potential vorticity on an isentropic surface $Q(\Theta = const.)$ or the TIL strength N^2_{max} (defined as the maximum in N^2 within 3 km above the local LRT), the fields are first calculated for each cyclone before creating a composite. Another method would be to average primary variables like the temperature T and the pressure p at each grid point in the pillar of data from several cyclones, and calculate secondary measures like $Q(\Theta = \text{const.})$ or N^2_{max} afterwards. While both methods achieve comparable results, the former one preserves more fine scale structure.

4.2 AN EXEMPLARY ANALYSIS OF A SEQUENCE OF CASE STUDIES

4.2.1 *Baroclinic life cycle with LC2 characteristics*

Around the 14th of October 2014 a surface cyclone evolved over the North Atlantic, which reached its absolute minimum in MSLP along its track on the 14th at 06 UTC (Fig. 4.2a). Twenty-four hours before that the UTLS flow above the surface cyclone exhibited a trough of enhanced isentropic potential vorticity (IPV) air originating from high latitudes, and a downstream ridge of low IPV air originating from low latitudes and exhibiting a pronounced tropospheric jet

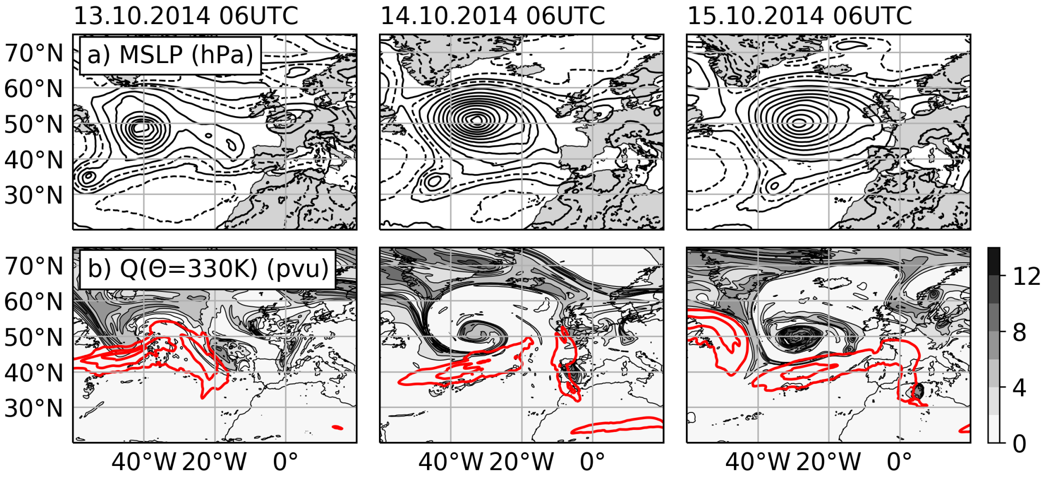

Figure 4.2: Evolution of an LC2 resembling baroclinic wave breaking event, 24 hours before (first column), at (middle column), and 24 hours after the time of maximum surface cyclone intensity (last column). a) MSLP (≤ 1013 hPa solid lines, > 1013 hPa dashed lines, in steps of 5 hPa). b) Isentropic potential vorticity (IPV) at $\Theta = 330$ K ($Q(\Theta = 330\text{ K})$, in pvu), and horizontal wind speed at 200 hPa (u_h, red solid lines from 45 ms^{-1} in steps of 15 ms^{-1}).

streak (Fig. 4.2b). During the intensification of the surface cyclone, the UTLS wave entered what Thorncroft et al. (1993) call the cyclonic wrap-up phase, which in this case meets the definition of an LC2 wave breaking, with the trough remaining on the cyclonic shear side of the jet streak. During the lysis stage of the surface cyclone, the UTLS flow maintained a rotational component, which resulted in an increasing filamentation of the UTLS air masses of different origin.

On a synoptic to planetary scale and during all three time steps depicted in Fig. 4.3, the TIL is more pronounced at lower latitudes. As the surface cyclone intensified and with the progressing wrap-up of ULTS air masses, a pronounced TIL formed within the anticyclonic flow of the ridge, with $N^2 > 10 \cdot 10^{-4}\ \text{s}^{-2}$ at latitudes up to 60° N (Fig. 4.3a and c). The formation of a strong TIL within the ridge agrees with the assumed role of balanced dynamics (Wirth, 2003; Erler and Wirth, 2011), together with diabatic modification of the stratification profile (Kunkel et al., 2016) in regions commonly associated with the outflow of warm conveyor belts (Madonna et al., 2014).

During the progression of the baroclinic wave, the synoptic scale evolution of enhanced vertical wind shear near to the tropopause largely matched the evolution of the TIL (Fig. 4.3b). The ridge featured enhanced values of S^2 approximately of the order of magnitude of N^2, reaching up to high latitudes as

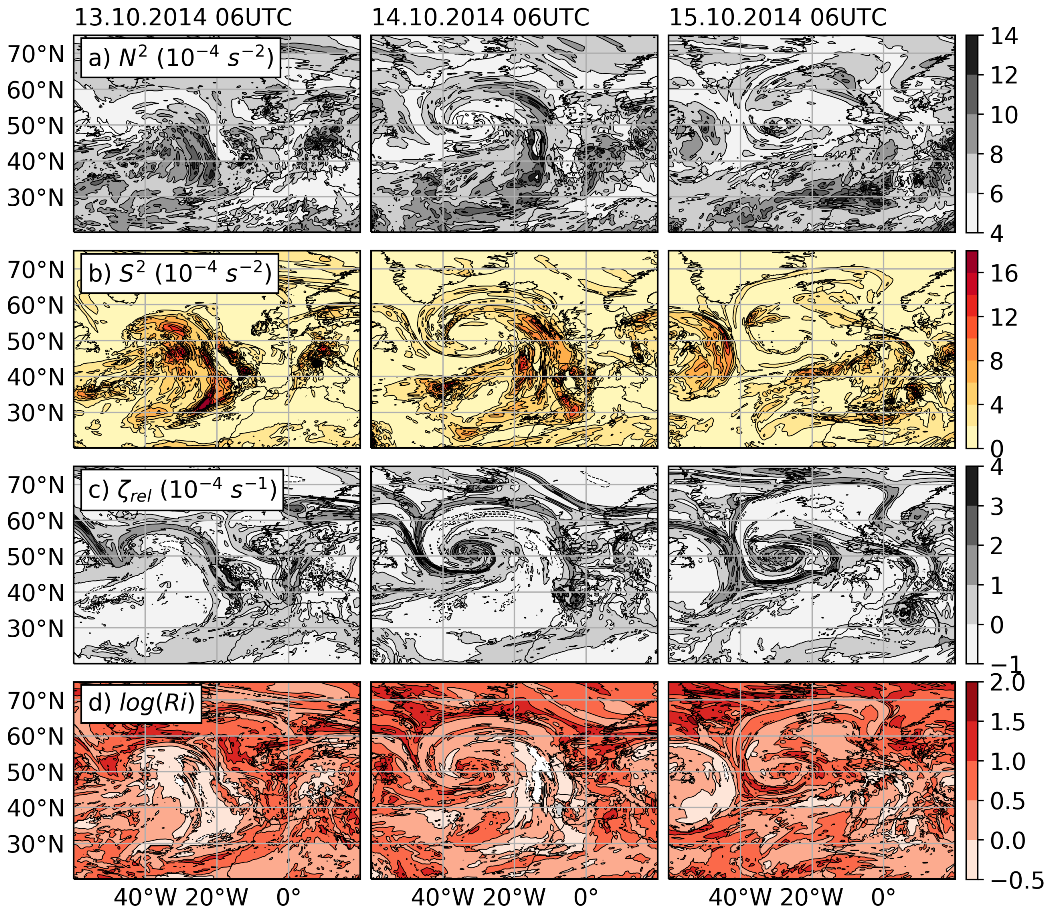

Figure 4.3: As in Fig. 4.2, for a different set of UTLS measures. a) Maximum in static stability within 3 km above the LRT (N^2, in s^{-2}). b) Maximum in vertical shear of the horizontal wind within 1 km vertical distance from the LRT (S^2, in s^{-2}). c) Relative vorticity at LRT altitude (ζ_{rel}, in s^{-1}). d) Richardson number minimum within 3 km above the LRT (Ri_{min})

the wrap-up proceeded and the ridge expanded. The strong vertical wind shear was partly associated with the jet streak south and eastward of the cyclone centre. Regions of intense vertical wind shear furthermore emerged within the wrap-up further northward, indicating a more diverse dynamic structure than just enhanced wind shear above the jet core.

The regions of strong wind shear were associated with comparatively low Richardson numbers of the order of $\mathcal{O}(1)$ in the otherwise dynamically stable LMS (Fig. 4.3d). Eventually, during the lysis stage of the surface cyclone, both N^2 and S^2 reverted to lower values usually evident in the background flow at higher latitudes and remote from the jet stream.

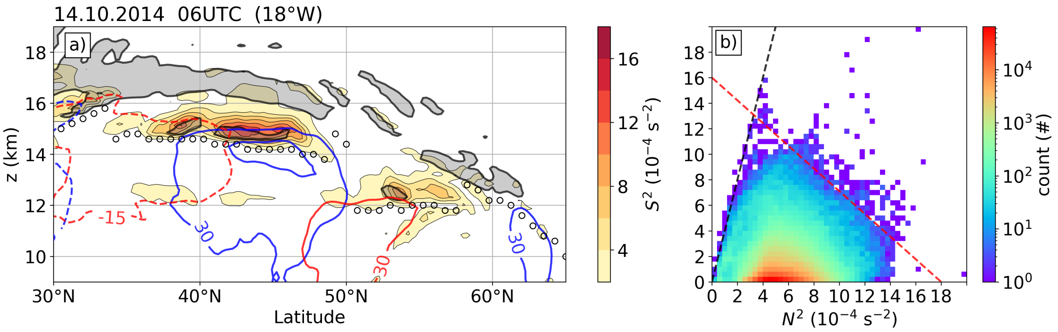

Figure 4.4: a) Vertical cross section on 14 October 2014, 06 UTC at 18° W. Filled contour shows vertical shear of the horizontal wind (S^2, in s^{-2}), black dotted lines isentropes (Θ in K), grey filled contour indicates static stability $N^2 \geq 6 \cdot 10^{-4}$ s^{-2}, blue (red) lines zonal (meridional) wind isotachs (u, v, in ms^{-1}, dashed lines for negative values). Circle markers indicate LRT altitude (z(LRT) in km). b) Two-dimensional histogram of N^2 and S^2 within 3 km above the LRT, on 14 October 2014, 06 UTC and for the region displayed in Fig. 4.3. Colorbar indicates count of grid volumes in the respective N^2-S^2 bin. Black dashed line indicates $Ri = 1/4$. Red dashed line see Section 4.2.1

On the mesoscale, the variability of the thermal and dynamic structure at the tropopause resembled the flow conditions encountered during WISE RF07. Regions of enhanced static stability and intense vertical wind shear generally did not co-occur, which is illustrated for an exemplary vertical cross section at 18° W on 14 October 2014 (Fig. 4.4a). The large scale wind maxima of the flow around the cyclone centre were associated with enhanced vertical wind shear closely above the LRT, particularly above the zonal jet streak at 40°–50° N. The more scattered and less pronounced regions of enhanced vertical wind shear indicate that $S^2 \geq 4 \cdot 10^{-4}$ s^{-2} is not necessarily a jet-bound feature. Vertical wind shear of $S^2 = 4 \cdot 10^{-4}$ s^{-2} over a vertical distance of 500 m (an estimation based on the results of Chapter 3) equals a wind speed difference of $\Delta u_h = 10$ ms^{-1} or less if directional shear is involved. Interestingly, the regions of strong vertical wind shear and the TIL in Fig. 4.4 are clearly separate, which indicates the different forcing mechanisms. For the exceptional vertical wind shear maximum of $S^2 > 12 \cdot 10^{-4}$ s^{-2} above the zonal wind maximum, dynamic stability and thus maintenace of the gradients is ensured through a secondary maximum in static stability, located below the more coherent N^2 structure that would commonly be refered to as the TIL.

The fact that enhanced N^2 and enhanced S^2 generally do not co-occur above the LRT is further illustrated in Fig. 4.4b. The majority of the grid volumes within 3 km above the LRT exhibit static stability between the stratospheric

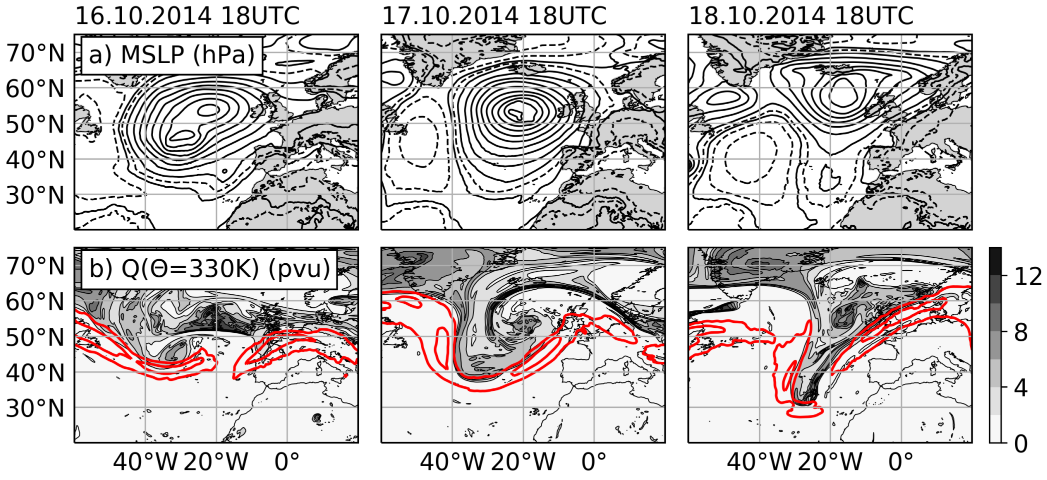

Figure 4.5: As in Fig. 4.2, for the LC1 resembling baroclinic wave breaking event, 24 hours before (first column), at (middle column), and 24 hours after the time of maximum surface cyclone intensity.

background $\overline{N^2}_{strat} = 4 \cdot 10^{-4}$ s^{-2} and moderately enhanced values associated with the TIL. More infrequent N^2 maxima reach up to about $N^2 = 14 \cdot 10^{-4}$ s^{-2}. At the same time, weak vertical wind shear $S^2 < 2 \cdot 10^{-4}$ s^{-2} is most prevalent. Vertical wind shear and static stability do not correlate, and enhanced values of S^2 can be found within the whole spectrum of N^2 under the condition that dynamic stability $Ri > Ri_c$ is maintained. Particularly the largest values of N^2 and S^2 do not correlate, which is indicated by the negative red slope in Fig. 4.4b.

4.2.2 *Baroclinic life cycle with LC1 characteristics*

About two days after the first wave breaking event, a second one took place over the North Atlantic which was again associated with a strong surface cyclone (Fig. 4.5). Initially, the MSLP featured a double minimum, composed of the decaying cyclone centre from the LC2 event and a second one which formed East of Newfoundland. The newly formed surface cyclone migrated across the Atlantic, and a wave pattern emerged in the UTLS flow, which was characterised by strongly filamented tropospheric and stratospheric air due to the presceding wave breaking event. As the surface cyclone intensified and the trough and ridge entered the wrap-up phase, the jet stream split and the trough turned anticyclonically, eventually forming an elongated streamer of enhanced IPV air that stretched down to low latitudes of 30° N. Thorncroft et al. (1993) characterise such a wave breaking event as an LC1 (life cycle 1).

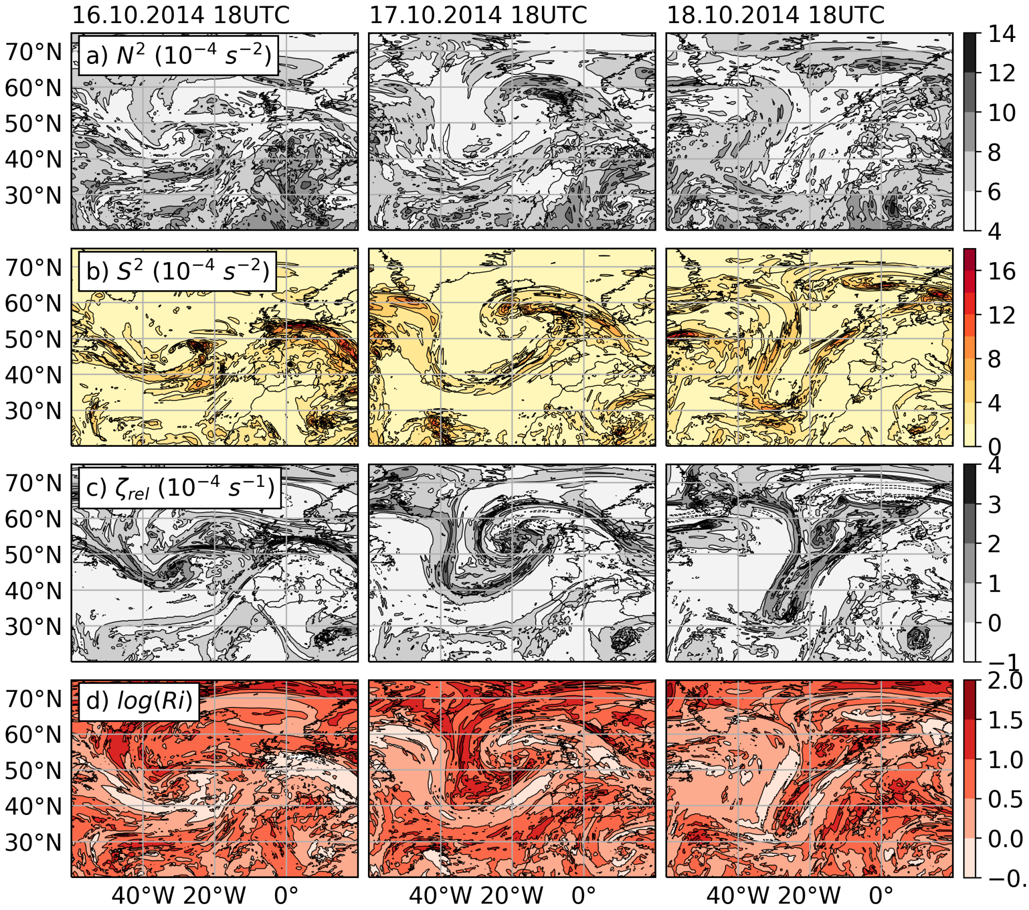

Figure 4.6: As in Fig. 4.3, for the LC1 resembling baroclinic wave breaking event, 24 hours before (first column), at (middle column), and 24 hours after the time of maximum surface cyclone intensity.

The evolution of the TIL and enhanced vertical wind shear at the tropopause (Fig. 4.6) closely resembled the one during the LC2. The anticyclonic UTLS flow in the lowermost stratosphere within the ridge was again dominated by enhanced values of N^2 and S^2 of the same order of magnitude and comparatively low minimum Richardson numbers, in contrast to the trough which was characterised by low values of N^2 and S^2 above the LRT as well as large Richardson numbers. At the time of maximum surface cyclone intensity, minimum Richardson numbers emerged in the vicinity of the jet streak as well as north of the cyclone centre in the outflow reagion of the ascending air streams within the ridge. Both lower stratospheric static stability and vertical wind shear again exhibited a pronounced mesoscale variability. At the last time step depicted, the TIL reverted to lower values at midlatitudes, while the eastern flank of the

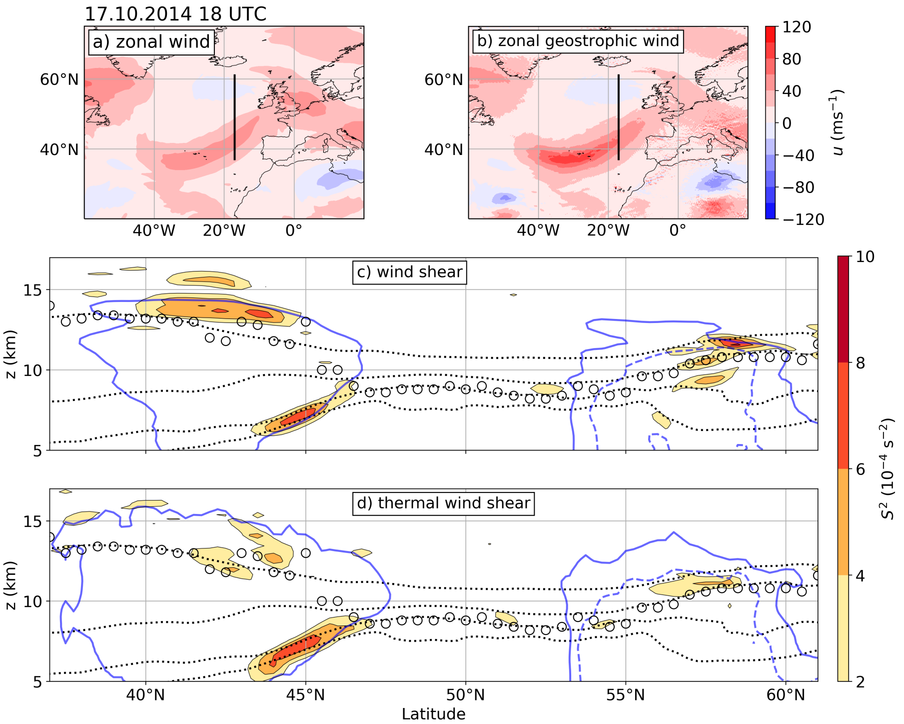

Figure 4.7: Comparison of the horizontal wind and the geostrophic wind, for the time of maximum cyclone intensity of the LC1 case study, i.e., 17 October 2014, 18 UTC. a) Zonal wind at 300 hPa (u, in ms^{-1}). b) Geostrophic zonal wind at 300 hPa (u_g, in ms^{-1}). c) Meridional cross section at 17° W. Vertical wind shear color coded (S^2, in s^{-2}), isentropes black dotted (Θ, 315 K, 320 K, 330 K, 350 K), LRT altitude black circle markers, and zonal wind -10 ms^{-1} (blue dashed) and 0 ms^{-1} respectively 30 ms^{-1} (blue solid) isotachs. d) Thermal wind shear color coded (S^2, in s^{-2}), and zonal geostrophic wind -10 ms^{-1} (blue dashed) and 0 ms^{-1} respectively 30 ms^{-1} (blue solid) isotachs. Isentropes and LRT as in panel c.

IPV streamer remained dominated by enhanced wind shear associated with the jet streak east of the decaying surface cyclone.

At the time of maximum surface cyclone intensity, strong vertical wind shear above the LRT emerged south of the cyclone centre in the vicinity of the jet streak. Additionally, regions of strong wind shear were located north of the cyclone centre, as was the case for the LC2 baroclinic wave. This raises the question of what casues the enhanced vertical wind shear in this region. Figure 4.7a and b indicate that the geostrophic wind presents a good first order approximation of the synoptic scale flow around the cyclone centre. The geostrophic wind overestimates the absolute zonal wind speed, in accordance with the fact that innertial forces of the rotational system are neglected (Holton and Hakim, 2004). Regions of strong vertical wind shear are located south and north of the

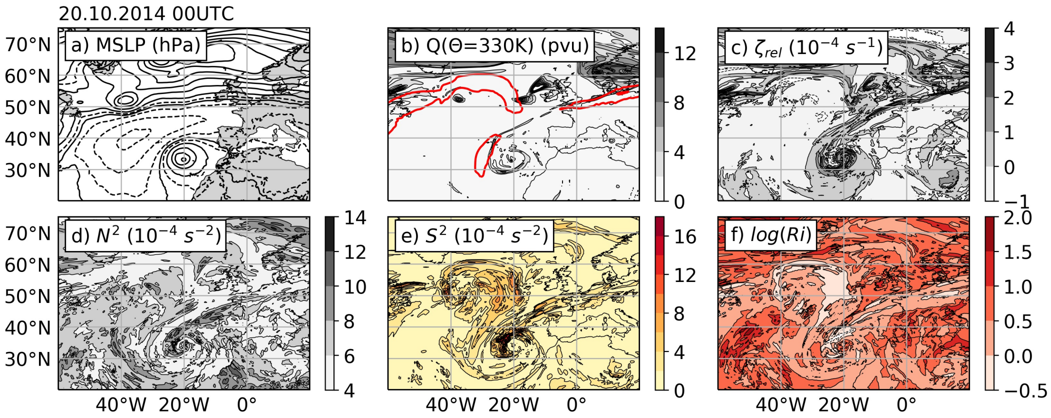

Figure 4.8: As in Fig. 4.2 and Fig. 4.3, for the stratospheric cut-off resulting from the LC1 resembling baroclinic wave breaking event.

trough, and in each case above and below the LRT. Figure 4.7c and d shows a comparison of the total wind shear and the thermal wind shear, i.e., the vertical shear of the geostrophic wind under the assumption of hydrostatic equilibrium. The regions of strong wind shear below the LRT are overall well represented by the thermal wind approximation, with an overestimation at the pronounced upper tropospheric frontal zone at about 45° N and an underestimation at about 65° N. The isentropes that slope downward into the stratosphere above the trough also indicate baroclinicity, thus forcing enhanced thermal wind shear above the LRT north and south of the cyclone centre. In this region, however, the actual vertical wind shear is significantly underestimated, despite the overestimation of the geostrophic wind speed. This indicates the significance of dynamic processes on smaller scales where the assumed approximate equilibrium between pressure gradient force and Coriolis force no longer applies (Newton and Persson, 1962).

The formation of the IPV streamer during the lysis stage of the LC1 eventually resulted in a cut-off of stratospheric air on the $\Theta = 330$ K isosurface, with a surface cyclone evolving underneath (Fig. 4.8). The evolution of the thermal and dynamic structure in the UTLS again resembled the LC1 and the LC2 wave breaking events, where enhanced N^2 and S^2 emerged in the anticyclonic flow within the wrapped up low IPV air, and low Richardson numbers above the LRT particularly north of the cyclone centre.

All three of the described cyclones which emerged consecutively over the North Atlantic exhibited a similar evolution in the UTLS flow features, i.e., the synoptic scale trough-ridge dipole structure of enhanced static stability and enhanced vertical wind shear in the LMS. The point in time of maximum surface cyclone intensity which was identified through the absolute MSLP minimum along the cyclones tracks proved to be a viable indicator for comparable stages of the wrap-up in the UTLS flow, and the linked evolution of TIL and the regions of strong wind shear. These results motivate a further generalised analysis of the thermal and dynamic structure at the tropopause with respect to the wave breaking events in the UTLS. This will be addressed through composites of extratropical cyclones over a five year period in the next subsection.

4.3 COMPOSITE ANALYSIS OF UTLS FLOW FEATURES WITHIN EXTRATROPICAL CYCLONES

The cyclone tracking algorithm introduced in Section 4.1 identified a sum of 130 surface cyclones in the MSLP field within the North Atlantic storm track region and during the SON season in the years 2010–2014. These cyclones satisfy the criteria described in Section 4.1, namely a minimum lifetime of 24 hours with a MSLP minimum of at least 1007.25 hPa. These criteria are not too exclusive, which allows the set of tracked cyclones to contain a spectrum from weak to strong cyclones. The UTLS wave breaking events analysed in Section 4.2 were associated with rather strong surface cyclones, and weaker MSLP minima can be expected to exhibit a less pronounced linkage to the UTLS flow. The tracked cyclones therefore are subdivided into three categories, based on the absolute MSLP minimum along their tracks: The 76 *strong* cyclones with $\mathrm{MSLP}_{min} \leq$ 990 hPa, a subset of the 30 *very strong* cyclones with $\mathrm{MSLP}_{min} \leq 980$ hPa, and the 54 *weak* cyclones with $\mathrm{MSLP}_{min} > 990$ hPa. The composite analysis then focusses on the same UTLS flow features as in Section 4.2, i.e., the distribution of isentropic potential vorticity, the relative vorticity, that static stability and the vertical wind shear, and the resulting Richardson number with the goal to generalise the findings of the case studies.

The composites have been derived following the description in Section 4.1. Figure 4.9 shows composites of the IPV on the $\Theta = 330$ K isosurface and the relative vorticity at LRT altitude for the three subsets of cyclones, with the composites being comprised of the horizontal fields from the individual cyclones at the time of maximum surface cyclone intensity. The comparison of the strong and the very strong cyclones reveals in both cases similar average states of the UTLS flow at the time of maximum surface cyclone intensity. The air masses of different meridional origin and with different IPV are wrapped up around the cyclone centre, and the wind field in the air masses with high IPV amounts to negative values of relative vorticity due to the horizontal shear induced by the jet streak (not shown) as well as due to absolute vorticity conservation during the meridional wave excursion. The wrap-up is overall more pronounced for the subset of the very strong cyclones. The composite derived from the remaining

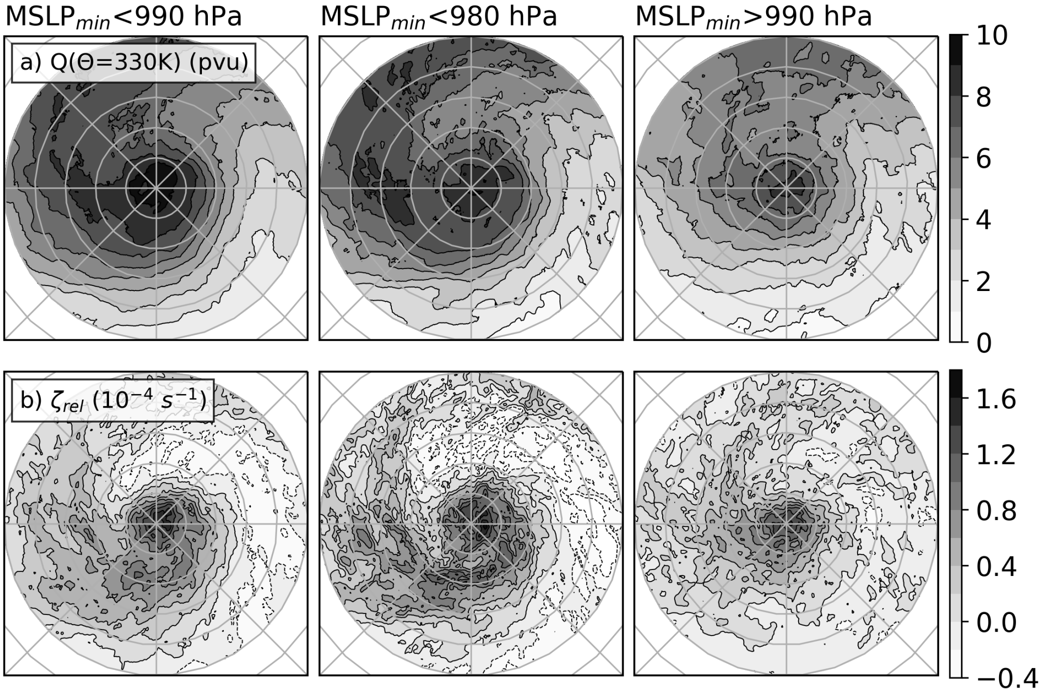

Figure 4.9: Composites of UTLS features derived from subsets of the tracked cyclones, displayed over a radius of 15° around the cyclone centre at the time of maximum surface cyclone intensity. Top column for the 76 strong cyclones with MSLP$_{min}$ $\leq$ 990 hPa, middle column for the 30 very strong cyclones with MSLP$_{min}$ $\leq$ 980 hPa, and bottom row for the 54 weak cyclones with MSLP$_{min}$ $>$ 990 hPa. a) Potential Vorticity at $\Theta = 330$ K ($Q(\Theta = 330$ K), in pvu). b) Relative vorticity at LRT altitude (ζ_{rel}, in s^{-1}).

weak cyclones exhibits a wrap-up around the cyclone centre as well, but less pronounced and with overall weaker gradients.

The quasi-horizontal composites of the TIL strength defined by the maximum in N^2 within 3 km above the local LRT shows a dipole distribution, with a pronounced TIL within the anticyclonic flow of the low IPV air originating from lower latitudes (Fig. 4.10a). The mean TIL strength maximises north/northwest of the cyclone centre, which agrees with the observation from the case studies in Section 4.2. The flow exhibiting positive relative vorticity at tropopause altitudes shows a weak TIL strength, in agreement with what is expected from theoretical considerations as well as idealised baroclinic life cycle experiments. Still, it is interesting that the surface cyclone intensity predicts similar upper tropospheric flow conditions leading up to quite comprehensive composites. The described TIL distribution is evident for all three subsets of

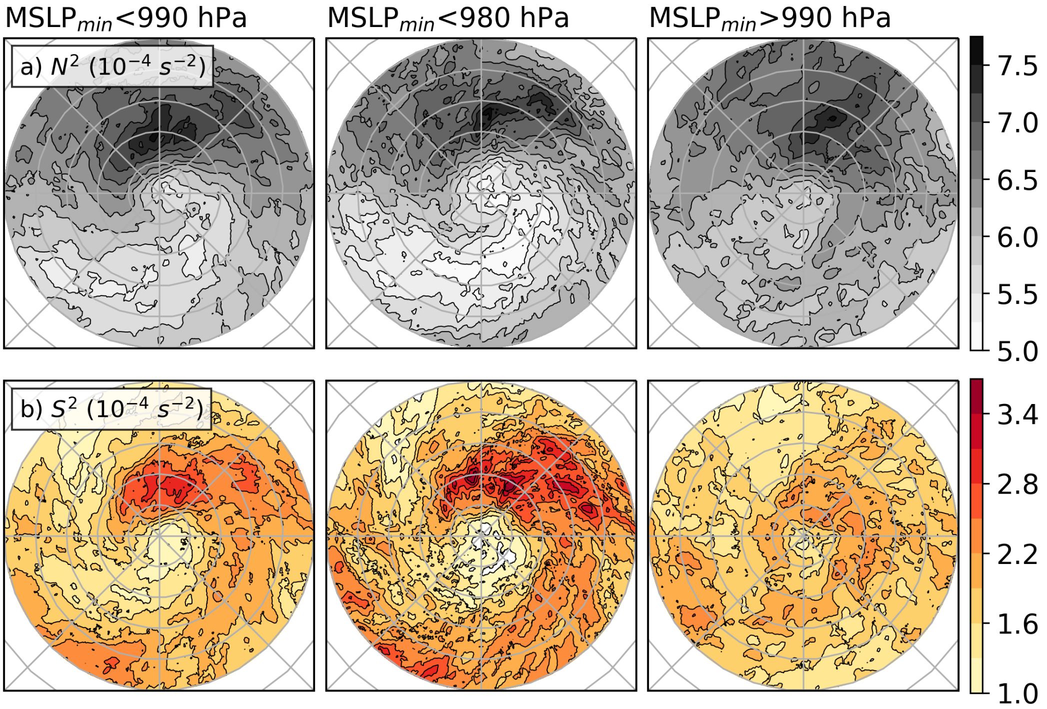

Figure 4.10: As in Fig. 4.9, for different UTLS features. a) Maximum in static stability within 3 km above the LRT (N^2, in s^{-2}). b) Maximum in vertical shear of the horizontal wind within 1 km vertical distance from the LRT (S^2, in s^{-2}), and d) relative vorticity at LRT altitude (ζ_{rel}, in s^{-1}).

cyclones, with sharper gradients and a more pronounced trough-ridge dipole structure for stronger cyclones.

The composite of the maximum in vertical wind shear located in the tropopause region matches the distribution of the TIL strength to a large degree (Fig. 4.10b), analogous to the situation found in the case studies in Section 4.2. The mean wind shear is most intense in the region where the strongest TIL emerges, i.e., north/northeast of the cyclone centre. Again, this should not be interpreted as a co-occurrence of enhanced N^2 and enhanced S^2 due to the dynamic stability criterion. Instead, the analysis reveals a (first of all horizontal) alignment of the processes that lead to the observed enhancement of N^2 and S^2.

Figure 4.11a shows the quasi-horizontal mean of the minimum Richardson numbers found within 3 km vertical distance from the LRT in the UTLS flow associated with the 76 strong cyclones. The tendency towards dynamic instability in the LMS above ridges is apparent, in comparison to the dynamically stable flow within the troughs. The Richardson numbers in general exhibit a large variability due to the nonlinear dependency on the wind gradient, which

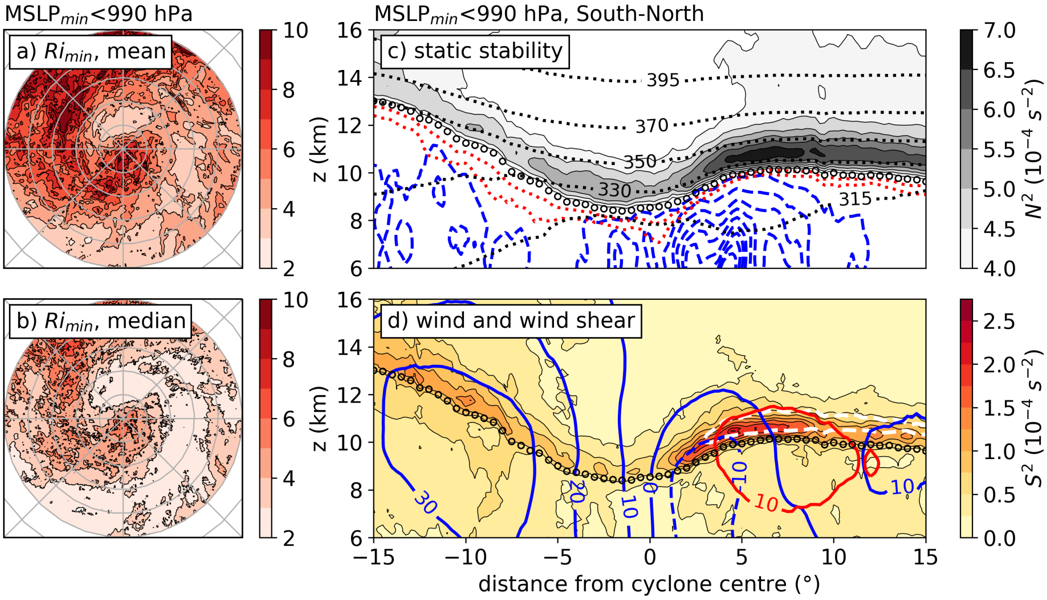

Figure 4.11: a) and b): Quasi-horizontal composites derived from the 76 strong cyclones with MSLP$_{min}$ $\leq$ 990 hPa. a) Mean and b) median value of the minimum Richardson numbers within 3 km above the local LRT ($\overline{Ri}_{min}$, (-)). c) and d): Northward aligned vertical cross sections through the cylcone centre, LRT-based average for the 76 strong cyclones, with mean LRT altitude restored. c) Static stability as filled contour (N^2, in s^{-2}), isentropes as black dotted (Θ, in K), LRT altitude as circle markers (z(LRT), in km), potential vorticity isolines as red dotted ($Q = 2$ pvu and $Q = 3$ pvu), and cloud ice water content as blue dashed lines (CIWC, beginning at $5 \cdot 10^{-6}$ kg/kg and in same steps). d) Vertical shear of the horizontal wind as filled contour (S^2, in s^{-2}), zonal (meridional) wind component in blue (red), positive values solid, negative values dashed lines (u and v, in m/s), dashed white contour $N^2 = 6 \cdot 10^{-4}$ s^{-2} isoline, and LRT altitude as in c).

reduces the validity of a mean value. Birner et al. (2002) introduce an adjusted mean of logarithmic Richardson numbers to counteract the large variability. The median of the minima in Richardson numbers presents another way to analyse the average dynamic stability (Fig. 4.11b). A greater part of the ridge exhibits median values of $\overline{Ri}_{min} \leq 3$, indicating that in this region and area-wide half of the time at least one grid point within 3 km above the local LRT exhibits a Richardson number of $Ri_{min} \leq 3$. The reduced dynamic stability is caused by enhanced vertical wind shear, because the definition of the LRT implicates stable stratification at least within 2 km above the LRT altitude, and the TIL has been identified to maximise in strength in this region.

Figure 4.11c and d further illustrate the average flow conditions in the UTLS in vertical cross section composites, aligned in south-north direction through the cyclone centre. The wrapped up ridge is evident in the elevated LRT altitudes south and north of the cyclone centre where the trough is located. The layer of maximum static stability that defines the TIL is most pronounced at about 5°–10° north of the cyclone centre, and located closely above the LRT. The upper troposphere in this region is dominated by ascending air and ice cloud formation reaching up to the tropopause, which agrees with the anticipated role of latent heat release as well as radiative forcing at the cloud deck on the TIL formation (Kunkel et al., 2016).

The average horizontal wind field agrees particularly with the LC1 case study. The composite exhibits a zonal wind maximum south of the cyclone centre which is associated with the jet stream, as well as tropospheric easterlies north of the cyclone centre with a sharp wind reversal above the tropopause. Static stability N^2 and vertical wind shear S^2 exhibit a similar structure, however, differences are evident as well. The layer of maximum vertical wind shear in the composite is located closer to the LRT and closer to the cyclone centre, where the isentropes slope downward into the stratosphere above the trough. The comparison between the observed wind shear and the thermal wind shear in Section 4.2.2 showed that the vertical gradient of the geostrophic wind underestimates the observed S^2 structure above the LRT, indicating the importance of sub-synoptic scale processes. The regions of enhanced N^2 and S^2 emerge north and northeast of the cyclone centre, in the outflow region of large scale ascending air streams like warm and cold conveyor belts. Enhanced gravity wave activity associated with cloud formation and tropopause gravity wave interaction could contribute to the observed enhancement in static stability and/or wind shear. This could include resolved gravity waves in the model, parametrised gravity wave drag, and residual gradients of gravity wave mean flow interaction in observational data assimilated in the IFS analysis.

4.4 SUMMARY

Chapter 3 described the occurrence of a layer of strong vertical wind shear above the tropopause, within ridges of baroclinic waves that were surveyed during the WISE airborne measurement campaign. The wind shear maximum appeared to be closely linked to the evolution of a pronounced TIL above the ridges, and the analysis of in situ measured trace gas mixing ratios revealed shear induced turbulent mixing around and within the TIL. Chapter 4 aimed at a more generalised analysis of the relation between the TIL and strong vertical wind shear during baroclinic life cycles. The central question adressed was the following:

- *Does the TIL exhibit similar evolution stages during individual baroclinic life cycles, how do they relate to the evolution of the wind field, and what are consequences for the dynamic stability particularly in the tropopause region?*

The case studies of a sequence of wave breaking events, with the first resembling an LC2 and the second an LC1 wave breaking (Thorncroft et al., 1993), showed exemplarily how both the layer of strong vertical wind shear and the layer of enhanced stratification emerge above the LRT of the ridge, as the air masses of different meridional origin and isentropic potential vorticity wrap up cyclonically around the underlaying surface cyclone centre. The point in time of maximum surface cyclone intensity measured by the MSLP minimum along the cyclone tracks proved to be a viable indicator for comparable evolution stages of the wave breaking process in the UTLS flow. Around this time, the flow exhibits a pronounced rotational component around its axis which reaches from the surface cyclone centre up to the tropopause, with strong tropospheric westerlies to the south and easterlies in the north. This results in a wrap-up of the upper tropospheric ridge around the cyclone centre. The LC1 wave breaking eventually resulted in a cut-off of stratospheric IPV at low latitudes, which superimposed with a surface cyclone. This cyclonic system showed similar characterstics in the UTLS compared to the LC1 and LC2, particularly concerning N^2 and S^2 at the time of maximum surface cylcone intensity.

The identification of a common evolution stage based on the minimum of the MSL pressure allowed the preparation of comprehensive composites of UTLS features from 130 cyclones which were tracked for the time period SON 2010–2014. These composites confirmed the representativity of the case studies, particularly the features identified in the UTLS. Therfore, in the following the summary generally refers to both the case studies and the composite analysis.

Overall, the key results of the cyclone tracking and composite analysis are as follows:

- During baroclinic life cycles, the TIL evolves as predicted from idealised numerical simulations and thus according to the forcing mechanisms identified in these studies (Wirth, 2004; Kunkel et al., 2014; Kunkel et al., 2016). The TIL evolution of individual baroclinic life cycles furthermore exhibits a common evolution stage at the time of maximum surface cyclone intensity. During this stage, the upper tropospheric part of the ridge, which is characterised by large IPV, reaches far northward where it exhibits a pronounced TIL particularly north and northeast of the cylcone centre. These regions are associated with the upper tropospheric outflow of large scale ascending air streams like warm conveyor belts, indicating the importance of cloud-related diabatic modification of the temperature profile for the formation of the TIL.

- A layer of strong vertical wind shear emerges above the LRT and largely matches the synoptic scale evolution of the TIL, particularly at the time of maximum surface cyclone intensity. Although these regions of strong vertical wind shear are located in regions of enhanced baroclinicity, it was shown exemplarily for the LC1 wave breaking event that the vertical wind gradients can only partly be explained with the thermal wind relation. This agrees with earlier observations and theoretical considerations on the importance of inertial forces at smaller scales and thus larger Rossby numbers (Newton and Persson, 1962) where the assumption of geostrophic equilibrium does not apply (Holton and Hakim, 2004). In Chapter 3 the variability of S^2 was at least partly attributed to gravity wave perturbation of the flow in the UTLS (compare also (Kunkel et al., 2014)). Localised mesoscale flow deformation, convergence, and differential temperature advection can furthermore result in enhancement of the vertical wind gradient (Ellrod and Knapp, 1992).

- Enhanced N^2 and enhanced vertical wind shear S^2 generally do not co-occur due to the pronounced horizontal mesoscale variability of both features. This indicates the different forcing mechanisms, and particuarly the processes that force the strong wind shear need further investigation. The maximum in vertical wind shear occurs on average below the TIL, and thus closer to the tropopause.

- The regions of strong wind shear above the tropopause are associated with reduced Richardson numbers of the order of $\mathcal{O}(1)$. This indicates the potential for dynamic instability and turbulent mixing under the assumption of further localised wind gradient sharpening, e.g. due to non-resolved small scale wave perturbations, as it was identified for the case studies in Chapter 3.

The implications of the results presented are as follows. Baroclinic waves dominate the large scale flow in the midlatitudes, and play a crucial role concerning the occurrence of cross-isentropic diabatic exchange of air between the troposphere and the stratosphere. The diabatic processes that lead to a material change of PV are turbulence below and above the jet stream (Danielsen, 1968; Shapiro, 1980; Whiteway et al., 2004; Duck and Whiteway, 2005; Trier et al., 2020), radiative forcing particularly above cloud decks (Zierl and Wirth, 1997), cloud formation and latent heat release (Gray, 2006), and convective injection (Homeyer et al., 2014). Turbulence has been identified to contribute significantly to the overall STE budget particularly within baroclinic waves (Spreitzer et al., 2019). Generally, the cyclonic shear side of the jet, which is characterised by low tropopause altitudes and the formation of stratospheric intrusions, is considered the dominating region for turbulent STE. The anticyclonic shear side of the jet, i.e. the ridges of barolinic waves have gained less attention in this context. This is justified by the deeper chemical transition between the troposphere and the stratosphere within troughs, which is ciommonly associated with a weaker stratification in this region, and thus, a weaker transport barrier (Pan et al., 2007).

The composite analysis of baroclinic waves over the North Atlantic showed that ridges are associated with the occurrence of strong wind shear and an increased potential for dynamic instability above the LRT. In this context, it is crucial to factor in the temporal and spatial evolution of baroclinic waves on a spectrum of scales. The point in time of maximum surface cyclone intensity is associated with a synoptic scale co-occurrence of the TIL and a layer of strong vertical wind shear, particularly at high latitudes. The mesoscale variabilty of N^2 and S^2 has significant implications for the dynamic stability in the LMS, resulting in an enhanced potential for the occurrence of dynamic instability and turbulent mixing in the region where a pronounced TIL evolves. These flow conditions are met frequently and over large areas within the ridge. This result further hints towards a possible significant contribution of scattered but frequent small scale turbulent mixing on the formation and maintenance of the ExTL, particularly at comparatively large potential temperatures within ridges of baroclinic waves.

Research on the STE budget commonly relies on the representation of the thermal and dynamic UTLS stucture in numerical models, as well as a realistic parametrisation of the non-resolved diabatic processes that result in STE (e.g., Sprenger and Wernli, 2003; Fueglistaler et al., 2004; Berthet et al., 2007; Hoor et al., 2010; Konopka and Pan, 2012). Therefore, it is often stated that the results from these studies first of all apply to the respective 'model world'. Recently, Spreitzer et al. (2019) showed the significance of shear induced turbulent PV modification in the tropopause region above ridges, based on a current version of the IFS, and thus, a state of the art representation of the atmosphere. The analysis presented in this chapter confirms that the horizontal as well as the vertical resolution is crucial for a realistic representation of the thermal and dynamic structure in the UTLS, due to the identified mesoscale variability of N^2 and S^2 as well as the layered structure of these features.

5

A 10 YEAR NORTHERN HEMISPHERE CLIMATOLOGY OF THE TROPOPAUSE WIND SHEAR LAYER

The composite analysis of baroclinic waves in Chapter 4 showed the systematic occurrence of strong vertical wind shear in a sharply defined layer that is located in close vicinity above the LRT. Conceptually, this agrees with the enhanced static stability in the stratosphere compared to the troposphere which can sustain dynamic stability and thus, the wind gradients. Furthermore, the regions of enhanced baroclinicity at upper level fronts within the waves are associated with enhanced thermal wind shear forcing. However, for the exemplary case study in Chapter 4.2 it was shown that the thermal wind relation does not represent all regions of strong wind shear, which agrees with earlier findings by Newton and Persson (1962) and indicates the importance of inertial forces and sub-synoptic scale processes.

Strong vertical wind shear at the tropopause has been identified in a variety of research studies, based on radiosonde data (Birner et al., 2002; Birner, 2006; Zhang et al., 2015, 2019), mesosphere-stratosphere-troposphere (MST) radar measurements (Vasantha et al., 2002), GPS radio occultation (GPS-RO) profiles (Sunilkumar et al., 2015), and at several locations mainly on the northern hemisphere. The vertical wind shear signal in certain regions has been attributed to to planetary circulation features, e.g., the PFJ and the STJ in the extratropics (Birner, 2006), or the TEJ in the tropics (Sunilkumar et al., 2015). The strong vertical wind shear at the tropopause has been discussed in the context of enhanced baroclinicity and thermal wind shear forcing (Birner, 2006), gravity wave tropopause interaction (Kunkel et al., 2014; Zhang et al., 2015, 2019), and the general concept that exceptional wind shear can occur where enhanced static stability can maintain the shear forces (Liu, 2017).

Several research studies on strong vertical wind shear at the tropopause make use of tropopause-relative vertical averages to disregard the tropopause variability, since the magnitude of S^2 exhibits a pronounced variability, and thus localised maxima are likely smoothed out in conventional averages. Early research on enhanced vertical wind shear by Dvoskin and Sissenwine (1958) as well as the more recent study on turbulence indicators at the tropical tropopause by Sunilkumar et al. (2015) analysed vertical occurrence frequency distributions for certain threshold values of S^2. This approach can be advantageous, because e.g. a zonal and/or temporal average over the trough-ridge dipole structure of baroclinic waves can result in a mean vertical profile of S^2 (or N^2) close to the background state. The vertical occurrence frequency distribution of a threshold retains the information on the occurrence of exceptional signals in the analysed quantity.

The following Chapter presents a comprehensive approach towards an analysis of strong vertical wind shear in the tropopause region, to expand the results of preceding research studies on that matter, as well as the results from Chapter 3 and 4. Throughout the introduction and the analysis sections of this thesis it was motivated to further analyse the temperature- and dynamic structure of the UTLS in state of the art numerical model representations of the atmosphere, because of the significance of processes on spatial scales that have previously not been well resolved in numerical models. The ongoing research on this topic aims towards a general better understanding of the tropopause region, and ultimately the processes that influence the separation efficiency of the tropopause as a conceptual transport barrier. Thus, the central question approached is the following:

- *How does the occurrence of strong vertical wind shear relate to the planetary circulation; what are the forcing mechanisms for the wind shear; and what are possible consequences for cross tropopause transport?*

These questions are addressed using ten years of daily northern hemispheric ERA5 fields to compile a climatology of the occurrence of strong vertical wind shear. The Chapter is structured as follows. First, the data set and the handling of the data is briefly reviewed. Second, the general approach and the metrics are introduced on the basis of a single day analysis. Third, an analysis of the vertical and geographic distribution of the occurrence of strong vertical wind shear in the ten year data set is presented.

Parts of this chapter have been included in a research study that is currently under revision in *Weather and Climate Dynamics* (Kaluza et al., 2021).

5.1 THE ERA5 REANALYSIS AND DATA HANDLING

The analysis presented in this chapter is based on ten years of daily northern hemispheric ERA5 fields (Hersbach et al., 2020), for the period of 1 January 2008 to 31 December 2017. The daily model output is for the time of 00 UTC, and the data is handled on the native vertical hybrid sigma-pressure level, as well as on a regular 0.25° latitude-longitude grid. In the vertical, the data set is reduced to the region from 1.5 km above the orography up to level 37 (counting from level 1 at 1 Pa atmospheric pressure towards the surface), which corresponds to an altitude of about 25 km. Thus, the analysis focusses on the UTLS region and the planetary boundary layer is excluded, as well as the region

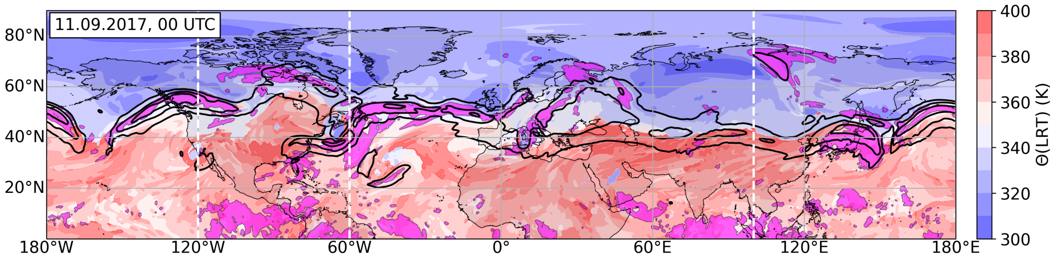

Figure 5.1: Synoptic situation on 11 September 2017, 00 UTC over the northern hemisphere. Color contour shows potential temperature at the LRT ($\Theta(LRT)$, in K), black lines isotachs of the horizontal wind at 200 hPa (from 30 ms^{-1} in steps of 15 ms^{-1}). Magenta shaded areas indicate regions with $S^2 \geq S_t^2$ between 1 km below and 2 km above the local LRT. Dashed white lines indicate the location of the vertical cross-sections in Fig. 5.2.

of the mesosphere-lower thermosphere (MLT) which is frequently exposed to exceptional wind shear (e.g., Liu, 2017).

5.2 IDENTIFICATION OF A TROPOPAUSE WIND SHEAR LAYER ON 11 SEPTEMBER 2017

The introductory single day analysis in this section focusses on the large scale flow on the northern hemisphere on 11 September 2017 (Fig. 5.1). The potential temperature Θ at the LRT exhibits a pronounced meridional gradient, from values of about 380 K at low latitudes to significantly lower values of about 320 K in the polar region. The transition is characterised by a tropopause break in the extratropics, which is sharply defined over the Asian continent and more gradual in other regions, particularly where the flow is disturbed by baroclinic wave activity. The horizontal wind at 200 hPa indicates several jet maxima, i.e., the STJ above the Asian continent at the sharp tropopause break, and individual jet streaks of the PFJ within baroclinic waves at different evolution stages.

The vertical cross sections displayed in Fig. 5.2 further illustrate the strength and location of the jet streams, particularly in relation to the LRT. At 120° W a pronounced PFJ streak is situated at the upper level front of the ridge of a baroclinic wave. The vertical wind shear maximises at the upper edge of the downward sloping tropopause at potential temperatures of about 350 K. At 60° W two distinct westwind maxima are apparent, which can be interpreted as the jet exit region of the STJ and the entry region of a jet streak of the PFJ. Strong vertical wind shear $S^2 \geq S_t^2$ emerges over large areas in close

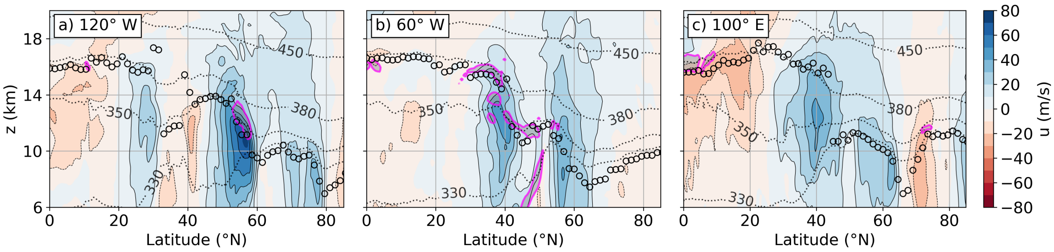

Figure 5.2: Vertical cross section at the latitudes indicated in Fig. 5.1, i.e., a) 120° W, b) 60° W, and c) 100° E. Color contour shows zonal wind speed (u, in ms^{-1}), and magenta contour indicates region of $S^2 \geq 4 \cdot 10^{-4}$ s^{-2}. Black circle markers indicate LRT altitude, and black dotted lines isolines of the potential temperature (Θ, in K).

vicinity of the pertubed tropopause, as well as below the tropopause between the two jet maxima. The wind maximum at 100° E that is centred at about 40° N is associated with the STJ, and here the wind shear does not exceed $S^2 = 4 \cdot 10^{-4}$ s^{-2}. Strong vertical wind shear is located above the elevated LRT at high latitudes associated with a breaking baroclinic wave, and thus in agreement with the results from Chapter 4. The tropical upper tropospheric easterlies furthermore exhibit a region of $S^2 \geq 4 \cdot 10^{-4}$ s^{-2} closely above the LRT.

In the three cross sections displayed, the occurrence of strong wind shear $S^2 \geq 4 \cdot 10^{-4}$ s^{-2} is mostly limited to the region within a few kilometer distance from the LRT. The threshold $S_t^2 = 4 \cdot 10^{-4}$ s^{-2} was previously defined and motivated in Chapter 3, and is taken up again in the further course of this analysis. Figure 5.3 shows the zonal occurrence frequency distribution of $S^2 \geq S_t^2$ for the whole northern hemisphere, to analyse the representativity of the cross sections in Fig. 5.2. Strong vertical wind shear is apparent throughout the UTLS, reaching from the tropics down to high latitudes north of 60° N. The rearrangement of the grid volumes which exhibit $S^2 \geq S_t^2$ into a vertical coordiate system that is based on the distance from LRT reduces the vertical spread of the distribution, and indicates pronounced occurrence frequency maxima in a layer of 1–2 km vertical extent located directly above the LRT. Secondary maxima are apparent below the LRT in the tropics as well as in the extratropics. Thus, the occurrence of strong vertical wind shear $S^2 \geq S_t^2$ is largely limited to the tropopause region.

Returning to the initial point of the analysis, the northern hemispheric geographic distribution of $S^2 \geq S_t^2$ within 1 km below and 2 km above the local LRT on 11 September 2017 is indicated in Fig. 5.1. At high latitudes, strong vertical wind shear emerges at the tropopause above the jet streaks and within the ridges of baroclinic waves at different evolution stages. At lower latitudes,

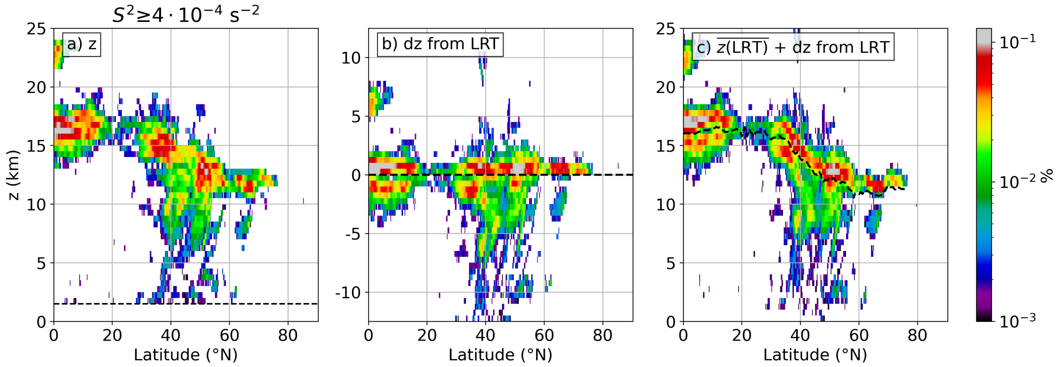

Figure 5.3: Relative occurrence frequency of $S^2 > S_t^2$, zonally averaged over the northern hemisphere on 11 September 2017, at 00 UTC. Logarithmic occurrence frequency contour. Data vertically binned in $dz = 500$ m. a) Absolute height distribution. Dashed black line indicates the effect of the 1.5 km above orography cut-off. b) LRT-relative vertical coordinates. Dashed black line shows LRT altitude. c) As in b) with the average LRT altitude of the vertical profiles with $S^2 \geq S_t^2$ restored.

the STJ features strong vertical wind shear at the tropopause, although not area-wide. In the tropics, large areas of the tropopause region are exposed to strong vertical wind shear, particularly over the Indian ocean and the East Pacific which can be attributed to upper tropospheric easterlies in these regions. Several smaller scale regions of strong vertical wind shear are associated with individual wind systems, like the late stage ex-hurricane Irma over Florida, or the stratospheric cut-off over the Mediterranean Sea.

In summary, the analysis indicated that the occurrence of strong vertical wind shear above the threshold $S_t^2 = 4 \cdot 10^{-4}$ s^{-2} is largely limited to the tropopause region, and that it can be associated with individual features of the planetary circulation. This is the intial point for the following analysis of ten years of ERA5 data.

5.3 TEN YEAR CLIMATOLOGY OF STRONG VERTICAL WIND SHEAR IN THE UTLS

The analysis on the vertical and meridional distribution of strong vertical wind shear in the northern hemisphere is repeated for the whole ten year data set (Fig. 5.4). The occurrence frequency distribution agrees well with the single day analysis. Figure 5.4a shows the 10 year temporal and zonally averaged occurrence frequency distribution for $S^2 \geq S_t^2$ with the geometric altitude as the vertical coordinate, along with the mean LRT altitude. Occurrence frequency maxima are apparent in the midlatitudes, at the tropopause break above and

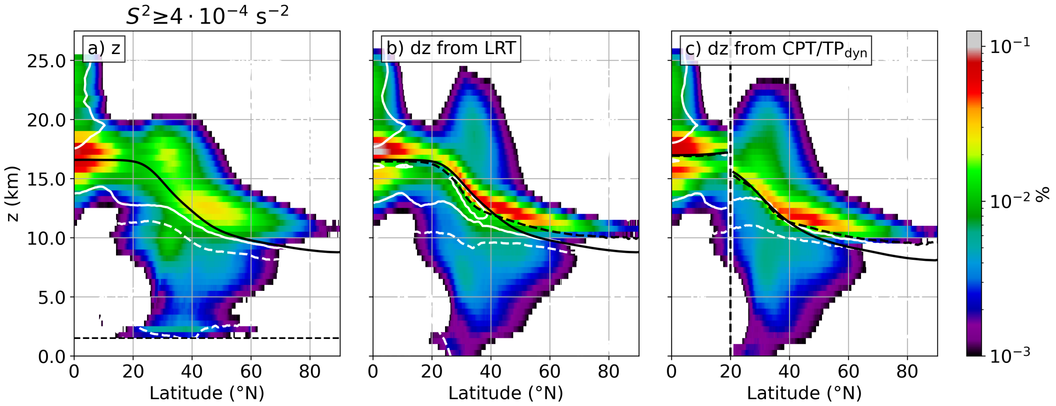

Figure 5.4: Northern hemispheric occurrence frequency distribution of grid volumes that exhibit strong vertical wind shear $S^2 \geq S_t^2$, from 1 January 2008 to 31 December 2017. Logarithmic frequency contour, vertically binned with $dz = 500$ m. a) Geometric altitude as the vertical coordinate. Solid bold black line indicates mean LRT altitude for all 10 years and the whole northern hemisphere. Dashed thin black line indicates the effect of the 1.5 km above orography cut-off. White solid (dotted) line indicates regions where negative (positive) vertical wind shear makes for 75 % of the counts. b) As in panel a, with LRT-relative vertical coordinate and with mean LRT altitude for profiles with $S^2 \geq S_t^2$ restored (dashed bold black line). Solid bold black line as in panel a. c) As in panel b but from $0° - 20°$ N with the cold point tropopause (CPT) as a reference altitude, and north of 20° N with the dynamic tropopause ($Q = 2$ pvu) as a reference altitude.

below the tropopause, and in the tropics. Rearranging the grid volumes in a vertical coordinate based on the distance from the mean LRT altitude (Fig. 5.4b) concentrates the occurrence frequency maxima in a distinct layer above the LRT. This layer reaches from the tropics to latitudes north of 60° N with occurrence frequencies of the order of $1 - 10$ % over a vertical extent of $1 - 2$ km. In the following, the layer of maximum occurrence frequency above the LRT will be referred to as the *tropopause shear layer (TSL)*, borrowing the phrasing from the tropopause inversion layer (TIL). However, it should be kept in mind that the metric applied here is different, since the TIL is commonly defined based on the N^2 maximum above the LRT in tropopause-relative mean profiles.

The tropopopause shear layer (TSL) exhibits maximum occurrence frequencies for $S^2 \geq S_t^2$ in the tropics, where it is characterised mainly by decreasing winds with altitude. Above the TSL, the occurrence of strong vertical wind shear involves positive and negative vertical wind gradients, which is linked to the phase of the quasi-biennial oscillation and the elevation of the level of van-

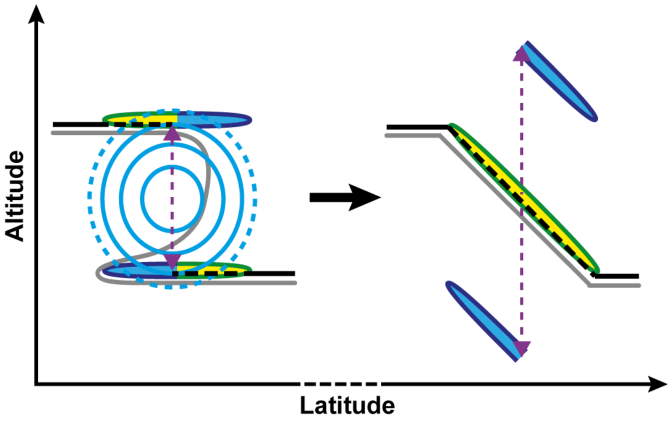

Figure 5.5: Schematical vertical cross section of the tropopause-based averaging method. Left part shows exemplary situation at the tropopause break, right part the key measures after tropopause-based averaging. Black lines indicate the LRT, grey lines the dynamic tropopause. Blue lines show isotachs, and the yellow and blue regions indicate regions of enhanced vertical wind shear above and below the jet core.

ishing horizontal wind. A distinct secondary occurrence frequency maximum for $S^2 \geq S_t^2$ is apparent below the LRT.

At the tropopause break which is located at latitudes of about 30° – 40° N, the TSL is composed more evenly of both positive and negative vertical wind gradients, compared to the remainder of the TSL. This is due to the contribution of decreasing winds with height at the southern upper edge of the tropopause break, as well as increasing winds at its northern lower edge. The large vertical spread of enhanced occurrence frequencies above and below the tropopause break is at least partly explicable with the averaging effect that is illustrated in Fig. 5.5. PV streamers that occur at the lower edge of the tropopause break (Škerlak et al., 2015) are associated with upper level fronts and thus, enhanced wind shear forcing. The PV streamers exhibit a static stability that can sustain dynamic stability for $S^2 \geq S_t^2$, however, they do not meet the LRT definition and thus, the LRT is identified several kilometers above the region of strong wind shear. The tropopause based averaging method then shifts the grid volumes with $S^2 \geq S_t^2$ towards lower altitudes along with the mean LRT altitude that is located somewhere between the upper and the lower edge, due to the overall variability like the meridional meandering motion of the tropopause break. The equivalent effect applies at the upper edge of the tropopause break when regions of strong wind shear reach into the stratosphere at the upper edge of the LMS. Thus, the distance between the occurrence frequency maximum and the LRT of the order of 5 km is correct, however, strong vertical wind shear does not occur frequently at altitudes above 20 km.

In the midlatitudes and north of about 45° N, the TSL is associated with above average LRT altitudes. The zonal mean LRT altitude of vertical profiles that exhibit $S^2 \geq S_t^2$ is located about 1 km above the overal zonally averaged LRT altitude. This indicates the importance of ridges of baroclinic waves, in agreement with the results from Chapter 4.

Figure 5.4b indicates that the occurrence of strong vertical wind shear $S^2 \geq S_t^2$ is closely linked to the stratification criterion that defines the LRT. This agrees with the assumed role of thermal wind shear forcing at upper tropospheric fronts, as well as the dynamic stability restriction which states that wind shear larger than S_t^2 generally can not be maintained in the troposphere. However, the overall link between the tropopause definition and the occurence of strong vertical wind shear remains to quantified. Therefore, the analysis is repeated in vertical coordinates based on other common tropopause definitions, i.e., the cold point tropopause (CPT) in the tropics and the $Q = 2$ pvu dynamic tropopause in the extratropics (Fig. 5.4c). In the tropics the LRT and the CTP are distinctly separated (Seidel et al., 2001), which motivates the comparison in this region. The PV on the other hand does not constitute a usefull definition of a dynamic tropopause in the tropics (Holton, 1995). Therefore, the analysis relative to the dynamic tropopause is limited to the extratropics. Figure 5.4c indicates that the ERA5 reanalysis resolves the separation of the LRT and the CPT, as well as the increasing distance between the tropopauses towards higher latitudes (Seidel et al., 2001). The occurrence frequency for $S^2 \geq S_t^2$ is more evenly distributed above and below the CPT compared to the LRT, which indicates that strong vertical wind shear in the tropics is more closely linked to the LRT. In the extratropics, the analysis relative to the dynamic tropopause (Fig. 5.4c north of 20° N) results in a similar distribution compared to the LRT. However, the layer of maximum occcurrence frequencies above the dynamic tropopause is less sharply defined, particularly above the tropopause break at about 30° N, where the spread is significantly enhanced. This is due to the fact that the dynamic tropopause is identified systematically below the LRT in this region, thus, assigning PV streamers and the associated regions of strong wind shear to the stratosphere. This results in a larger amount of grid volumes which are shifted upwards during the averaging process. In conclusion, the comparison of the averaging method in vertical coordinates relative to the different tropopause definitions reveals that the occurrence of strong wind shear is (not generally but in the overall mean) more closely linked to the LRT compared to the dynamic tropopause and the CPT.

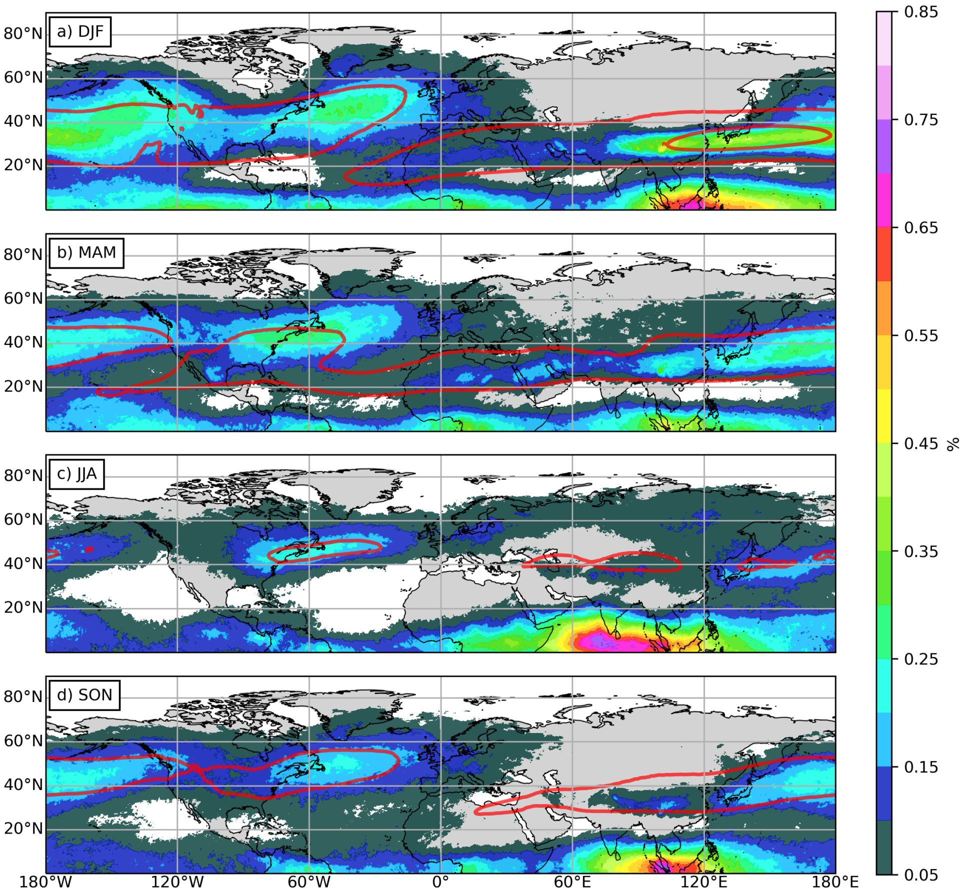

Figure 5.6: Occurrence frequency distribution of $S^2 \geq S_t^2$ between 1 km below and 2 km above the local LRT and in the northern hemisphere. Averaged over 10 years from 2008 to 2017 for a) DJF, b) MAM, c) JJA and d) SON. Red solid lines indicate isolines of the horizontal wind at 200 hPa, starting at 30 m s^{-1} in steps of 30 m s^{-1}.

The geographic occurrence frequency distribution of strong vertical wind shear close to the LRT is shown in Fig. 5.6. A distinct separation of occurrence frequency maxima is apparent throughout all seasons. In the midlatitudes, the tropopause is frequently exposed to $S^2 \geq S_t^2$ in the storm track regions above the North Atlantic and the Northeast Pacific (Shaw et al., 2016). The occurrence frequencies maximise at values of $25 - 30$ % during winter, and decrease by $5 - 10$ % during the summer months where the geographic spread is reduced as well.

At lower latitudes, the occurrence of $S^2 \geq S_t^2$ at the tropopause is linked to the STJ over the Asian continent. The strength of the occurrence frequency maximum agrees with the seasonality of the jet stream, and maximises during winter at values of up to 45 %.

The tropics feature several maxima that span around the equator. During summer, an exceptionally pronounced occurrence frequency maximum is apparent over the Indian Ocean, with values up to 75 %. It is associated with the emergence of the TEJ as an inherent part of the Asian summer Monsoon circulation. During winter, the occurrence frequency maximum shifts eastwards over the maritime continent, where it exhibits a reduced horizontal spread as well as slightly reduced maximum occurrence frequencies compared to the summer months. The occurrence of strong wind shear above the maritime continent during winter is closely linked to the El Niño Southern Oscillation (ENSO) ocean–atmosphere coupling, which will be further adressed in Section 5.3.3.

The following subsections further analyse the individual occurrence frequency maxima for $S^2 \geq S_t^2$ in the context of the associated planetary circulation features, beginning at high latitudes and progressing towards the equator.

5.3.1 *The relation between baroclinic Rossby waves in the midlatitudes and strong wind shear at the tropopause*

In the midlatitudes, the occurrence of strong vertical wind shear in the tropopause region is linked to baroclinic waves and the associated jet streaks. Figure 5.4a revealed above-average LRT altitudes for profiles that exhibit $S^2 \geq S_t^2$, and Chapter 4 identified strong vertical wind shear above the tropopause particularly within ridges of breaking baroclinic waves. The following analysis focusses on this link between the tropopause altitude and the occurrence frequency maxima of $S^2 \geq S_t^2$ in the North Atlantic and North Pacific storm track region.

First, two zonal regions are defined, one which encompasses the occurrence frequency maximum over the North Atlantic, i.e., $80° - 0°$ W, and one over the Northeast Pacific, i.e., $180° - 120°$ W. The latter selection was made in such a way to exclude the STJ maximum, although, a clear separation is not allways achieved, which will become apparent later on. The analysis now makes use of the conservation property of the potential vorticity under adiabatic and frictionless flow conditions (Hoskins, 1991), which is a valid first order approximation for synoptic scale flow. Thus, the meridional excursion of air masses can be identified based on anomalies of the potential temperature on the 2 pvu surface $\Theta(Q = 2 \text{ pvu})$ relative to an unperturbed background state. Ridges of baroclinic waves are associated with a poleward excursion of subtropical air masses and therefore with positive $\Theta(Q = 2 \text{ pvu})$ anomalies, and troughs analogously with polar/subpolar air masses that reach equatorwards, with the 2 pvu surface on comparatively low potential temperatures.

In the following, the unperturbed background state is defined as the ten year zonal and temporal average of the dynamic tropopause, i.e., the potential

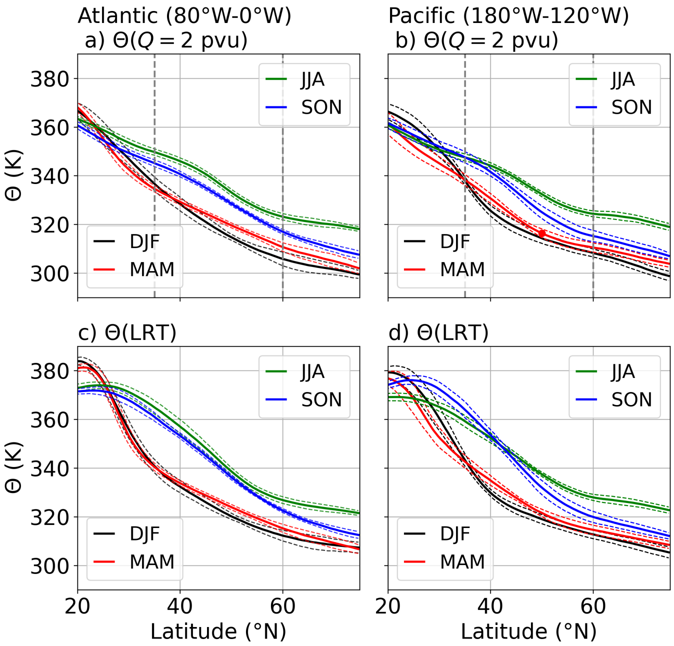

Figure 5.7: a) and b): Seasonal ten year temporally and zonally averaged dynamic tropopause potential temperature ($\overline{\Theta}(Q = 2$ pvu), in K). c) and d): Seasonal ten year temporally and zonally averaged LRT potential temperature ($\overline{\Theta}$(LRT), in K). Solid lines show mean values, dashed lines interannual standard deviation. Left column North Atlantic region (80° W–0° W). Right column Northeast Pacific region (180° W–120° W). Red dot in a indicates $\overline{\Theta}(Q = 2$ pvu) which Fig. 5.8 is referring to.

temperature on the 2 pvu surface $\overline{\Theta}(Q = 2$ pvu), for each region and season individually. This is illustrated in Fig. 5.7a and b. As expected, the dynamic tropopause decreases from comparatively large potential temperatures of about $360 - 380$ K at low latitudes down to potential temperatures between $300 - 320$ K in the polar region. The meridional gradient ist most pronounced during winter and spring. The region between 35° N −60° N is selected, to focus again on the occurrence frequency maxima in the storm track regions which are located within these latitudes. The interannual standard deviation of $\Theta(Q =$ 2 pvu) is generally low in this region, which indicates that $\overline{\Theta}(Q = 2$ pvu) defines a representative background state for each of the ten years.

The merdional progression and the seasonality of the zonally and temporally averaged potential temperature at the LRT (Fig. 5.7c and d) compares well with $\overline{\Theta}(Q = 2$ pvu). The comparison is presented to illustrate the link between the two tropopause definitions, because both are included in the analysis. The occurrence of $S^2 \geq S_t^2$ is analysed based on the distance from the LRT, because according to the results from Chapter 1.3 the increase in static stability at the LRT and strong vertical wind shear are closely linked. The meridional excursion

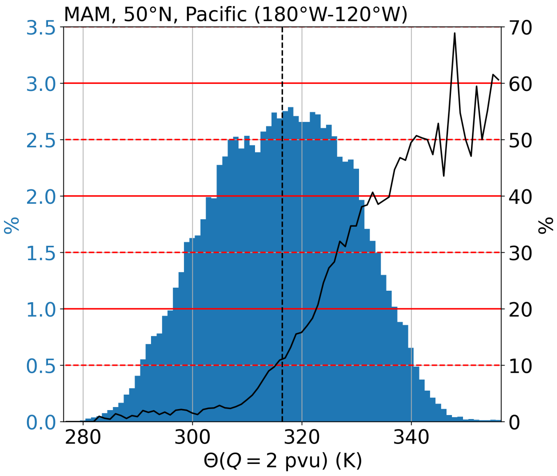

Figure 5.8: Occurrence frequency of $S^2 \geq S_t^2$ within 1 km below and 2 km above the LRT, depending on $\Theta(Q = 2\ \text{pvu})$. Blue histogram shows occurrence frequency distribution of $\Theta(Q = 2\ \text{pvu})$ at 50° N during MAM 2008 – 2017 and averaged over 180° – 120° W. $\Theta(Q = 2\ \text{pvu})$ in 1 K bins. Dashed black line shows mean value $\overline{\Theta}(Q = 2\ \text{pvu}) = 316.4$ K (red dot in Fig. 5.6b). Solid black line shows occurrence frequency for $S^2 \geq S_t^2$ in 1 km vertical distance from the LRT within the $\Theta(Q = 2\ \text{pvu})$ bins.

of UTLS air masses within baroclinic waves is identified on the basis of the dynamic tropopause, because of the conservation property of the PV.

The central step of the analysis is the calculation of instanatneous deviations of $\Theta(Q = 2\ \text{pvu})$ from the previously defined background state, for each region and season and for all ten years. Figure 5.8 shows the results from this analysis step exemplarily at 50° N over the Northeast Pacific and during MAM. The $\Theta(Q = 2\ \text{pvu})$ values exhibit a unimodal distribution around the ten year average background value of $\overline{\Theta}(Q = 2\ \text{pvu}) = 316.4$ K. Strong vertical wind shear $S^2 \geq S_t^2$ at the tropopause however occurs almost exclusively at above-average potential temperatures. The occurrence frequencies for $S^2 \geq S_t^2$ increase up to about 50 % for the largest apparent potential temperatures of the dynamic tropopause.

The analysis is now applied for the whole meridional subsection from 35° – 60° N, over the North Atlantic and the Northeast Pacific region and for all seasons. The result is displayed in Fig. 5.9 where the mean value of the potential temperature $\overline{\Theta}(Q = 2\ \text{pvu})$ has been substracted at each latitude bin of 0.25°:

$$\Delta\Theta(Q = 2\ \text{pvu}) = \Theta(Q = 2\ \text{pvu}) - \overline{\Theta}(Q = 2\ \text{pvu}). \tag{12}$$

The analysis puts the result of Fig. 5.8 into a larger context, and reveals that strong vertical wind shear is generally associated with above-average potential

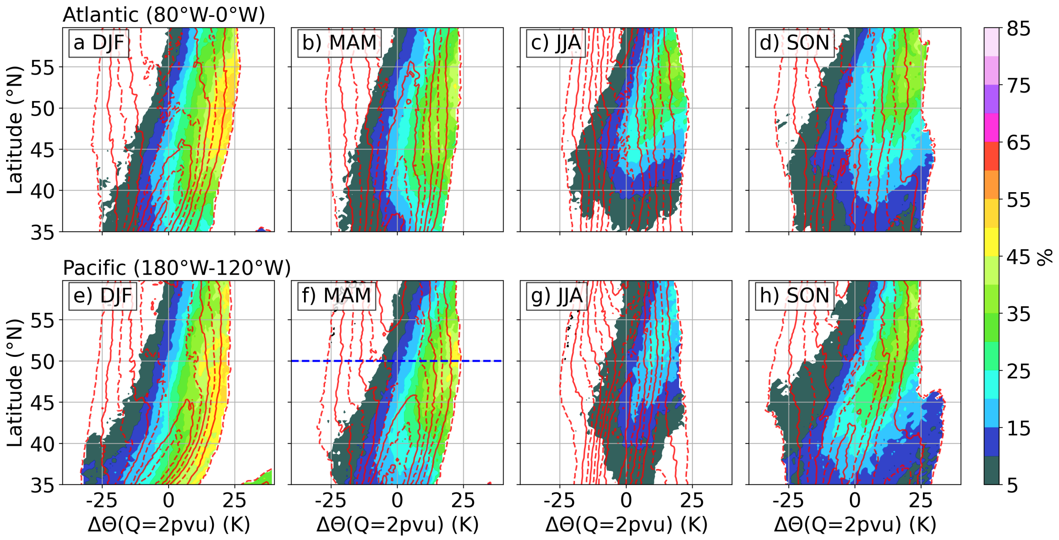

Figure 5.9: Occurrence frequency of $\Delta\Theta(Q = 2\text{ pvu})$ deviations from $\overline{\Theta}(Q = 2\text{ pvu})$ as in Fig. 5.8c, with meridional dependency. Dashed (solid) red lines indicate occurrence frequencies isolines, beginning at 0.5 % (1.0 %) and in steps of 1.0 %. Colour contour shows occurrence frequency for $S^2 \geq S_t^2$ between 1 km below and 2 km above the LRT within the $\Theta(Q = 2\text{ pvu})$ bins. a) to d) DJF MAM JJA SON over the North Atlantic region. e) to h) Same for the Northeast Pacific region. Blue dashed line in f) indicates location of Fig. 5.8.

temperature at the $Q = 2$ pvu surface, and thus primarily ridges of baroclinic waves. The occurrence frequencies for $S^2 \geq S_t^2$ increase with increasing $\Delta\Theta(Q = 2\text{ pvu})$ and at higher latitudes, with peak values of about 50 % at 50° N and $\Delta\Theta(Q = 2\text{ pvu}) = 20$ K.

The connection between strong wind shear, positive $\Delta\Theta(Q = 2\text{ pvu})$, and the meridional location that has been identified for MAM over the Northeast Pacific is evident for all seasons and in both regions. The overall occurrence frequencies for $S^2 \geq S_t^2$ peak during DJF and decrease towards summer, along with a northward shift. Over the Northeast Pacific, the influence of the STJ is apparent, particularly during DJF, where the STJ is most pronounced (Fig. 5.9e). The jet causes a bimodal distribution of $\Delta\Theta(Q = 2\text{ pvu})$ at low latitudes, due to occasional northward excursions the STJ into the region of interest, along with the subtropical tropopause break. This results in the secondary maximum of $\overline{\Theta}(Q = 2\text{ pvu})$ associated with the upper edge of the tropopause break, and shifts the overall average towards larger values of $\overline{\Theta}(Q = 2\text{ pvu})$.

The case studies from Chapter 3 are now briefly put into context of the climatology on the occurrence of strong vertical wind shear within ridges of baroclinic waves. The underlying idea is to estimate the representativity of the

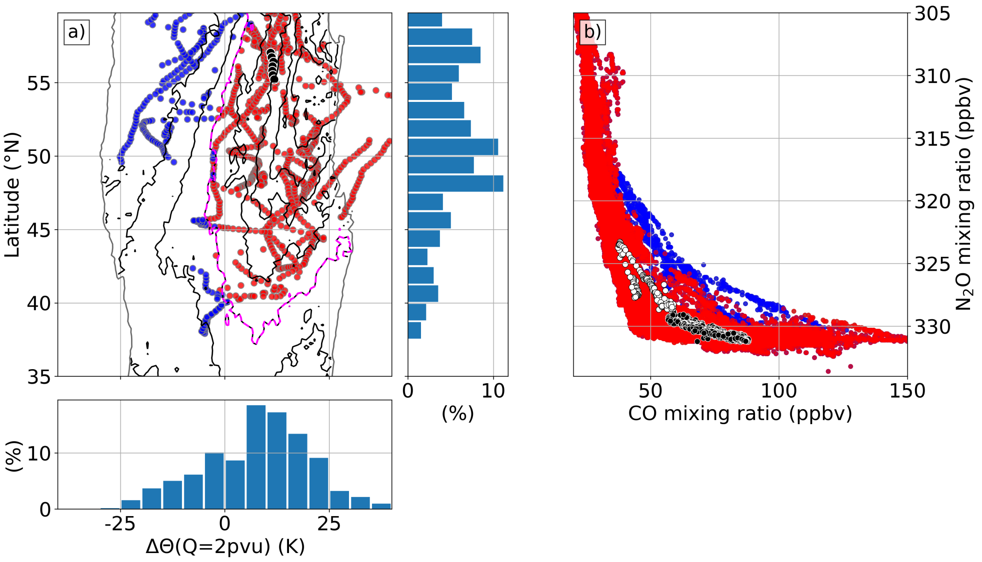

Figure 5.10: a) Black solid contour lines indicate occurrence frequencies for $S^2 \geq S_t^2$ in 1 km vertical distance from the LRT, for SON and over the North Atlantic. Contour lines start at 5 % and progress in steps of 5 % (compare Fig. 5.9d). Circle markers show overlay of measurements from the WISE campaign in the $\Delta\Theta(Q = 2$ pvu)-Latitude space, at reduced frequency for reasons of clarity. Black markers indicate the flight leg from 14:36 to 14:54 UTC during WISE RF07. Red (blue) markers indicate measurements from all WISE flights in regions with occurrence frequencies for $S^2 \geq S_t^2$ larger than (smaller than) 15 %, that were performed within 30 K vertical distance above the tropopause. The 15 % contour is higlighted in magenta. Histograms indicate the relative distribution of measurements performed within each $\Delta\Theta(Q = 2$ pvu)-bin, respectively each latitude bin. b) N_2O-CO tracer-tracer correlation for the flight data displayed in panel a. The descent at 11:55 UTC during WISE RF12 is indicated in white circle markers (These measurements were performed north of 60° N, and thus beyond the range of panel a.

synoptic situations investigated during the research flights, particularly the case studies WISE RF07 and RF12, in the context of the wind shear statistics which were derived in this Chapter. During WISE RF07, a layer of strong vertical wind shear was crossed at latitudes north of 55° N during SON over the North Atlantic, in a region where the $Q = 2$ pvu dynamic tropopause was located at potential temperatures of about 335 K. This is equivalent to a $\Delta\Theta(Q = 2$ pvu$) = 13$ K deviation from the 10 year background SON average of $\overline{\Theta}(Q = 2$ pvu$) = 322.3$ K (Fig. 5.7a). According to the analysis presented in Section 5.3.1, the occurrence frequency for strong vertical wind shear in this region amounts to about 25 %. This is indicated in Fig. 5.10a. The flight leg during WISE RF07 where turbulent mixing was identified is indicated as an overlay in the $\Delta\Theta(Q = 2$ pvu)-Latitude space diagram for SON over the Atlantic (compare Fig. 5.9d). Furthermore, the flight legs from all WISE flights that were located within 30 K potential temperature distance above the tropopause are displayed. The majority of the flight legs closely above the tropopause are located at high latitudes north of 45° N and at above-average dynamic tropopause potential temperatures. This agrees with the central objectives of the WISE campaign, i.e., the investigation of the relation between the ExTL and the TIL in regions where a strong TIL emerges, i.e., northward reaching ridges of baroclinic waves.

The flight legs close to the tropopause are subdivided into two data sets based on the threshold value of 15 % for the occurrence frequencies of $S^2 \geq S_t^2$. The N_2O-CO tracer-tracer correlation shows distinct characteristics for these two data sets (Fig. 5.10b). The trace gas measurements in regions where strong vertical wind shear is uncommon, i.e., mainly within troughs, exhibit several mixing lines which indicate "deep" mixing (Pan et al., 2007). These mixing lines connect with the tropospheric branch at comparatively large CO mixing ratios, thus, contributing characteristic tropospheric air to the mixing process. Equivalently, the mixing lines connect with the stratospheric branch at comparatively low N_2O mixing ratios, thus, indicating the transport of comparatively "old" stratospheric air towards the troposphere. Old or aged stratospheric air refers to air with a long residence time in the stratosphere, which is characterised by reduced N_2O mixing ratios due to photochemical depletion (Birner and Bönisch, 2011). Trace gas measurements in regions where strong vertical wind shear occurs more frequently (> 15 %) are associated with above-average potential temperatures at the dynamic tropopause, i.e., the up- and northward transport of tropospheric air from lower latitudes within ridges of baroclinic waves. The N_2O-CO tracer-tracer correlation of these measurements exhibits mixing lines as well, however, they connect the stratospheric and the tropospheric branch at steeper slopes and at lower CO mixing ratios. This includes the mixing lines which were identified in Chapter 3 for WISE RF07 and RF12. Tropospheric CO mixing ratios generally decrease with altitude and distance from tropospheric source regions. Furthermore, photochemical depletion increases with altitude. The distinction between mixing processes within the ExTL based on the tropopause altitude is a common concept in research on STE within baroclinic waves. The previous paragraph motivated how this approach can be extended based on the wind shear statistics. The aim is to estimate the significance of of the TSL for the formation and maintenance of the ExTL. The concept is presented as an outlook for upcoming research, as a more detailed analysis is beyond the scope of this thesis.

In summary, the analysis revealed a distinct correlation between the potential temperature at the $Q = 2$ pvu surface and the occurrence frequency of $S^2 \geq S_t^2$,

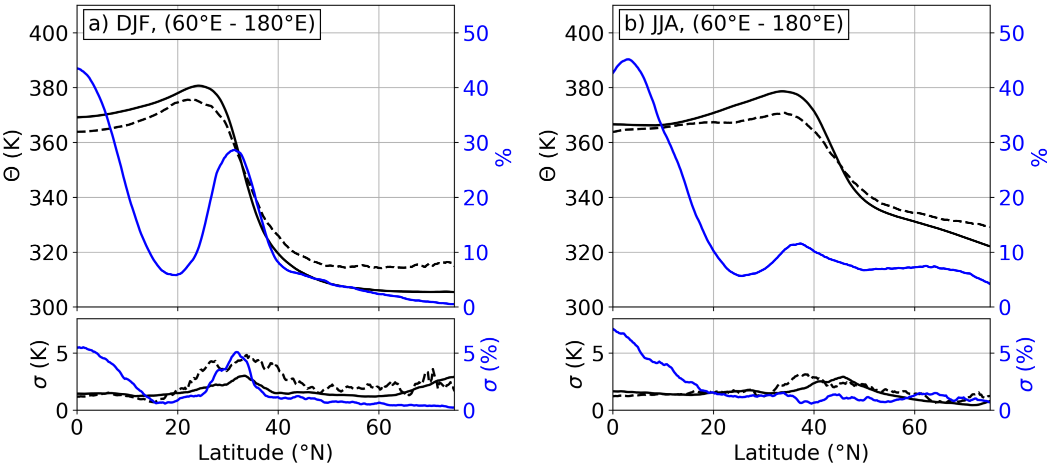

Figure 5.11: Vertical cross sections of ten year average tropopause properties between 60° E and 180° E longitude: a) winter (DJF) and b) summer (JJA). Upper panels: Solid black line shows $\overline{\Theta}$(LRT) for the zonal region. Blue solid line shows zonally averaged occurrence frequency for $S^2 \geq S_t^2$ between 1 km below and 2 km above the local LRT, and dashed solid line depicts $\overline{\Theta}$(LRT) for such vertical profiles. Bottom panels show interannual standard deviation for every measure. The standard deviation of the occurrence frequency displays absolute percentage values.

which confirms that strong vertical wind shear in the midlatitudes emerges primarily at the tropopause within ridges of baroclinic waves. This result agrees with the findings in Chapter 4 and further generalises them.

5.3.2 *The tropopause wind shear layer at the subtropical jet stream*

The analysis of the geographic distribution of strong vertical wind shear at the tropopause revealed a distinct occurrence frequency maximum in the region where the STJ emerges, i.e., over east Asia and the Northwest Pacific. Strong vertical wind shear $S^2 \geq S_t^2$ occurs most frequently in this region during DJF, when the jet stream is most pronounced. The winter STJ over Asia is also referred to as the east Asian jet stream (EAJS). During these months, the tropopause break in the zonal region between $60° - 180°$ E is sharply defined, and the potential temperatures at the LRT decrease from values of the order of $360 - 380$ K south of 30° N to values below 320 K north of 40° N (Fig. 5.11a). The meridional progression of $\overline{\Theta}$(LRT) agrees well with the climatology of Seidel et al. (2001) which is based on radiosonde measurements.

The pronounced tropopause break during winter ist associated with the emergence of the EAJS, along with frequently occurring strong vertical wind shear at the tropopause (Fig. 5.11a). The zonally averaged occurrence frequency for

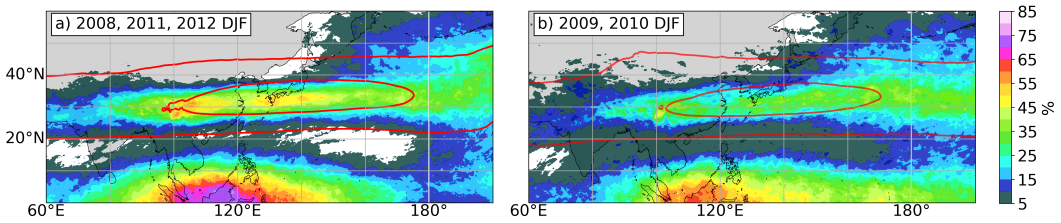

Figure 5.12: As in Fig. 5.6a for a smaller geographical section, averaged over selected DJF seasons of a) west-located EAJS core years (2008, 2011 and 2012), and b) averagely located EAJS core years (2009 and 2010). For further destails see text and Wu and Sun (2017).

$S^2 \geq S_t^2$ between $60° - 180°$ E peaks right at the location of the tropopause break, where it exhibits values approaching 30 %. The interannual standard deviation of the occurrence frequency maximum exhibits absolute values of about 5 %. This variability in the occurrence frequency of strong wind shear at the tropopause can be linked to the variability of the EAJS. In the meridional direction, the location of the EAJS core does not vary much on interannual time scales (Yang et al., 2002), which agrees with the meridionally sharply defined maximum of the zonally averaged occurrence frequencies for $S^2 \geq S_t^2$. The zonal location of the EAJS exhibits a more pronounced interannual variability, as well as the strength of the jet , which has been investigated by Wu and Sun (2017). The authors identified the jet core to be located comparatively far westward during the winter seasons of 2008, 2011 and 2012 (focussing on years that intersect with the data set analysed in this thesis), along with above-average jet core wind speeds. These jet stream characterstics are associated with frequently occurring strong wind shear at the tropopause in the zonal region from 60° E–180° E (Fig. 5.12a). During the winter seasons of 2009 and 2010, the jet core has shifted to the east and exhibits lower maximum wind speeds, which agrees with the reduced occurrence frequencies for $S^2 \geq S_t^2$ between 60° E–180° E (Fig. 5.12b). Despite the general agreement between these basic characterstics of the EAJS and the occurrence of strong vertical wind shear, the direct connection should not be generalised and needs further investigation, e.g. because Wu and Sun (2017) do not see a strong correlation between the zonal EAJS core location and maximum wind speeds. Furthermore, it should be considered that the occurrence of $S^2 \geq S_t^2$ over a limited vertical extent at the tropopause is not necessarily linked to exceptional wind speeds.

During the summer months, the subtropical jet stream over the Asian continent slows down and shifts to the north of the upper-tropospheric Tibetan high pressure system which is associated with the East Asian summer monsoon

(EASM) circulation. The zonally averaged occurrence frequencies for $S^2 \geq S_t^2$ in the vicinity of the LRT decrease to 11 %, and the peak shifts towards the upper edge of the tropopause break (Fig. 5.11b).

5.3.3 *Strong vertical wind shear at the tropical easterly jet*

The exceptional tropical summer maximum of the occurrence frequencies of strong wind shear at the tropopause is associated with the emergence of the tropical easterly jet (TEJ). The TEJ is characterised by upper tropospheric easterlies of up to 40 ms^{-1} that arise from June to September at altitudes of about 150 hPa below the tropical tropopause (Krishnamurti and Bhalme, 1976). The occurrence of the TEJ core is associated with the EASM circulation. The tropopause region above the TEJ is exposed to strong vertical wind shear $S^2 \geq S_t^2$ up to 70 % of the time and over large areas above the Indian ocean, according to Fig. 5.6c. The zonal average of this occurrence frequency maximum exhibits a pronounced interannual variability (Fig. 5.11b). This agrees with the findings from (Roja Raman et al., 2009) who analysed the vertical shear of the zonal wind at different heights above the TEJ core based on MST radar measurements and radiosonde data. The occurrence frequencies for $S^2 \geq S_t^2$ at the LRT which are displayed in Fig. 5.6c furthermore agree qualitatively well with the results from Sunilkumar et al., 2015. The authors of said study analysed vertical occurrence frequency distributions of the vertical wind shear above certain threshold values, at two radiosonde stations which are located at Trivandrum (8.3° N, 76.6° E) and Gadanki (13.5° N, 79.2° E). They identified occurrence frequencies of almost 80 % for $S^2 > 2.25 \times 10^{-4}\ \mathrm{s}^{-2}$ at Trivandrum and 67 % at Gadanki, respectively 37 % for $S^2 > 9.0 \times 10^{-4}\ \mathrm{s}^{-2}$ at Trivandrum and 15 % at Gadanki. These peak values emerged as a sharp maximum above the convective tropopause (COT) and close to the cold point tropopause (CPT), with the LRT generally located in between (Sunilkumar et al., 2013).

5.3.4 *The Pacific winter Walker circulation cell*

During the winter months, the tropical occurrence frequency maximum for $S^2 \geq S_t^2$ shifts towards the east where it is located above the maritime continent and exhibits $5 - 10$ % lower maximum occurrence frequencies over a smaller area compared to the summer TEJ maximum (Fig. 5.6a). The pronounced interannual variability of the occurrence of strong vertical wind shear in this region as well as the season and geographical location of its occurrence indicate a link to the El Niño Southern Oscillation (ENSO) ocean–atmosphere coupling within the Pacific Walker circulation cell.

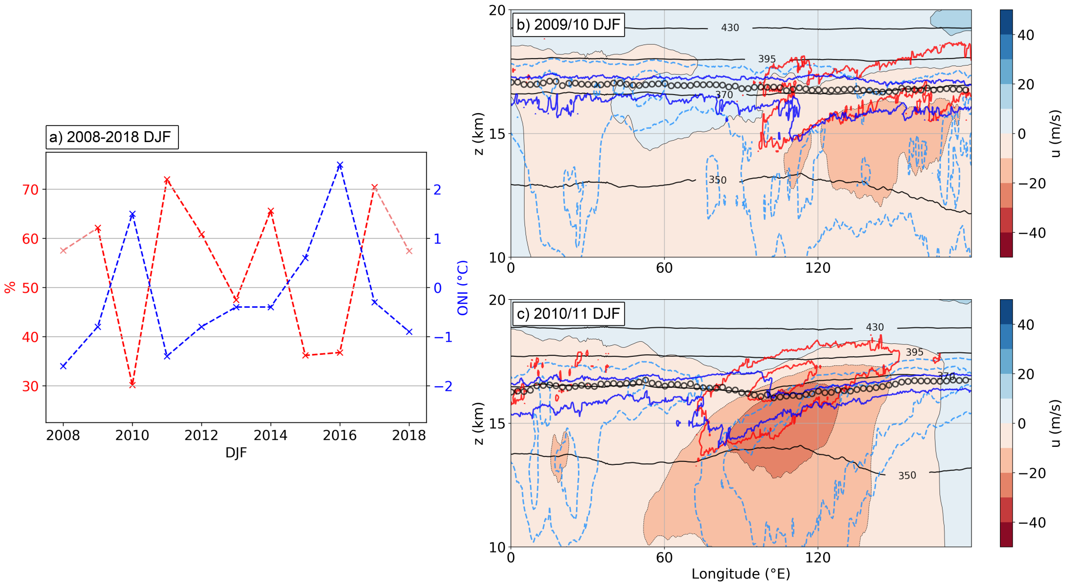

Figure 5.13: a) Comparison of the Oceanic Niño sea surface temperature anomaly Index for DJF (ONI, blue graph) with the strong shear occurrence frequency during DJF averaged over the region from 100° E to 130° E and from the equator to 10° N (red graph). The values for January–February 2008 and December 2017 are included (light red). ONI values from https://www.noaa.gov/. b) and c) Temporal mean of a zonal cross-section at the equator, averaged in geometric height coordinates, for the two consecutive DJF seasons 2009/10 and 2010/11. Color contour shows mean zonal wind component (u, in m s^{-1}). Red solid lines show the 10 % and the 50 % isolines of occurrence frequencies for $S^2 \geq S_t^2$. Blue solid lines show the 10 % and the 50 % isolines of occurrence frequencies for $N^2 \geq 4 \cdot 10^{-4}$ s^{-2}. Black circle markers indicate LRT altitude, and black solid lines show isolines of potential temperature (Θ, in K). Light blue dashed lines indicate the isolines of 70 % and 85 % relative humidity over ice.

To test this hypothesis, the average occurrence frequencies for strong vertical wind shear in the tropopause region above the maritime continent are compared with the Oceanic Niño sea surface temperature anomaly Index (ONI) as a measure for the ENSO phase. The occurrence frequencies are averaged over the area from 100° E to 130° E and from the equator to 10° N, and the results are shown in Fig. 5.13a. The interannual progression of the two quantities shows an anticorrlation, with average to large occurrence frequencies of $S^2 \geq S_t^2$ during neutral and La Niña phases with a pronounced peak during the strong La Niña phase of 2010/11. The positive sea surface temperature (SST) anomaly in the West Pacific during La Niña is associated with enhanced convection over the maritime continent. The intense large scale convective lifting and the enhanced upper tropospheric outflow results in pronounced and localised upper tropospheric eaterlies, which are linked to the frequent occurrence of strong vertical wind shear at the tropical tropopause. The convective outflow region is associated with enhanced gravity wave activity, as convection is the primary source for gravity wave generation in the tropics through several forcing mechanisms (Müller et al. (2018) and therein). The interaction between gravity waves and the tropopause could contribute to the exceptionally frequent occurrence of strong vertical wind shear above the maritime continent, considering the fact that the upper tropospheric easterlies exhibit on average comparatively low maximum wind speeds.

The pronounced El Niño phases during DJF 2009/10 and 2015/16 are associated with significantly below-average occurrence frequencies for strong vertical wind shear at the tropopause, i.e. about 20 % below the 10 year average of 54.2 %. This is linked to the eastward shift of the rising branch of the Walker circualtion cell along with the SST anomaly (Sullivan et al., 2019). The convection occurs less localised over the Pacific ocean and the upper tropospheric easterlies which are associated with the convective outflow are less pronounced. Thus, strong vertical wind shear occurs less frequently, particularly above the maritime continent (Fig. 5.13c).

At the beginning of Chapter 5.3, the ten year zonally averaged occurrence frequency of $S^2 \geq S_t^2$ revealed a distinct secondary maximum below the tropical LRT, which was noticably separate from the TSL above the LRT. Figure 5.13c indicates how this secondary maximum comes to existence, which is now briefly reviewed. The upper tropospheric easterlies above the maritime continent are associated with a frequently occurring lapse rate tropopause jump over a vertical distance of about $500 - 1000$ m, which is located at the western edge of the easterlies. The region below the upper edge of this small scale tropopause break is frequently exposed to enhanced static stability along with strong vertical wind shear, thus, sustaining dynamic stability. The zonal averaging then results in two distinct maxima, one above the LRT which follows the downward sloping LRT in easterly direction, and one below the LRT which includes all wind shear regions east of the tropopause break. The TEJ exhibits comparable characteristics, thus, the explanation which was given for DJF is analogous for the summer months.

5.4 SUMMARY

The objective of Chapter 5 was a comprehensive analysis on the occurrence of strong vertical wind shear in the northern hemispheric tropopause region. This was motivated by the results from Chapter 4 concerning the occurrence of enhanced vertical wind shear above the LRT within ridges of breaking baroclinic waves, as well as the variety of research studies that identified the frequent occurrence of exceptional vertical wind shear closely above the lapse rate tropopause (e.g., Birner et al., 2002; Sunilkumar et al., 2015; Liu, 2017; Zhang et al., 2019). Strong vertical wind shear is a prerequisite for turbulent mixing to occur in stably stratified flow, i.e., above the tropopause, and its occurrence might be linked to the formation and maintenance of the extratropical transition layer. Therefore, the central question which was adressed was the following:

- *How does the occurrence of strong vertical wind shear relate to the planetary circulation; what are the forcing mechanisms for the wind shear; and what are possible consequences for cross tropopause transport?*

This question was approached using ten years of daily northern hemispheric ERA5 fields as a comprehensive state of the art representation of the atmospheric state. The data set was analysed for the occurrence of strong vertical wind shear S^2 above the threshold value of $S_t^2 = 4 \cdot 10^{-4}$ s^{-2}, in a tropopause-relative vertical coordinate system. The treshold value was motivated based on two considerations. 1) The mean static stability in the troposphere can not sustain vertical wind shear larger than S_t^2 due to the dynamic stability criterion. 2) Stratospheric vertical wind shear $S^2 \geq S_t^2$ results in Richardson numbers of the order of $\mathcal{O}(1)$, considering the average stratospheric static stability of $\overline{N^2}_{strat} = 4 \cdot 10^{-4}$ s^{-2}, an thus close to the critical limit $Ri_c = 1/4$.

The analysis identified a pronounced occurrence frequency maximum for $S^2 \geq S_t^2$ within a sharply defined layer of 1–2 km vertical extent located closely above the LRT, reaching from the tropics down to latitudes larger than 60° N, which motivated the defintion of a tropopause wind shear layer (TSL). The geographic distribution of the occurrence of strong vertical wind shear at the tropopause showed several distinct occurrence frequency maxima, which can be attributed to planetary circulation features, i.e., the jet streaks of the polar front jet and the rotational wind systems within differently evolved baroclinic waves, the subtropical jet stream, and the upper tropospheric easterlies associated with the Walker circulation cells. The key aspects of the link between strong vertical wind shear an the planetary circulation are as follows:

- Strong vertical wind shear occurrs frequently at the tropopause within the storm track regions in the Northeast Pacific and the North Atlantic. It occurrs almost exclusively at above average tropopause altitudes, and thus mainly within ridges of baroclinic waves, in agreement with the results from Chapter 4. The latitudinal excursion of air masses was identified based on deviations of the potential temperature at the $Q = 2$

pvu surface from a background mean state, and the analsis revealed that $S^2 \geq S_t^2$ occurs up to 50 % of the time within far northward reaching ridges characterised by above-average dynamic tropopause potential temperatures of about $\Delta\Theta(Q = 2 \text{ pvu}) = 20$ K.

- The subtropical jet stream over the Asian continent exhibits localised occurrence frequency maxima for $S^2 \geq S_t^2$ up to 45 % in the ten year average and during winter, where the jet stream is most pronounced. The interannual variability of the occurrence frequencies for $S^2 \geq S_t^2$ appears to be linked to the zonal location and the strength of the jet core (Wu and Sun, 2017), which needs further investigation.
- The tropical tropopause above the upper tropospheric tropical easterly jet, which emerges from June to September, is exposed to strong vertical wind shear up to 70 % of the time over large areas of the Indian Ocean. These findings, while striking, agree with observation-based research studies on characteristics of the tropical easterly jet (Roja Raman et al., 2009; Sunilkumar et al., 2015).
- The outflow region of the rising branch of the Pacific winter Walker circulation cell exhibits similar occurrence frequencies for strong vertical wind shear $S^2 \geq S_t^2$ at the tropopause above the maritime continent, compared to the tropical easterly jet. This is particularly the case during la Niña phases, in agreement with the stronger outflow on top of the more intense and localised convection above the maritime continent. The interannual variability of the occurrence frequencies for strong vertical wind shear over the maritime continent ranges from 30 % during el Niño (DJF 2009/10) up to 70 % during la Niña (DJF 2010/11).

Overall, the identification of the tropopause shear layer and its geographical mapping presents a step towards a better understanding of the dynamic structure of the transition region between the troposphere and the stratosphere. For the extratropics, the analysis confirmed and expanded the central results from Chapter 4, i.e., that strong vertical wind shear near to the tropopause emerges frequently within ridges of baroclinic waves, and thus, a region that is also associated with the evolution of a pronounced TIL. For the baroclinic wave breaking event with LC2 characteristics in Chapter 4.2.1 it was shown that enhanced static stability and enhanced vertical wind shear generally do not correlate, despite the synoptic scale co-occurrence of the TIL and regions of strong wind shear closely above the LRT. Figure 5.14a shows that the results from the case study are representative for the whole ten years of northern hemispheric ERA5 data. The lower stratosphere between the LRT and 3 km above is mainly characterised by average stratospheric static stability $\overline{N^2}_{strat} = 4 \cdot 10^{-4}$ s^{-2} as well

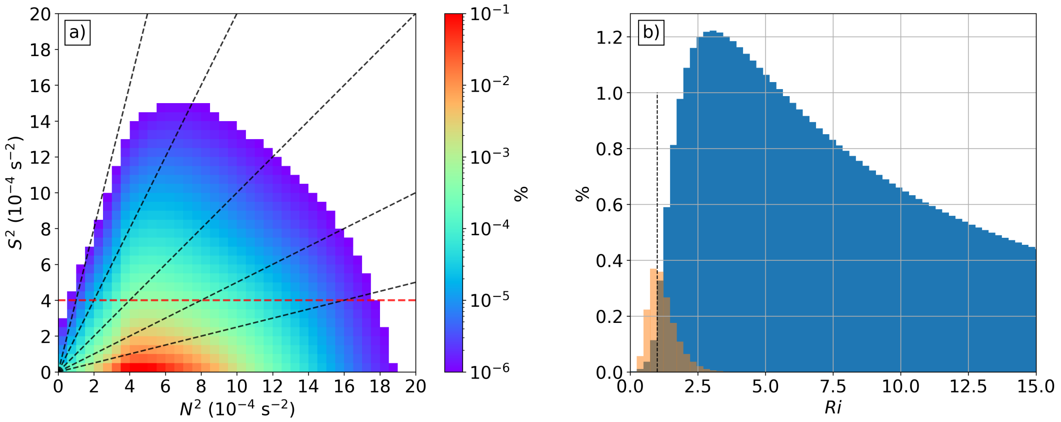

Figure 5.14: a) Relative occurrence frequency distribution of N^2-S^2 pairs in the region between the LRT and 3 km above, for all daily northern hemispheric ERA5 fields from 2008–2017. Logarithmic occurrence frequency color scale. Red dashed line indicates $S^2 = S_t^2$. Dashed black lines indicate the Richardson numbers 0.25, 0.5, 1.0, 2.0 and 4.0. b) Histogram of the relative distribution of Richardson numbers associated with the data displayed in panel a in bins of $\Delta Ri = 0.25$. Orange bars show Ri for grid volumes with $S^2 \geq S_t^2$, and blue bars for the remaining grid volumes between the LRT and 3 km above. Dotted black line indicates $Ri = 1$.

as enhanced values associated with the TIL. At the same time, vertical wind shear below S_t^2 is most prevalent. The resulting Richardson number distribution for grid volumes with $S^2 < S_t^2$ peaks at $Ri = 3$ and spans over a large spectrum of larger values (Fig. 5.14b). Richardson numbers of $Ri < 1$ are rarely associated with $S^2 < S_t^2$ within the first 3 km above the LRT.

Grid volumes with strong vertical wind shear $S^2 \geq S_t^2$ can be found within a large spectrum of N^2 values, under the condition that dynamic stabillity $Ri > Ri_c$ is maintained (leftmost dashed black line in Fig. 5.14a). The Richardson number distribution for grid volumes with $S^2 \geq S_t^2$ peaks at $Ri = 1$ which validates the motivation for the choice of the threshold value $S_t^2 = 4 \cdot 10^{-4}$ s^{-2}. Furthermore, these grid volumes constitute the greater part of Richardson numbers $Ri < 1$. Thus, the analysis shows that the lower stratosphere between the LRT and 3 km above is generally dynamically stable in the absence of strong vertical wind shear, i.e., outside the TSL.

Strong vertical wind shear does not correlate well with the occurrence of turbulence (e.g., Knox, 1997) and the Richardson numbers predicted by the IFS in the ERA5 data set do rarely fall below Ri_c. However, the identification of the TSL narrows down the region where shear induced dynamic instability and turbulence can occur in the stably stratified flow above the LRT. Chapter 3 furthermore showed that the TSL can be exposed to turbulent mixing, which was identified to be caused by small scale processes below the resolution capabilities of the IFS, and which are represented in the model in form of the diffusive turbulence parametrisation that sets in at above-critical Richardson numbers of the order of $\mathcal{O}(1)$. The limited occurrence of the TSL within the first few kilometers above the LRT indicates a link to the chemically defined ExTL or mixing layer. The analysis of airborne measured in situ CO profiles revealed a distinct "kink" in the vertical transition from tropospheric to stratospheric values, which defines the upper edge of the chemical transition layer and indicates a discontiuity in the occurrence of the processes that define the transition. Hoor et al. (2004) determined this upper edge to be located at about 25 K potential temperature above the local dynamic tropopause, i.e., the $Q = 2$ pvu surface, and Pan et al. (2004) identified it at about $2 - 3$ km above the LRT. These results were expanded on global scales by Hegglin et al. (2009), based on CO-O_3 and H_2O-O_3 tracer-tracer correlations derived from Atmospheric Chemistry Experiment Fourier Transform Spectrometer (ACE-FTS) satellite data. The systematic link to the processes that determine the transition was initiated by Berthet et al. (2007), who saw a tropopause following behaviour of the majority of TST trajectories in a trajectory model that was driven by ECMWF data. This Lagrangian approach was extended by Hoor et al. (2010), who linked the chemically defined transition layer to tropopsphere-stratosphere transition timescales of $0 - 50$ days, and thus significantly faster transport compared to the remainder of the LMS. The vertical confinement of the TSL indicates a contribution to the comparatively fast mixing within the first few kilomters above the tropopause. Thus, one of the key results in this Chapter is that shear induced turbulent mixing in the LMS is limited to the first few kilometers above the LRT, which indicates its role as a contributing process to the formation and maintenace of the ExTL on a global scale.

The TSL could be further analysed in the context of the processes that are responsible for its formation. The analysis in Chapter 4 and 5 indicated that strong vertical wind shear at the tropopause is not necessarily linked to exceptional wind speeds in the upper troposphere. Additionally, the thermal wind relation can significantly underestimate the wind shear above the LRT within baroclinic waves, although the shear regions are embedded in the synoptic scale flow that is well represented by the geostrophic wind approximation on isobaric levels. In this context, the strength of the TSL could be an indicator for enhanced gravity wave acitivity and the associated bi-directional interaction between gravity waves and the tropopause respectively the TIL, i.e., the associated maximum of the refractive index (Bense, 2019). Equivalently, the relation between the TSL and gravity waves is bi-directional because the sudden change in wind speed can lead to wave propagation or wave reflection. The TSL could be a major source for gravity waves that emerge from shear instabilities

(Plougonven and Zhang, 2014), depending on how frequently it is exposed to dynamic instability. Non-linear wave-mean-flow interaction caused by the TSL can furthermore influence both the TSL and the TIL through wave energy dissipation and vertical heat and momentum flux at the tropopause (Zhang et al., 2019).

In summary, the identification of the TSL puts previous research studies on the occurrence of strong vertical wind shear at the tropopause into a larger context, and highlights advantages of a threshold based analysis. The analysis reveals that the occurrence of $S^2 \geq S_t^2$ is largely limited to a vertical layer within the first few kilometers above the LRT, which occurs as global scale feature in the UTLS.

6

CONCLUSIONS AND OUTLOOK

6.1 CONCLUSION

This thesis aimed at a better understanding of the evolution of the tropopause inversion layer (TIL) in the context of the ambient atmospheric dynamics, with the goal to assess its function as a conceptual transport barrier for transport and mixing in the region that separates the troposphere from the stratosphere. On one hand, the lower stratospheric maximum in static stability which defines the TIL conceptually inhibits exchange between vertically adjacent air masses. On the other hand, the TIL does not emerge as a standalone flow feature, but rather as one constituent within the underlying large scale dynamics. In this context, several research studies recently suggested a causal relationship between stratosphere-troposphere exchange (STE) and the evolution of the TIL (Kunz et al., 2009; Gettelman and Wang, 2015; Kunkel et al., 2016). The thesis at hand adressed this issue with a particular focus on extratropical baroclinic wave dynamics with the objective to estimate the potential for shear induced turbulence and STE in regions where the TIL evolves. For this, analyses over a large spectrum of spatial and temporal scales were performed, from individual case studies based on in situ airborne measurements in the tropopause region (Chapter 3), to model-based process studies of baroclinic life cycles (Chapter 4), up to climatological and planetary scales based on reanalysis data (Chapter 5). This synergistic approach led to the following key results:

1. Turbulent mixing and STE occurs in regions within baroclinic waves which are characterised by a pronounced temperature inversion above the tropopause, i.e., the TIL.
2. The strong vertical wind shear which causes the turbulence emerges frequently within a synoptic scale through-ridge dipole that largely follows the evolution of the TIL in breaking baroclinic waves.
3. Strong vertical wind shear that holds the potential for dynamic instability in the stratosphere occurs frequently as well as nearly exclusively within a distinct layer of 1–2 km vertical extent above the lapse rate tropopause, and on a global scale.

These findings are based on the results of analyses covering case, process and climatological studies and are provided more comprehensively in the following paragraphs.

The thermal and dynamical structure of the tropopause region at midlatitudes was analysed in the context of the occurrence and shaping of the extratropical transition layer, based on measurements from two research flights. The observational data is taken from the WISE campaign which took place in autumn 2017 over the North Atlantic.

During research flight RF07 the airplane approached the tropopause from the stratosphere above the ridge of a late stage baroclinic wave that was associated with a pronounced surface cyclone. According to forecast fields from the ECMWF IFS, the airplane crossed a layer of strong vertical wind shear that was located closely above the tropopause and reached into the region of enhanced static stability associated with the TIL. Thus, the model predicted Richardson numbers of the order of $\mathcal{O}(1)$. The tracer-tracer correlation of the in situ measured N_2O and CO mixing ratios indicated quasi-isentropic mixing in this region, along with small scale wave perturbations in the trace gas mixing ratios and the measured potential temperature as well as high frequency variability shortly thereafter which was interpreted as in situ measured turbulence. These processes took place on scales below the resolution capability of the IFS. The fact that the layer of strong wind shear was exposed to localised dynamic instabily was further confirmed through the observation of Kelvin Helmholtz billows which emerged on top of the warm conveyor belt cloud deck, shortly after the time where mixing was evident in the trace gas measurements.

During research flight RF12 the research aircraft descended through a region where the IFS forecast predicted a pronounced TIL as well as strong vertical wind shear. This allowed the comparison of the model-derived and the in situ measured dynamic and thermal structure in the tropopause region above the ridge of a baroclinic wave. The analysis showed a largely realistic representation of the TIL in the IFS, but a significant underestimation of the vertical wind shear due to a non-resolved wave signal which was evident in the horizontal wind. The tracer-tracer correlation of N_2O and CO indicated a temporal and/or spatial sequence of mixing processes that took place within the TIL profile.

Both RF07 and RF12 indicate wind shear induced turbulent mixing at the tropopause above upper tropospheric ridges and on the anticyclonic shear side of the tropospheric jet streak. The quasi-vertical state parameter measurements along the selected descent during RF12 indicated a discrepancy between the ability of the IFS to resolve the vertical temperature structure on one hand and the vertical wind shear on the other hand. The vertical and the mesoscale horizontal extent of the shear layer which was predicted by the IFS along the flight path of RF07 was identified to be close to the vertical and effective horizontal resolution capability of the IFS.

The analyses indicate that shear induced turbulent mixing might be a frequently occurring mixing process within ridges of baroclinic waves at above average tropopause altitudes, and thus, a region that has gained comparatively little attention in the context of STE and the associated evolution and maintenance of the extratropical transition layer. This issue is closely linked to the occurrence of a pronounced TIL above ridges, respectively the lack thereof within troughs and low-tropopause features like stratospheric intrusions, where the comparatively small static stability presents a weaker transport barrier, which is associated with frequent and deep mixing of tropospheric and stratospheric air (e.g., Pan et al., 2007; Konopka and Pan, 2012; Schäfler et al., 2021). Furthermore, the comparison of IFS forecast data and in situ measurements indicate that shear induced turbulent mixing above ridges might be underestimated in numerical models, due to resolution restrictions of and the identified discrepancy of the ratio of the static stability N^2 to the vertical wind shear S^2.

In a subsequent analysis the focus is on the apparent link between the evolution of the thermal and the dynamic structure in the tropopause region during baroclinic life cycles in the midlatitudes. The objective was to link the evolution of mean sea level pressure anomalies with the flow in the UTLS, and thus, to track the evolution of the thermal and dynamic structure in the tropopause region. A surface cyclone tracking algorithm was applied to five years of operational ECMWF IFS analysis data over the North Atlantic. First, the metrics were applied to case studies of baroclinic wave breaking events that resemble characteristic LC1 and LC2 life cylces (Thorncroft et al., 1993). Second, the tracking algorithm was used to compile composites of barclinic wave breaking events at comparable evolution stages.

The point in time of maximum surface cyclone intensity, i.e., the global mean sea level pressure minimum along the cyclone track was identified to be associated with common evolution stages in the UTLS during indivdual baroclinic life cycles. The analysis showed that the TIL in real atmospheric flow evolves in good agreement with the forcing mechanisms that have been identified based on theoretical considerations and idealised baroclinic life cyle simulations. The TIL exhibits a distinct trough-ridge dipole structure, in agreement with the anticipated role of the vertical divergence of the ageostrophic vertical wind associated with upper tropospheric PV anomalies of different algebraic sign (Wirth, 2004; Wirth and Szabo, 2007). Furthermore, the TIL exhibits a pronounced mesoscale varibility within the ridges, which has been attributed to enhanced gravity wave activity associated with the upper tropospheric front and the jet exit region (Kunkel et al., 2014), as well localised modification of the thermal structure at the tropopause due to diabatic and mainly cloud-related processes as well as turbulence (Kunkel et al., 2016).

Another key result of Chapter 4 is that the occurrence of strong vertical wind shear in the tropopause region largely matches the synoptic scale evolution of the TIL, i.e., a dipole structure that is characterised by intense wind shear above the tropopause within the ridge, respectively no pronounced wind shear at the tropopause within the trough. The regions of strong wind shear exhibit a mesoscale variability comparable to the TIL, however, a general co-occurrence of enhanced S^2 and enhanced N^2 is not present. Nevertheless, the tropopause region within ridges of baroclinic waves exhibits frequently comparatively low Richardson numbers of the order of $\mathcal{O}(1)$ in the elsewhere dynamically stable lowermost stratosphere. This tendency towards dynamic instability is governed by the vertical wind shear, and thus, the processes responsible for its occurrence. The thermal wind shear approximation was shown to significantly underestimate certain regions of strong vertical wind shear, which agrees with earlier research on the importance of inertial forces (Newton and Persson, 1962) as well as mesoscale flow deformation e.g. caused by large scale gravity waves with intrinsic frequencies close to the inertial limit (Kunkel et al., 2014).

Overall, the results from Chapter 4 broaden our understanding from the case study results in Chapter 3. For WISE RF07 and RF12, the occurrence of strong vertical wind shear above the tropopause was identified as a prerequisite respectively an indicator for the potential for dynamic instability and shear induced turbulent mixing above the tropopause. The composite analysis showed that these conditions are frequently met over large areas of the tropopause region within ridges of baroclinic waves over the North Atlantic, including particularly far poleward reaching ridges at the time of maximum surface cylone intensity. As a consequence, the small scale mixing process identified on base of the case studies (Chapter 3) most potentially contributes significantly to STE in the extratropics. This is also confirmed by recent findings by Spreitzer et al. (2019). This process might have been previously underestimated due to the fact that numerical models are just recently beginning to resolve the vertical and mesoscale horizontal scales at which the dynamic stability in the tropopause region is defined. The reason for the significance of frequently occurring small scale mixing within baroclinic waves is the fact that they are the predominant flow feature in the UTLS in the midlatitudes, with 4–8 individual waves being present in each hemisphere all the time.

Ultimately, the mixing described in Chapter 3 and 4 is the consequence of vertical shear of the horizontal wind. Although it is known that strong wind shear occurs in the tropopause region, no climatological analysis was present of the shear occurrence. This gap is now closed by an analysis of daily ERA5 data over the course of ten years for the northern hemisphere. Applying a threshold criterion with $S_t^2 = 4 \cdot 10^{-4}\ \mathrm{s}^{-2}$ showed that regions of strong vertical wind shear

$S^2 \geq S_t^2$ are most dominantly present in a layer above the local tropopause. In fact, such enhanced shear has an occurrence frequency on the order of $1-10$ % within the first two kilometers above the local tropopause. Moreover, since these enhanced shear values occur everywhere above the tropopause from the tropics to high latitudes, this feature can be regarded as a global scale phenomenon and can thus be termed the tropopause wind shear layer (TSL).

Although present from the equator to the high latitudes, the strong vertical wind shear has geographically dependant different sources. In the midlatitudes, $S^2 \geq S_t^2$ emerges mainly in the storm track regions over the North Atlantic and the Northeast Pacific, at above-average tropopause altitudes within ridges of baroclinic waves. This further expands the key findings from Chapter 4, and generalises them for all seasons in the long year average and the whole northern hemisphere. Similarly to the chemically defined extratropical transition layer, the occurrence of the TSL is limited to the first few kilometers above the local tropopause. This tropopause-following behaviour of both features strongly suggests a link to the separation of the extratropical transition layer from the remainder of the LMS (Hoor et al., 2004; Pan et al., 2004; Hegglin et al., 2009) which has been linked to a discontinuity in the transport time scales (Berthet et al., 2007; Hoor et al., 2010), and thus, the processes that transport and disperse tropospheric air in the stratosphere. Ultimately, such a link would also involve a controlling function of the TSL concerning the radiative budget not only locally but also at the earths surface, because small relative changes in the temperature structure and the gradients of radiatively active trace gases in the UTLS can significantly influence the radiative forcing (Riese et al., 2012).

At lower latitudes, the STJ over the Asian continent is associated with comparatively frequently occuring strong vertical wind shear at the tropopause, particularly during winter. The occurrence of strong vertical wind shear at the southern side of the tropopause break particularly during winter could contribute to stratosphere-troposphere exchange at the upper edge of the lowermost stratosphere. Up to now, the upper edge of the lowermost stratosphere has been identified to be "ventilated" with tropospheric air primarily during the summer months, where the latitudinal transport barrier at the tropopause break is comparatively weak (Berthet et al., 2007).

The tropical upper tropospheric easterlies over the Indian ocean and the Maritime continent are associated with the exeptionally frequent occurrence of strong wind shear $S^2 \geq S_t^2$ at the the tropical tropopause, with area-wide peak values of up to 70 %. The summer maximum over the Indian ocean is associated with the tropical easterly jet, and the representation of the tropopause wind shear layer in the ERA5 reanalysis agrees with observation-based research studies on intense vertical wind shear associated with the tropical easterly jet (Roja

Raman et al., 2009; Sunilkumar et al., 2015). The winter maximum over the maritime continent emerges mainly during pronounced la Niña phases, which is linked to the relation between the strength and location of the convective rising branch of the Pacific Walker circulation cell (Sullivan et al., 2019) and the sea surface temperature anomaly. Both the tropical easterly jet and the upper tropospheric winter easterlies above the maritime continent feature a systematically occurring perturbation in the tropopause structure, which is linked to the occurrence of strong vertical wind shear above and below the local lapse rate tropopause. This needs further investigation in the context of STE within the tropical tropopause layer (Fueglistaler et al., 2004; Fueglistaler et al., 2009), and closely linked, the processes that force the exceptionally pronoucend and frequent wind shear in this region (Flannaghan and Fueglistaler, 2014). Gravity waves excited from tropical convection (Müller et al., 2018) could contribute to the formation of the tropopause shear layer (Podglajen et al., 2017), and its occurrence in this region vice versa likely influences the spectrum of vertically propagating gravity waves (Lane, 2021).

In summary, the results of this thesis advance our understanding of the relation between the dynamic and thermal structure in the UTLS substantially, particularly in the extratropical UTLS. The occurrence of the TIL in the extratropics is put into context of the underlying synoptic- and mesoscale flow, and thus, the TIL is identified as an inherent feature of a region that frequently comprises the potential for dynamic shear instability and turbulent mixing.

6.2 OUTLOOK

On the basis of the results from this thesis further research can advance in the following directions, to adress questions that remain open or have come up in this thesis.

First, the relative contribution of processes that result in the formation and the observed variability of the TSL on different scales needs further investigation. In the midlatitudes this could be approached in form of baroclinic life cycle simulations at varying steps of idealisation. Such sensitivity studies could then link balanced flow dynamics and the influence of resolved gravity waves to the formation of the TSL, as well as non-resolved physical processes and the respective model paramtrisation schemes, equivalent to the research on the formation of the TIL (Wirth and Szabo, 2007; Erler and Wirth, 2011; Kunkel et al., 2014; Kunkel et al., 2016).

Second, the potential for dynamic instability and turbulent mixing within the regions of strong vertical wind shear should be be further narrowd down.

Jaeger and Sprenger (2007) compiled a climatology on clear air turbulence indicators in the northern hemispheric tropopause region based on the ERA40 reanalysis. The climatological distribution of the turbulence index TI (Ellrod and Knapp, 1992) as a more sophisticated indicator for turbulence shows a good general agreement with the climatology of the TSL in some regions, e.g. the storm track regions, as well as more pronounced differences in other regions, e.g. the enhanced potential for turbulence over central Europe and the American Northwest as well as particularly on the northern side of the subtropical jet stream. Deviations could stem from process-related differences due to the inclusion of the horizontal flow deformation in the TI as a source for wind shear generation, or they could be attributed to advancements in the resolution capabilities and the representation of physical processes in the more advanced ERA5 reanalysis.

These first two points for further research are closely linked because the wind shear on one hand governs the potential for shear induced turbulent mixing in the stably stratified lower stratosphere and on the other hand and the occurrence of turbulence significantly influences the thermal and dynamic structure through vertical diffusion of momentum and heat.

The validation of the characteristics of the TSL that were identified in the ERA5 reanalysis is another important point to consider, i.e., its instantaneous vertical extent and the vertical spread in the tropopause region, as well as its variability on different temporal and spatial scales and the resulting geographically mapped occurrence frequencies. This could be approached on the basis of a systematic comparison of observational data with the model-derived characterstics within the metrics that were defined in this thesis. For example, such an analysis could be based on radiosonde measurements, or the doppler lidar wind measurement data from the ESA Aeolus satellite which was recently put into orbit. The Aeolus satellite probes the lowermost 30 km of the atmosphere in a vertical resolution comparable to the one of the IFS in the tropopause region (multiples of 250 m, typically in the range of $0.25 - 2$ km, (Reitebuch et al., 2014)), and thus, presents a potent opportunity for a further investigation of the TSL.

A last point which should be mentioned here is the link between the TSL and the extratropical transition layer. The question is whether the TSL is a major cause of the existence of the chemical transition region in the extratropics. Such an analysis could be based on the approach briefly outlined in Chapter 5.3.1 in the combination of high resolution observations with reanalysis data. However, such an investigation should be based not soley on case studies from research aircraft campaigns but should also include a larger data set, e.g., from IAGOS. This has the adavantage to focus on both a process oriented view as well as on a quasi-climatological perspective due to the long available time series of the IAGOS data set.

A

SUPPLEMENTARY INFORMATION FOR CHAPTER 3

A.1 GEOMETRIC ESTIMATION OF THE KELVIN HELMHOLTZ BILLOW DIMENSION

The estimation of the height of the Kelvin Helmholtz billows photographed on the cloud deck is based on the idea that the shift of the billows in the image plane is caused the displacement due to the airplane traveling for $\Delta t = (4 \pm 1)$ s with the true air speed $TAS = (235 \pm 5)$ m/s. The images are shifted relative to each other such that the Kelvin Helmholtz billows overlap, and the relative shift is used to calculate the dimension of the image plane at the location of the wave.

The viewing angle of the camera was estimated to $\phi = 90° + (20 \pm 3)°$ from the airplane heading, based on the location of the airplane windows and the alignment of the airplane wing in the photos. This implicates that the distance covered by the airplane $TAS \cdot \Delta t$ results in a horizontal displacement of the billows in the image plane, as well as a departure of the image plane from the airplane orthogonal to the flight direction. The latter results in an increase of the image plane size relative to the Kelvin Helmholtz billows which are assumed to remain constant in size during Δt. The total shift of the billows depends on their horizontal location in the image plane, as well as on the viewing angle of the camera. The following considerations are made to illustrate the concept of the calculation:

For a backward facing camera, a point in the centre of the image would receive no shift, and a point towards the corners would receive a shift based on the increase of the size of the image plane. For a sidewards facing camera (orthogonal to the flight direction), any point in the image plane would receive a shift of $TAS \cdot \Delta t$, and the size of the image plane would stay constant. For the viewing angle estimated for the photos taken during WISE RF07, the following considerations are made to narrow down the range of sizes for the Kelvin-Helmholtz billows:

The increase in distance of the image plane from the airplane orthogonal to the flight direction $\Delta y = TAS \cdot \Delta t \cdot sin(\phi)$ amounts to (321 ± 93) m. A point at the right edge in the second photo is located $\Delta x = (697 \pm 46)$ m from the right edge in the first photo, according to the geometric deliberations in Fig. 3.9 and utilising the law of sines. Equivalently, a point that is initially (in the first photo) located at the left edge of the image plane, is shifted $\Delta x = (1070 \pm 21)$

m from the left edge in the second photo. This value is larger than $TAS \cdot \Delta t$ due to the additional effect of the increase of the size of the image plane. These two values for Δx narrow down the range for the absolute shift in kilometers between the two photos.

In a first calculation, the shift of the two photos relative to each other is done such that the pronounced billows on the right hand side overlap, and is estimated to $f = 5 \pm 1$ %. Assuming the lower (right hand side) limit $\Delta x = 697$ m as 5 % of the images width, results in a horizontal dimension of (13.93 ± 4.55) km of the image plane of the first photo at the location of the Kelvin Helmholtz billows.

The relative horizontal extent of the whole wave package is smaller in the second photo, which agrees with the assumed increase in size of the image plane, and validates the considerations in the previous paragraphs. The wave crests on the left hand side of the image therefore do not overlap precisely when shifting the images based on the crests on the right hand side. Repeating the calculation with an $f = 6$ % shift based on the wave crests on the left side and the upper limit for Δx of 1070 m results in a horizontal dimension of (17.83 ± 5.37) km of the image plane of the second photo at the location of the Kelvin Helmholtz billows. According to the central values this is an increase of 3.89 km of the horizontal image plane extent between the first and the second photo.

According to the estimated increase in distance of the image orthogonal to the flight direction of $\Delta y = 367$ m, the horizontal dimension of the image plane of the second photo should increase by (373 ± 108) m compared to the first photo, which is a factor 10 smaller than the previous result. The two calculations however receive more comparable results when taking into consideration that the two shifts of the images are mainly based on one crest about 2/8 of the image size from the right edge for the first photo, respectively a crest about 1/8 from the left edge for the second photo. The assumed angle between the image plane and the wave train as well as its uncertainty further reduce the precision of the calculation.

The estimation of the extreme values for the size of the image planes including the error estimation results in a large margin of possible values, from (13.93 ± 4.55) km for the first photo to (17.83 ± 5.37) km for the second photo. The relative shift of the two images however is not done based on wave crests at the edges of the photos. A best guess value is chosen based on the fact that the image shift is most reliable based on the wave crests about 2/8 of the horizontal image size from the right edge, which results in approximately (15 ± 5) km horizontal extent of the image plane at the location of the Kelvin Helmholtz billows.

The central wave train consisting of five wavelength spans over approximately 42 % of the horizontal image, which implicates a wavelength $\lambda = (1260 \pm 420)$

m. Assuming a crest height of about $\lambda/2$ results in a vertical extent of the wave (630 ± 210) m.

Overall, the assumptions and calculations made in the previous paragraphs deliver results that are consistent in themselves, but also agree with the information from the in-situ measurements, the IFS model data, and the information within the photos.

BIBLIOGRAPHY

Assonov, S. S., C. A. Brenninkmeijer, T. Schuck, and T. Umezawa (2013). “N2O as a tracer of mixing stratospheric and tropospheric air based on CARIBIC data with applications for CO2.” *Atmospheric Environment* 79, pp. 769–779. DOI: 10.1016/j.atmosenv.2013.07.035.

Banerjee, A., G. Chiodo, M. Previdi, M. Ponater, A. J. Conley, and L. M. Polvani (2019). “Stratospheric water vapor: an important climate feedback.” *Climate Dynamics* 53.3-4, pp. 1697–1710. DOI: 10.1007/s00382-019-04721-4.

Beljaars, A. C., A. R. Brown, and N. Wood (2004). “A new parametrization of turbulent orographic form drag.” *Quarterly Journal of the Royal Meteorological Society* 130.599 PART B, pp. 1327–1347. DOI: 10.1256/qj.03.73.

Bengtsson, L., K. I. Hodges, M. Esch, N. Keenlyside, L. Kornblueh, J. J. Luo, and T. Yamagata (2007). “How may tropical cyclones change in a warmer climate?” *Tellus, Series A: Dynamic Meteorology and Oceanography* 59 A.4, pp. 539–561. DOI: 10.1111/j.1600-0870.2007.00251.x.

Bense, V. (2019). “Modifikation von Schwerewellen bei Propagation durch die Tropopause – Idealisierte Modellstudien.” Dissertation. Johannes Gutenberg-University Mainz. DOI: http://doi.org/10.25358/openscience-2356.

Berthet, G., J. G. Esler, and P. H. Haynes (2007). “A Lagrangian perspective of the tropopause and the ventilation of the lowermost stratosphere.” *Journal of Geophysical Research Atmospheres* 112.18, pp. 1–14. DOI: 10.1029/2006JD008295.

Birner, T. and H. Bönisch (2011). “Residual circulation trajectories and transit times into the extratropical lowermost stratosphere.” *Atmospheric Chemistry and Physics* 11.2, pp. 817–827. DOI: 10.5194/acp-11-817-2011.

Birner, T. (2006). “Fine-scale structure of the extratropical tropopause region.” *Journal of Geophysical Research Atmospheres* 111.4, pp. 1–14. DOI: 10.1029/2005JD006301.

Birner, T. (2010). “Residual Circulation and Tropopause Structure.” *Journal of Atmospheric Sciences* 67, pp. 2582–2600. DOI: 10.1175/2010JAS3287.1.

Birner, T., A. Dörnbrack, and U. Schumann (2002). “How sharp is the tropopause at midlatitudes?” *Geophysical Research Letters* 29.14, pp. 45–1–45–4. DOI: 10.1029/2002GL015142.

Bühler, O. and M. E. McIntyre (2005). “Wave capture and wave-vortex duality.” *Journal of Fluid Mechanics* 534, pp. 67–95. DOI: 10.1017/S0022112005004374.

Catto, J. L., L. C. Shaffrey, and K. I. Hodges (2010). “Can climate models capture the structure of extratropical cyclones?” *Journal of Climate* 23.7, pp. 1621–1635. DOI: 10.1175/2009JCLI3318.1.

Cressman, G. P. (1959). “An Operational Objective Analysis System.” *Monthly Weather Review* 87.10, pp. 367–374. DOI: 10.1175/1520-0493(1959)087<0367:AOOAS>2.0.CO;2.

Danielsen, E. F. (1968). “Stratospheric-Tropospheric Exchange Based on Radioctivity, Ozone and Potential Vorticity.” *Journal of the Atmospheric Sciences* 25.3, pp. 502–518. DOI: https://doi.org/10.1175/1520-0469(1968)025<0502:STEBOR>2.0.CO;2.

Davis, C. A. and K. A. Emanuel (1991). “Potential Vorticity Diagnostics of Cyclogenesis.” *Monthly Weather Review* 119, p. 55. DOI: https://doi.org/10.1175/1520-0493(1991)119<1929:PVDOC>2.0.CO;2.

Dee, D. P. et al. (2011). “The ERA-Interim reanalysis: Configuration and performance of the data assimilation system.” *Quarterly Journal of the Royal Meteorological Society* 137.656, pp. 553–597. DOI: 10.1002/qj.828.

Dörnbrack, A., T. Gerz, and U. Schumann (1995). “Turbulent Breaking of Overturning Gravity Waves below a Critical Level.” *Applied Scientific Research* 54, pp. 163–176. DOI: https://doi.org/10.1007/BF00849114.

Duck, T. J. and J. A. Whiteway (2005). “The spectrum of waves and turbulence at the tropopause.” *Geophysical Research Letters* 32.7, pp. 1–4. DOI: 10.1029/2004GL021189.

Dvoskin, N. and N. Sissenwine (1958). “Evaluation of AN/GMD-2 Wind Shear Data for Development of Missile Design Criteria.” *Air Force Surveys in Geophysics* 99, 72 pp.

ECMWF (2016a). “IFS documentation – Cy41r2 Operational implementation 8 March 2016 Part III : Dynamics and numerical procedures.” *IFS Documentation CY41R2*. ECMWF. DOI: 10.21957/83wouv80.

ECMWF (2016b). “IFS documentation – Cy41r2 Operational implementation 8 March 2016 Part IV: Physical Processes.” *IFS Documentation CY41R2*. ECMWF. DOI: 10.21957/tr5rv27xu.

ECMWF (2016c). “IFS documentation – Cy41r2 Operational implementation 8 March 2016 Part VI : Technical and computational procedures.” *IFS Documentation CY41R2*. ECMWF. DOI: 10.21957/5rwd87qew.

Ellrod, G. P. and D. I. Knapp (1992). “An Objective Clear-Air Turbulence Forecasting Technique: Verification and Operational Use.” *Weather and Forecasting* 7, p. 15. DOI: https://doi.org/10.1175/1520-0434(1992)007<0150:AOCATF>2.0.CO;2.

Endlich, R. M. and G. S. McLean (1965). “Jet-Stream Structure over the Central United States Determined from Aircraft Observations.” *Journal of Applied Meteorology* 4.1, pp. 83–90. DOI: 10.1175/1520-0450(1965)004<0083:jssotc>2.0.co;2.

Erler, A. R. and V. Wirth (2011). “The Static Stability of the Tropopause Region in Adiabatic Baroclinic Life Cycle Experiments.” *Journal of the Atmospheric Sciences* 68.6, pp. 1178–1193. DOI: 10.1175/2010JAS3694.1.

Ertel, H. (1942). “Ein neuer hydrodynamischer Erhaltungssatz.” *Die Naturwissenschaften* 30.36, pp. 543–544. DOI: 10.1007/BF01475602.

Fischer, H., F. G. Wienhold, P. Hoor, O. Bujok, C. Schiller, P. Siegmund, M. Ambaum, H. A. Scheeren, and J. Lelieveld (2000). “Tracer correlations in the northern high latitude lowermost stratosphere: Influence of cross-tropopause mass exchange.” *Geophysical Research Letters* 27.1, pp. 97–100. DOI: 10.1029/1999GL010879.

Flannaghan, T. J. and S. Fueglistaler (2014). “Vertical mixing and the temperature and wind structure of the tropical tropopause layer.” *Journal of the Atmospheric Sciences* 71.5, pp. 1609–1622. DOI: 10.1175/JAS-D-13-0321.1.

Flocke, F, R. Herman, R. Salawitch, E. Atlas, C. Webster, S. Schauffier, and R. Lueb (1999). “An examination of chemistry and transport processes in the tropical lower stratosphere using observations of long-lived and short-lived compounds obtained during STRAT and POLARIS.” 104.D21, pp. 26625–26642. DOI: https://doi.org/10.1029/1999JD900504.

Forbes, R. M. and A. M. Tompkins (2011). “An improved representation of cloud and precipitation.” *ECMWF Newsletter* 129.129, pp. 13–18. DOI: 10.21957/nfgulzhe.

Forbes, R. M. and M. Ahlgrimm (2014). “On the representation of high-latitude boundary layer mixed-phase cloud in the ECMWF global model.” *Monthly Weather Review* 142.9, pp. 3425–3445. DOI: 10.1175/MWR-D-13-00325.1.

Forster, P and K. P. Shine (1997). “Radiative forcing and temperature trends from stratospheric ozone changes.” *Journal of Geophysical Research* 102.D9, pp. 10841–10855. DOI: https://doi.org/10.1029/96JD03510.

Fritts, D. C. and T. L. Palmer (1996). “Evolution and Breakdown of Kelvin-Helmholtz Billows in Stratified Compresiible Flows. Part I: Comparison of Two- and Three-dimensional Flows.” *Journal of Atmospheric Sciences* 53.22, pp. 3173–3191. DOI: https://doi.org/10.1175/1520-0469(1996)053<3173:EABOKB>2.0.CO;2.

Fritts, D. C., L. Wang, G. Baumgarten, A. D. Miller, M. A. Geller, G. Jones, M. Limon, D. Chapman, J. Didier, C. B. Kjellstrand, D. Araujo, S. Hillbrand, A. Korotkov, G. Tucker, and J. Vinokurov (2017). “High-resolution observations and modeling of turbulence sources, structures, and intensities in the upper mesosphere.” *Journal of Atmospheric and Solar-Terrestrial Physics* 162.October 2016, pp. 57–78. DOI: 10.1016/j.jastp.2016.11.006.

Fritts, D. C., L. Wang, M. A. Geller, D. A. Lawrence, J. Werne, and B. B. Balsley (2016). “Numerical modeling of multiscale dynamics at a high reynolds number: Instabilities, turbulence, and an assessment of ozmidov and thorpe scales.” *Journal of the Atmospheric Sciences* 73.2, pp. 555–578. DOI: 10.1175/JAS-D-14-0343.1.

Fritts, D. C., L. Wang, and J. A. Werne (2013). “Gravity wave-fine structure interactions. Part I: Influences of fine structure form and orientation on flow evolution and instability.” *Journal of the Atmospheric Sciences* 70.12, pp. 3710–3734. DOI: 10.1175/JAS-D-13-055.1.

Fueglistaler, S, A. E. Dessler, T. J. Dunkerton, I Folkins, Q Fu, and P. W. Mote (2009). “Tropical Tropopause Layer.” *Reviews of Geophysics* 47.1, pp. 1–31. DOI: doi:10.1029/2008RG000267.

Fueglistaler, S., H. Wernli, and T. Peter (2004). “Tropical troposphere-to-stratosphere transport inferred from trajectory calculations.” *Journal of Geophysical Research: Atmospheres* 109.3, pp. 1–16. DOI: 10.1029/2003jd004069.

Geerts, B. and Q. Miao (2010). “Vertically pointing airborne Doppler radar observations of Kelvin-Helmholtz billows.” *Monthly Weather Review* 138.3, pp. 982–986. DOI: 10.1175/2009MWR3212.1.

Gettelman, A., L. L. Pan, W. J. Randel, P. Hoor, T. Birner, and M. I. Hegglin (2011). “The Extratropical Upper Troposphere and Lower Stratosphere.” *Reviews of Geophysics* 49.3, pp. 1–31. DOI: https://doi.org/10.1029/2011RG000355.

Gettelman, A. and T. Wang (2015). “Structural diagnostics of the tropopause inversion layer and its evolution.” *Journal of Geophysical Research Atmospheres* 120.1, pp. 46–62. DOI: 10.1002/2014JD021846.

Gray, S. L. (2006). “Mechanisms of midlatitude cross-tropopause transport using a potential vorticity budget approach.” *Journal of Geophysical Research Atmospheres* 111.17, pp. 1–14. DOI: 10.1029/2005JD006259.

Hanley, J. and R. Caballero (2012). “Objective identification and tracking of multicentre cyclones in the ERA-Interim reanalysis dataset.” *Quarterly Journal of the Royal Meteorological Society* 138.664, pp. 612–625. DOI: 10.1002/qj.948.

Hegglin, M. I., C. D. Boone, G. L. Manney, and K. A. Walker (2009). “A global view of the extratropical tropopause transition layer from Atmospheric Chemistry Experiment Fourier Transform Spectrometer O3, H2O, and CO.” *Journal of Geophysical Research Atmospheres* 114.7, pp. 1–18. DOI: 10.1029/2008JD009984.

Hegglin, M. I. et al. (2010). “Multimodel assessment of the upper troposphere and lower stratosphere: Extratropics.” *Journal of Geophysical Research Atmospheres* 115.20, pp. 1–24. DOI: 10.1029/2010JD013884.

Hersbach, H. et al. (2020). “The ERA5 global reanalysis.” *Quarterly Journal of the Royal Meteorological Society* March, pp. 1–51. DOI: 10.1002/qj.3803.

Hoinka, K. P. (1997). “The tropopause: Discovery, definition and demarcation.” *Meteorologische Zeitschrift* 6.6, pp. 281–303. DOI: 10.1127/metz/6/1997/281.

Holton, J. R. (1995). “Stratosphere–Troposphere Exchange.” *Stratosphere Troposphere Interactions* 95, pp. 331–355. DOI: 10.1007/978-1-4020-8217-7_8.

Holton, J. R. and G. J. Hakim (2004). *An introduction to dynamic meteorology.* Ed. by R Dmowska, J. R. Holton, and T. H. Rossby. 4th edition. Vol. 88. Elsevier, pp. 1–532. DOI: 10.1016/C2009-0-63394-8.

Homeyer, C. R., L. L. Pan, S. W. Dorsi, L. M. Avallone, A. J. Weinheimer, A. S. O’Brien, J. P. Digangi, M. A. Zondlo, T. B. Ryerson, G. S. Diskin, and T. L. Campos (2014). “Convective transport of water vapor into the lower stratosphere observed during double-tropopause events.” *Journal of Geophysical Research* 119.18, pp. 10,941–10,958. DOI: 10.1002/2014JD021485.

Hoor, P., C. Gurk, D. Brunner, M. I. Hegglin, H. Wernli, and H. Fischer (2004). “Seasonality and extent of extratropical TST derived from in-situ CO measurements during SPURT.” *Atmospheric Chemistry and Physics Discussions* 4.2, pp. 1691–1726. DOI: https://doi.org/10.5194/acp-4-1427-2004.

Hoor, P., H. Wernli, M. I. Hegglin, and H. Bönisch (2010). “Transport timescales and tracer properties in the extratropical UTLS.” *Atmospheric Chemistry and Physics* 10.16, pp. 7929–7944. DOI: 10.5194/acp-10-7929-2010.

Hoor, P., H. Fischer, L. Lange, J. Lelieveld, and D. Brunner (2002). “Seasonal variations of a mixing layer in the lowermost stratosphere as identified by the CO-O3 correlation from in situ measurements.” *Journal of Geophysical Research: Atmospheres* 107.D5, ACL 1–1–ACL 1–11. DOI: 10.1029/2000JD000289.

Hoskins, B. J., M. E. McIntyre, and A. W. Robertson (1985). “On the use and significance of isentropic potential vorticity maps.” *The Quarterly Journal of the Royal Meteorological Society* 111.466, pp. 877–946. DOI: https://doi.org/10.1002/qj.49711147002.

Hoskins, B. J. (1991). “Towards a PV-θ view of the general circulation.” *Tellus A* 43.4, pp. 27–35. DOI: 10.1034/j.1600-0870.1991.t01-3-00005.x.

Iacono, M. J., J. S. Delamere, E. J. Mlawer, M. W. Shephard, S. A. Clough, and W. D. Collins (2008). “Radiative forcing by long-lived greenhouse gases: Calculations with the AER radiative transfer models.” *Journal of Geophysical Research Atmospheres* 113.13, pp. 2–9. DOI: 10.1029/2008JD009944.

Jaeger, E. B. and M Sprenger (2007). “A Northern Hemispheric climatology of indices for clear air turbulence in the tropopause region derived from ERA40 reanalysis data.” *Journal of Geophysical Research Atmospheres* 112.20, pp. 1–13. DOI: 10.1029/2006JD008189.

Kaluza, T., D. Kunkel, and P. Hoor (2019). “Composite analysis of the tropopause inversion layer in extratropical baroclinic waves.” *Atmospheric Chemistry and Physics* 19.10, pp. 1–22. DOI: https://doi.org/10.5194/acp-19-6621-2019.

Kaluza, T., D. Kunkel, and P. Hoor (2021). “On the occurrence of enhanced vertical wind shear in the tropopause region : A ten year ERA5 northern hemispheric study.” *Weather and Climate Dynamics*, pp. 1–30. DOI: https://doi.org/10.5194/wcd-2021-8.

Knox, J. A. (1997). “Possible mechanisms of clear-air turbulence in strongly anticyclonic flows.” *Monthly Weather Review* 125.6, pp. 1251–1259. DOI: 10.1175/1520-0493(1997)125<1251:PMOCAT>2.0.CO;2.

Koch, P., H. Wernli, and H. C. Davies (2006). “An event-based jet-stream climatology and typology.” *International Journal of Climatology* 26.3, pp. 283–301. DOI: 10.1002/joc.1255.

Köhler, M., M. Ahlgrimm, and A. Beljaars (2011). “Unified treatment of dry convective and stratocumulus-topped boundary layers in the ECMWF model.” *Quarterly Journal of the Royal Meteorological Society* 137.654, pp. 43–57. DOI: 10.1002/qj.713.

Konopka, P. and L. L. Pan (2012). “On the mixing-driven formation of the Extratropical Transition Layer (ExTL).” *Journal of Geophysical Research Atmospheres* 117.17, pp. 1–9. DOI: 10.1029/2012JD017876.

Krishnamurti, T. N. and H. Bhalme (1976). “Ocillations of a Monsoon System. Part I. Observational Aspects.” *Journal of Atmospheric Sciences* 33.10, pp. 1937–1954. DOI: https://doi.org/10.1175/1520-0469(1976)033<1937:OOAMSP>2.0.CO;2.

Kunkel, D., P. Hoor, and V. Wirth (2016). “The tropopause inversion layer in baroclinic life-cycle experiments: The role of diabatic processes.” *Atmospheric Chemistry and Physics* 16.2, pp. 541–560. DOI: 10.5194/acp-16-541-2016.

Kunkel, D., P. Hoor, T. Kaluza, J. Ungermann, B. Kluschat, A. Giez, H. C. Lachnitt, M. Kaufmann, and M. Riese (2019). “Evidence of small-scale quasi-isentropic mixing in ridges of extratropical baroclinic waves.” *Atmospheric Chemistry and Physics* 19.19, pp. 12607–12630. DOI: 10.5194/acp-19-12607-2019.

Kunkel, D., P. Hoor, and V. Wirth (2014). “Can inertia-gravity waves persistently alter the tropopause inversion layer?” *Geophysical Research Letters* 41.22, pp. 7822–7829. DOI: 10.1002/2014GL061970.

Kunz, A., P. Konopka, R. Müller, and L. L. Pan (2011). “Dynamical tropopause based on isentropic potential vorticity gradients.” *Journal of Geophysical Research Atmospheres* 116.1, pp. 1–13. DOI: 10.1029/2010JD014343.

Kunz, A., P. Konopka, R. Müller, L. L. Pan, C. Schiller, and F. Rohrer (2009). “High static stability in the mixing layer above the extratropical tropopause.” *Journal of Geophysical Research Atmospheres* 114.16, pp. 1–9. DOI: 10.1029/2009JD011840.

Lane, T. P. (2021). “Does Lower-Stratospheric Shear Influence the Mesoscale Organization of Convection ?” *Geophysical Research Letters* 48.3, pp. 1–10. DOI: 10.1029/2020GL091025.

Liu, H. L. (2017). “Large Wind Shears and Their Implications for Diffusion in Regions With Enhanced Static Stability: The Mesopause and the Tropopause.” *Journal of Geophysical Research: Atmospheres* 122.18, pp. 9579–9590. DOI: 10.1002/2017JD026748.

Lott, F. and M. J. Miller (1997). “A new subgrid-scale orographic drag parametrization: Its formulation and testing.” *Quarterly Journal of the Royal Meteorological Society* 123.537, pp. 101–127. DOI: https://doi.org/10.1002/qj.49712353704.

Louis, J. F., M. Tiedtke, and J. F. Geleyn (1982). “A Short History of the Operational PBL Parameterization at ECMWF.” *ECMWF Workshop on Boundary Layer Parametrization.* ECMWF, p. 21.

Madonna, E., H. Wernli, H. Joos, and O. Martius (2014). “Warm conveyor belts in the ERA-Interim Dataset (1979-2010). Part I: Climatology and potential vorticity evolution.” *Journal of Climate* 27.1, pp. 3–26. DOI: 10.1175/JCLI-D-12-00720.1.

Miles, J. W. (1961). “On the stability of heterogeneous shear flows.” *Journal of Fluid Mechanics* 10.4, pp. 496–508. DOI: 10.1017/S0022112061000305.

Mlawer, E. J., S. J. Taubman, P. D. Brown, M. J. Iacono, and S. A. Clough (1997). “Radiative transfer for inhomogeneous atmospheres: RRTM, a validated correlated-k model for the longwave.” *Journal of Geophysical Research Atmospheres* 102.14, pp. 16663–16682. DOI: 10.1029/97jd00237.

Morcrette, J. J., H. W. Barker, J. N. Cole, M. J. Iacono, and R. Pincus (2008). “Impact of a new radiation package, McRad, in the ECMWF integrated forecasting system.” *Monthly Weather Review* 136.12, pp. 4773–4798. DOI: 10.1175/2008MWR2363.1.

Müller, S., P. Hoor, F. Berkes, H. Bozem, M. Klingebiel, P. Reutter, H. G. Smit, M. Wendisch, P. Spichtinger, and S. Borrmann (2015). “In situ detection of stratosphere-troposphere exchange of cirrus particles in the midlatitudes.” *Geophysical Research Letters* 42.3, pp. 949–955. DOI: 10.1002/2014GL062556.

Müller, S. K., E. Manzini, M. Giorgetta, K. Sato, and T. Nasuno (2018). “Convectively Generated Gravity Waves in High Resolution Models of Tropical Dynamics.” *Journal of Advances in Modeling Earth Systems* 10.10, pp. 2564–2588. DOI: 10.1029/2018MS001390.

Neu, U. et al. (2013). “Imilast: A community effort to intercompare extratropical cyclone detection and tracking algorithms.” *Bulletin of the American Meteorological Society* 94.4, pp. 529–547. DOI: 10.1175/BAMS-D-11-00154.1.

Newton, C. W. and A. V. Persson (1962). “Structural characteristics of the subtropical jet stream and certain lower-stratospheric wind systems.” *Tellus* 14.2, p. 2. DOI: 10.3402/tellusa.v14i2.9542.

Nowack, P. J., N. L. Abraham, P. Braesicke, and J. A. Pyle (2018). “The Impact of Stratospheric Ozone Feedbacks on Climate Sensitivity Estimates.” *Journal of Geophysical Research: Atmospheres* 123.9, pp. 4630–4641. DOI: 10.1002/2017JD027943.

O’Sullivan, D. and T. J. Dunkerton (1995). “Generation of Inertia–Gravity Waves in a Simulated Life Cycle of Baroclinic Instability.” *Journal of the Atmospheric Sciences* 52.21, pp. 3695–3716. DOI: https://doi.org/10.1175/1520-0469(1995)052<3695:GOIWIA>2.0.CO;2.

Orr, A., P. Bechtold, J. Scinocca, M. Ern, and M. Janiskova (2010). “Improved middle atmosphere climate and forecasts in the ECMWF model through a nonorographic gravity wave drag parameterization.” *Journal of Climate* 23.22, pp. 5905–5926. DOI: 10.1175/2010JCLI3490.1.

Pan, L. L., W. J. Randel, B. L. Gary, M. J. Mahoney, and E. J. Hintsa (2004). “Definitions and sharpness of the extratropical tropopause: A trace gas perspective.” *Journal of Geophysical Research D: Atmospheres* 109.23, pp. 1–11. DOI: 10.1029/2004JD004982.

Pan, L. L., K. P. Bowman, M. Shapiro, W. J. Randel, R. S. Gao, T. Campos, C. Davis, S. Schauffler, B. A. Ridley, J. C. Wei, and C. Barnet (2007). “Chemical behavior of the tropopause observed during the Stratosphere-Troposphere Analyses of Regional Transport experiment.” *Journal of Geophysical Research Atmospheres* 112.18, pp. 1–13. DOI: 10.1029/2007JD008645.

Pilch Kedzierski, R., K. Matthes, and K. Bumke (2015). “Synoptic-scale behavior of the extratropical tropopause inversion layer.” *Geophysical Research Letters* 42.22, pp. 10018–10026. DOI: 10.1002/2015GL066409.

Plougonven, R. and C. Snyder (2005). “Gravity waves excited by jets: Propagation versus generation.” *Geophysical Research Letters* 32.18, pp. 1–4. DOI: 10.1029/2005GL023730.

Plougonven, R. and F. Zhang (2014). “Internal gravity waves from atmospheric jets and fronts.” *Reviews of Geophysics* 52.1, pp. 33–76. DOI: https://doi.org/10.1002/2012RG000419.

Podglajen, A., T. P. Bui, J. M. Dean-Day, L. Pfister, E. J. Jensen, M. J. Alexander, A. Hertzog, B. Kärcher, R. Plougonven, and W. J. Randel (2017). “Small-scale wind fluctuations in the tropical tropopause layer from aircraft measurements: Occurrence, nature, and impact on vertical mixing." *Journal of the Atmospheric Sciences* 74.11, pp. 3847–3869. DOI: 10.1175/JAS-D-17-0010.1.

Preusse, P., M. Ern, P. Bechtold, S. D. Eckermann, S. Kalisch, Q. T. Trinh, and M. Riese (2014). "Characteristics of gravity waves resolved by ECMWF." *Atmospheric Chemistry and Physics* 14.19, pp. 10483–10508. DOI: 10.5194/acp-14-10483-2014.

Randel, W. J., F. Wu, and P. Forster (2007). "The Extratropical Tropopause Inversion Layer: Global Observations with GPS Data, and a Radiative Forcing Mechanism." *Journal of the Atmospheric Sciences* 64.12, pp. 4489–4496. DOI: 10.1175/2007JAS2412.1.

Reiss, N. M. and T. J. Corona (1977). "An investigation ot a Kelvin-Helmholtz Billow Cloud." *Bulletin of the American Meteorological Society* 58.2, pp. 159–162. DOI: https://doi.org/10.1175/1520-0477(1977)058<0159:AIOAKH>2.0.CO;2.

Reitebuch, O., D. Huber, and I. Nikolaus (2014). *ADM-Aeolus Algorithm Theoretical Basis Document ATBD.*

Reiter, E. R. (1964). "Nature and Observation of High-Level Turbulence, Especially in Clear Air." *Journal of Aircraft* 1.2, pp. 94–95. DOI: 10.2514/3.43559.

Reiter, E. R. (1969). "The Nature of Clear Air Turbulence: A Review." *Proceedings of a Symposium on Clear Air Turbulence and Its Detection.* Ed. by P. YH. and G. A. Boston, MA: Springer. DOI: https://doi.org/10.1007/978-1-4899-5615-6_2.

Riese, M., F. Ploeger, A. Rap, B. Vogel, P. Konopka, M. Dameris, and P. Forster (2012). "Impact of uncertainties in atmospheric mixing on simulated UTLS composition and related radiative effects." *Journal of Geophysical Research* 117.16, pp. 1–10. DOI: 10.1029/2012JD017751.

Roja Raman, M., V. V. Jagannadha Rao, M. Venkat Ratnam, M. Rajeevan, S. V. Rao, D. Narayana Rao, and N. Prabhakara Rao (2009). "Characteristics of the Tropical Easterly Jet: Long-term trends and their features during active and break monsoon phases." *Journal of Geophysical Research* 114.19, pp. 1–14. DOI: 10.1029/2009JD012065.

Saffin, L., S. Gray, J. Methven, and K. Williams (2017). "Processes maintaining tropopause sharpness in numerical models." *Journal of Geophysical Research* 122.18, pp. 9611–9627. DOI: https://doi.org/10.1002/2017JD026879.

Schäfler, A., A. Fix, and M. Wirth (2021). “Mixing at the extratropical tropopause as characterized by collocated airborne H_2O and O_3 lidar observations.” *Atmospheric Chemistry and Physics* 21.6, pp. 5217–5234. DOI: 10.5194/acp-21-5217-2021.

Schmidt, T., J. P. Cammas, H. G. Smit, S. Heise, J. Wickert, and A. Haser (2010). “Observational characteristics of the tropopause inversion layer derived from CHAMP/GRACE radio occultations and MOZAIC aircraft data.” *Journal of Geophysical Research* 115.24, pp. 1–16. DOI: 10.1029/2010JD014284.

Seidel, D. J., R. J. Ross, J. K. Angell, and G. C. Reid (2001). “Climatological characteristics of the tropical tropopause as revealed by radiosondes.” *Journal of Geophysical Research* 106.D8, pp. 7857–7878. DOI: 10.1029/2000JD900837.

Shapiro, M. A. (1976). “The role of turbulent heat flux in the generation of potential vorticity in the vicinity of upper-level jet stream systems.” *Monthly Weather Review* 104.7, pp. 892–906. DOI: https://doi.org/10.1175/1520-0493(1976)104<0892:TROTHF>2.0.CO;2.

Shapiro, M. A. (1980). “Turbulent Mixing within Tropopause Folds as a Mechanism for the Exchange of Chemical Constituents between the Stratosphere and Troposphere.” *Journal of Atmospheric Sciences* 37.5, pp. 994–1004. DOI: https://doi.org/10.1175/1520-0469(1980)037<0994:TMWTFA>2.0.CO;2.

Sharman, R. D., S. B. Trier, T. P. Lane, and J. D. Doyle (2012). “Sources and dynamics of turbulence in the upper troposphere and lower stratosphere : A review.” *Geophysical Research Letters* 39.21, pp. 1–9. DOI: 10.1029/2012GL051996.

Shaw, T. A., M. Baldwin, E. A. Barnes, R. Caballero, C. I. Garfinkel, Y. T. Hwang, C. Li, P. A. O’Gorman, G. Rivière, I. R. Simpson, and A. Voigt (2016). “Storm track processes and the opposing influences of climate change.” *Nature Geoscience* 9.9, pp. 656–664. DOI: 10.1038/ngeo2783.

Škerlak, B, M Sprenger, and H Wernli (2014). “A global climatology of stratosphere – troposphere exchange using the ERA-Interim data set from 1979 to 2011.” *Atmospheric Chemistry and Physics* 14.2, pp. 913–937. DOI: 10.5194/acp-14-913-2014.

Škerlak, B., M. Sprenger, S. Pfahl, E. Tyrlis, and H. Wernli (2015). “Tropopause folds in ERA-interim: Global climatology and relation to extreme weather events.” *Journal of Geophysical Research* 120.10, pp. 4860–4877. DOI: 10.1002/2014JD022787.

Spreitzer, E., R. Attinger, M. Boettcher, R. Forbes, H. Wernli, and H. Joos (2019). “Modification of potential vorticity near the tropopause by nonconservative processes in the ECMWF model." *Journal of the Atmospheric Sciences* 76.6, pp. 1709–1726. DOI: 10.1175/JAS-D-18-0295.1.

Sprenger, M. and H. Wernli (2003). "A northern hemispheric climatology of cross-tropopause exchange for the ERA15 time period (1979-1993)." *Journal of Geophysical Research Atmospheres* 108.12, pp. 1–14. DOI: 10.1029/2002jd002636.

Stohl, A. et al. (2003). "Stratosphere-troposphere exchange: A review, and what we have learned from STACCATO." *Journal of Geophysical Research* 108.12, pp. 1–15. DOI: 10.1029/2002jd002490.

Sullivan, S. C., K. A. Schiro, C. Stubenrauch, and P. Gentine (2019). "The Response of Tropical Organized Convection to El Niño Warming." *Journal of Geophysical Research* 124.15, pp. 8481–8500. DOI: 10.1029/2019JD031026.

Sunilkumar, S. V., A. Babu, and K. Parameswaran (2013). "Mean structure of the tropical tropopause and its variability over the Indian longitude sector." *Climate Dynamics* 40.5-6, pp. 1125–1140. DOI: 10.1007/s00382-012-1496-8.

Sunilkumar, S. V., M. Muhsin, K. Parameswaran, M. Venkat Ratnam, G. Ramkumar, K. Rajeev, B. V. Krishna Murthy, K. V. Sambhu Namboodiri, K. V. Subrahmanyam, K. Kishore Kumar, and S. Shankar Das (2015). "Characteristics of turbulence in the troposphere and lower stratosphere over the Indian Peninsula." *Journal of Atmospheric and Solar-Terrestrial Physics* 133, pp. 36–53. DOI: 10.1016/j.jastp.2015.07.015.

Tegen, I., P. Hollrig, M. Chin, I. Fung, D. Jacob, and J. Penner (1997). "Contribution of different aerosol species to the global aerosol extinction optical thickness: Estimates from model results." *Journal of Geophysical Research* 102, pp. 23895–23915. DOI: 10.1029/97JD01864.

Thorncroft, C. D., B. J. Hoskins, and M. E. McIntyre (1993). "Two paradigms of baroclinic-wave life-cycle behaviour." *Quarterly Journal of the Royal Meteorological Society* 119.509, pp. 17–55. DOI: 10.1002/qj.49711950903.

Tiedke, M. (1989). "A Comprehensive Mass Flux Scheme for Cumulus Parametrization in Large-Scale Models." *Monthly Weather Review* 117.8, pp. 1779–1800. DOI: https://doi.org/10.1175/1520-0493(1989)117<1779:ACMFSF>2.0.CO;2.

Tiedke, M. (1993). "Representation of Clouds in Large-Scale Models." *Monthly Weather Review* 121.11, pp. 3040–3061. DOI: https://doi.org/10.1175/1520-0493(1993)121<3040:ROCILS>2.0.CO;2.

Trier, S. B., R. D. Sharman, D. Muñoz-Esparza, and T. P. Lane (2020). “Environment and Mechanisms of Severe Turbulence in a Midlatitude Cyclone.” *Journal of the Atmospheric Sciences* 77.11, pp. 3869–3889. DOI: 10.1175/jas-d-20-0095.1.

Vasantha, B., M. V. Ratnam, K. Mohan, S. Kamala, D. N. Rao, and G. V. Rama (2002). “Characteristics of tropical easterly jet over Gadanki: Comparison with radiosonde and rawinsonde.” *Indian Journal of Radio and Space Physics* 31.3, pp. 130–139.

WMO (1957). “Meteorology — A threedimensional science: Second session of the Commission for Aerology.” *WMO Bulletin* VI.4, pp. 134–138.

Wargan, K. and L. Coy (2016). “Strengthening of the Tropopause Inversion Layer during the 2009 Sudden Stratospheric Warming: A MERRA-2 Study.” *Journal of the Atmospheric Sciences* 73.5, pp. 1871–1887. DOI: 10.1175/JAS-D-15-0333.1.

Webster, P. (2020). “Climatology of the Tropical Atmosphere and Oceans.” *Dynamics of the Tropical Atmosphere and Oceans*. John Wiley & Sons Ltd. Chap. 1, pp. 1–35. DOI: 10.1002/9781118648469.ch1.

Wernli, H. and C. Schwierz (2006). “Surface Cyclones in the ERA-40 Dataset (1958–2001). Part I: Novel Identification Method and Global Climatology.” *Journal of the Atmospheric Sciences* 63.10, pp. 2486–2507. DOI: 10.1175/JAS3766.1.

Whiteway, J. A., G. P. Klaassen, N. G. Bradshaw, and J. Hacker (2004). “Transition to turbulence in shear above the tropopause.” *Geophysical Research Letters* 31.2, pp. 2–5. DOI: 10.1029/2003GL018509.

Wirth, V. and J. Egger (1999). “Diagnosing extratropical synoptic-scale stratosphere-troposphere exchange: A case study.” *Quarterly Journal of the Royal Meteorological Society* 125.554, pp. 635–655. DOI: 10.1256/smsqj.55412.

Wirth, V. and T. Szabo (2007). “Sharpness of the extratropical tropopause in baroclinic life cycle experiments.” *Geophysical Research Letters* 34.2, pp. 10–13. DOI: 10.1029/2006GL028369.

Wirth, V. (2003). “Static Stability in the Extratropical Tropopause Region.” *Journal of the Atmospheric Sciences* 60.11, pp. 1395–1409. DOI: 10.1175/1520-0469(2003)060<1395:SSITET>2.0.CO;2.

Wirth, V. (2004). “A dynamical mechanism for tropopause sharpening.” *Meteorologische Zeitschrift* 13.6, pp. 477–484. DOI: 10.1127/0941-2948/2004/0013-0477.

Wu, S. and J. Sun (2017). "Variability in zonal location of winter East Asian jet stream." *International Journal of Climatology* 37.10, pp. 3753–3766. DOI: 10.1002/joc.4947.

Yang, S., K. M. Lau, and K. M. Kim (2002). "Variations of the East Asian jet stream and Asian-Pacific-American winter climate anomalies." *Journal of Climate* 15.1, pp. 306–325. DOI: 10.1175/1520-0442(2002)015<0306:voteaj>2.0.co;2.

Zanis, P., E. Gerasopoulos, A. Priller, C. Schnabel, A. Stohl, C. Zerefos, H. W. Gäggeler, L. Tobler, P. W. Kubik, H. J. Kanter, H. E. Scheel, J. Luterbacher, and M. Berger (2003). "An estimate of the impact of stratosphere-to-troposphere transport (STT) on the lower free tropospheric ozone over the Alps using 10Be and 7Be measurements." *Journal of Geophysical Research* 108.12, pp. 1–9. DOI: 10.1029/2002jd002604.

Zhang, Y., S. Zhang, C. Huang, K. Huang, and Y. Gong (2019). "The Tropopause Inversion Layer Interaction With the Inertial Gravity Wave Activities and Its Latitudinal Variability." *Journal of Geophysical Research* 124.14, pp. 7512–7522. DOI: 10.1029/2019JD030309.

Zhang, Y., S. Zhang, C. Huang, K. Huang, Y. Gong, and Q. Gan (2015). "The interaction between the tropopause inversion layer and the inertial gravity wave activities revealed by radiosonde observations at a midlatitude station Yehui." *Journal of Geophysical Research* 120.16, pp. 8099–8111. DOI: https://doi.org/10.1002/2015JD023115.

Zierl, B. and V. Wirth (1997). "The influence of radiation on tro- popause behavior and stratosphere-troposphere exchange in an upper tropospheric anticyclone." *Journal of Geophysical Research* 102.D20, pp. 23883–23894. DOI: https://doi.org/10.1029/97JD01667.

Zülicke, C. and D. Peters (2006). "Simulation of inertia-gravity waves in a poleward-breaking Rossby wave." *Journal of the Atmospheric Sciences* 63.12, pp. 3253–3276. DOI: 10.1175/JAS3805.1.

LIST OF FIGURES

Figure 1.1 Schematic of the northern hemispheric UTLS and its key features, adopted from Gettelman et al. (2011). Seven year temporal and zonal average (2002–2008), a) Winter (DJF), and b) summer (JJA) season. Color contour shows vertical temperature gradient ($\partial T / \partial z$, in steps of 0.5 K km^{-1}). The solid black line indicates the location of the LRT, and the dashed black lines the dynamic tropopause based on the PV threshold values 2 pvu and 6 pvu. Dotted black lines show isentropes, and solid thin black lines zonal mean zonal wind (u, in steps of 10 m s^{-1}). Data basis for the thermal structure are GPS radio occultation (RO) measurements, PV and wind are derived from ECMWF ERA Interim reanalysis fields 2

Figure 1.2 Zonal mean tropopause based averaged vertical profiles for JJA at 70° N, adopted from Hegglin et al. (2009). LRT relative vertical coordinate. Black line shows static stability (N^2, in 10^{-4} s^{-2}), blue line H_2O mixing ratio (ppmv, logarithmic as indicated), solid grey line O_3 (ppmv), and dashed grey line CO (ppmv, factor 20). For further details see Hegglin et al. (2009). 6

Figure 1.3 Schematic of the tropopause region in baroclinic waves, to illustrate the key processes and the central issue of this work. The TIL is indicated in orange, above the tropopause (thick silver line). The tropospheric ridge is dominated by the jet streak, large scale uplifting, and high reaching clouds. Gravity waves (emitted, reflected, refracted) are indicated as wavy arrows. Turbulence is indicated by circular arrows. An exemplary vertical profile of a tropospheric trace gas mixing ratio is shown at the right edge. Dashed (dotted) red arrows show long (short) wave outgoing (incoming) radiation. The dependency of the material change rate of N^2 on the vertical divergence of the vertical wind is stated in the top left corner. 16

Figure 2.1 Schematic diagram of the physical processes implemented in the ECMWF IFS model. Figure adapted from ECMWF (2016b). 20

Figure 2.2 Exemplary vertical cross section at 60° N on 26 August 2011, 18 UTC. a) Operational IFS analysis data. b) ERA Interim reanalysis data. Greyscale filled contour shows static stability (N^2, in s^{-2}). Yellow shaded contour indicates intense vertical wind shear $S^2 \geq 4 \cdot 10^{-4}$ s^{-2}. Black dotted lines show isentropes (Θ, in K). Blue dashed lines show cloud ice water content (*ciwc*, in steps of 10^{-5} kg kg^{-1}). Black cirlce markers indicate LRT altitude. 24

Figure 2.3 Flight paths of all 16 flights conducted during the WISE campaign from September–October 2017, including the transfer flights from and to Oberpfaffenhofen. Red dashed lines depict flight sections within 50 hPa vertical distance from the LRT, blue lines show the remaining flight sections. 27

Figure 2.4 Vertical profiles of UMAQS trace gas mixing ratio measurements during WISE RF07 on 28 September 2017, for a) CO and b) N_2O. Colour code indicates flight time since takeoff in hours. 29

Figure 3.1 Potential temperature Θ on $Q = 2$ pvu dynamic tropopause, for four time steps during the evolution of the baroclinic wave. Contour lines for $\Theta = 320$ and 340 K are highlighted in black. Path of minimum surface pressure during the four days is shown in all four panels, with the current location indicated by the red x, and the $MSLP$ minimum colour coded from 994 hPa (yellow) to 973 hPa (red). 33

Figure 3.2 a) Selection of UTLS features on 28 September 2017, 15 UTC from ECMWF IFS forecast data. Solid black line indicates $\Theta(Q = 2$ pvu$) = 320$ K dynamic tropopause potential temperature. Light grey filled contour indicates regions where the static stability N^2 in the LMS exceeds $6 \cdot 10^{-4}$ s^{-2}, dark grey filled contour where the vertical shear of the horizontal wind S^2_{max} exceeds $4 \cdot 10^{-4}$ s^{-2} within 1 km vertical distance from the local LRT. RF07 flight path from 14:20–15:15 UTC is indicated in blue, HALO location at 15 UTC by blue star, MSLP minimum by grey x. b) Vertical cross section at 55° N, filled contour shows horizontal wind speed, dotted lines isentropes, black dots LRT altitude, black squares dynamic tropopause altitude, and blue star location of the DLR HALO at 15 UTC. Black filled contour indicates $N^2 \geq 6 \cdot 10^{-4}$ s^{-2}, and grey filled contour regions of enhanced vertical wind shear $S^2 \geq 4 \cdot 10^{-4}$ s^{-2} 34

Figure 3.3 Flight pattern of research flight RF07. Colour code indicates flight altitude, black solid line shows surface projection of the flight path. The black dotted lines indicate the location, the viewing direction and the opening angle of photographies of Kelvin Helmholtz billows that were taken at 15:03 UTC and are analysed in Section 3.1.3. 35

Figure 3.4 Time series of measured and model-derived quantities during WISE RF07 on 28 September 2017. a) Flight altitude (black solid, in km) and model-derived quantities from IFS forecast data, showing LRT altitude as black circle markers (z(LRT), in km), and $Q = 2$ pvu dynamic tropopause altitude as black square markers ($z(Q = 2$ pvu), in km). b) Black line shows potential temperature along flightpath (Θ, in K), blue line shows zonal wind component (u, in m s^{-1}), and red line meridional wind component (v, in m s^{-1}). Bright colors show IFS forecast data interpolated along the flight path, flat colors show in situ measured quantities. 36

Figure 3.5 a) Height-time cross section along the flight path on FL380, derived from hourly IFS forecast fields, between 14:15 and 15:15 UTC on 28 September 2017. Vertical wind shear S^2 (color-coded), static stability isoline $N^2 = 6 \cdot 10^{-4}$ s^{-2} (black solid), flight altitude (black dotted), isentropes Θ (grey dashed), cloud ice water content *ciwc* (blue dashed in steps of $5 \cdot 10^{-6}$ kg kg^{-1}), horizontal wind speed $\sqrt{u^2 + v^2}$ (green solid, starting at 40 m s^{-1} and in steps of 10 m s^{-1}), and LRT altitude (black circles). b) Static stability N^2 (solid red), vertical wind shear S^2 (red dashed), and Richardson number *Ri* (black solid, logarithmic scale). Quantities along flight path derived from IFS forecast data. c) Measured potential temperature (black solid, BAHAMAS, in K), N_2O mixing ratio (green, UMAQS, in ppbv), and CO mixing ratio (blue, UMAQS, in ppbv). 37

Figure 3.6 Tracer-tracer correlation of the mixing ratios of N_2O and CO that were measured during WISE RF07. Grey circle markers indicate mixing ratio pairs for the whole research flight, color coded cross markers show measurements for the time from 14:20–14:54 UTC, with the color indicating the measured potential temperature Θ. 38

Figure 3.7 Correlation analysis of the measurements presented in Fig. 3.5c. a) - c): CO-Θ correlation for the three successive time periods during the flight leg on FL380, with the time since 14:00 UTC colour-coded. d) - f): CO-N_2O tracer-tracer correlation, with the colour code indicating the measured potential temperature Θ in K. 39

Figure 3.8 a) Power spectral density of the meridional wind along the flight path during WISE RF07, comparison between BAHAMAS measurements (grey solid) and IFS forecast data (black solid). Red line indicates $f = 2 \cdot 10^{-3}$ s^{-1}. b) Divergence of the horizontal wind $\vec{\nabla} \cdot \vec{u}_h$ at 11.5 km altitude on 28 September 2017, 15 UTC. Black line indicates the flight path of the research aircraft between 14:20–15:15 UTC. 40

Figure 3.9 a) Composite of the the two post-processed photographs taken at 15:03:43 and 15:03:47 UTC. The displacement is such that the Kelvin-Helmholtz billows align horizontally. b) Schematic of the geometric analysis. Red lines show the cameras field of view and the image plane, blue dashed lines indicate the Kelvin-Helmholtz billows at two time steps. 43

Figure 3.10 Excerpt of the synoptic situation during WISE RF12. a) Potential temperature Θ on the $Q = 2$ pvu dynamic tropopause, on 12 October 2017, at 12 UTC. Contour lines for $\Theta = 320$ and 340 K are highlighted in black. Mean sea level pressure overlay in grey contour lines (MSLP, beginning at 965 hPa in the cyclone centre and in steps of 10 hPa). Flight path of WISE RF12 indicated in red. b) Height-time cross section along the flight path, indicating the Richardson number (Ri, color coded), flight altitude (z_{HALO}, black dotted line), dynamic tropopause ($z(Q = 2$ pvu), black dash-dotted), LRT altitude (z(LRT), circle markers), an isoline of the static stability ($N^2 = 6 \cdot 10^{-4}$ s^{-2}, grey solid line), and isolines of the horizontal wind (u_h, in m s^{-1}, grey dashed lines). All quantities derived from IFS forecast data. 45

Figure 3.11 Quasi-vertical profiles during the descent from 11:55 to 11:57 UTC during WISE RF12. Solid thick lines show IFS forecast profiles, dashed lines measurements or measurement-derived variables, and solid thin lines 20 second running mean of measurements. a) Air temperature (T, in K). b) Horizontal wind components, u in green, v in magenta ((u/v), in m s^{-1}). c) Vertical shear of the horizontal wind in blue (S^2, in s^{-2}) and static stability in red (N^2, in s^{-2}), on a logarithmic scale. Richardson number in black (Ri, dimensionless). Vertical blue line indicates $Ri = 0.25$. The potential temperature derived from the BAHAMAS measurements is indicated on the rightmost vertical axis. 46

Figure 3.12 Tracer-tracer correlation plot for CO and N_2O during WISE RF12. Grey markers show all measurements within the axis limits, color coded markers only measurements during the descent from 11:55:00 to 11:57:51 UTC. Color code indicates potential temperature at the location of each mixing ratio measurement (Θ, in K). . 47

Figure 4.1 a) All 139 cyclone tracks identified in the analysed region. Crosses indicate the location of MSLP along each track. b) Schematic of the size of the analysed region (dark grey) in comparison to the full sphere, as well as the size of a rotated spheric polar coordinate system (orange) with $\mathbf{\Phi}_{max} = 15°$ radius. The dark grey semi-transperent upright plane illustrates (with exaggerated vertical extent) the vertical cross-section aligned from north to south as displayed in Fig. 4.11c and d. 56

Figure 4.2 Evolution of an LC2 resembling baroclinic wave breaking event, 24 hours before (first column), at (middle column), and 24 hours after the time of maximum surface cyclone intensity (last column). a) MSLP ($\leq$ 1013 hPa solid lines, $>$ 1013 hPa dashed lines, in steps of 5 hPa). b) Isentropic potential vorticity (IPV) at $\Theta = 330$ K ($Q(\Theta = 330$ K$)$, in pvu), and horizontal wind speed at 200 hPa (u_h, red solid lines from 45 ms^{-1} in steps of 15 ms^{-1}). 58

Figure 4.3 As in Fig. 4.2, for a different set of UTLS measures. a) Maximum in static stability within 3 km above the LRT (N^2, in s^{-2}). b) Maximum in vertical shear of the horizontal wind within 1 km vertical distance from the LRT (S^2, in s^{-2}). c) Relative vorticity at LRT altitude (ζ_{rel}, in s^{-1}). d) Richardson number minimum within 3 km above the LRT (Ri_{min}) 59

Figure 4.4 a) Vertical cross section on 14 October 2014, 06 UTC at 18° W. Filled contour shows vertical shear of the horizontal wind (S^2, in s^{-2}), black dotted lines isentropes (Θ in K), grey filled contour indicates static stability $N^2 \geq 6 \cdot 10^{-4}$ s^{-2}, blue (red) lines zonal (meridional) wind isotachs (u, v, in ms^{-1}, dashed lines for negative values). Circle markers indicate LRT altitude (z(LRT) in km). b) Two-dimensional histogram of N^2 and S^2 within 3 km above the LRT, on 14 October 2014, 06 UTC and for the region displayed in Fig. 4.3. Colorbar indicates count of grid volumes in the respective N^2-S^2 bin. Black dashed line indicates $Ri = 1/4$. Red dashed line see Section 4.2.1 60

Figure 4.5 As in Fig. 4.2, for the LC1 resembling baroclinic wave breaking event, 24 hours before (first column), at (middle column), and 24 hours after the time of maximum surface cyclone intensity. 61

Figure 4.6 As in Fig. 4.3, for the LC1 resembling baroclinic wave breaking event, 24 hours before (first column), at (middle column), and 24 hours after the time of maximum surface cyclone intensity. 62

Figure 4.7 Comparison of the horizontal wind and the geostrophic wind, for the time of maximum cyclone intensity of the LC1 case study, i.e., 17 October 2014, 18 UTC. a) Zonal wind at 300 hPa (u, in ms^{-1}). b) Geostrophic zonal wind at 300 hPa (u_g, in ms^{-1}). c) Meridional cross section at 17° W. Vertical wind shear color coded (S^2, in s^{-2}), isentropes black dotted (Θ, 315 K, 320 K, 330 K, 350 K), LRT altitude black circle markers, and zonal wind -10 ms^{-1} (blue dashed) and 0 ms^{-1} respectively 30 ms^{-1} (blue solid) isotachs. d) Thermal wind shear color coded (S^2, in s^{-2}), and zonal geostrophic wind -10 ms^{-1} (blue dashed) and 0 ms^{-1} respectively 30 ms^{-1} (blue solid) isotachs. Isentropes and LRT as in panel c. 63

Figure 4.8 As in Fig. 4.2 and Fig. 4.3, for the stratospheric cutoff resulting from the LC1 resembling baroclinic wave breaking event. 64

Figure 4.9 Composites of UTLS features derived from subsets of the tracked cyclones, displayed over a radius of 15° around the cyclone centre at the time of maximum surface cyclone intensity. Top column for the 76 strong cyclones with $\text{MSLP}_{min} \leq 990$ hPa, middle column for the 30 very strong cyclones with $\text{MSLP}_{min} \leq 980$ hPa, and bottom row for the 54 weak cyclones with $\text{MSLP}_{min} > 990$ hPa. a) Potential Vorticity at $\Theta = 330$ K ($Q(\Theta = 330\text{ K})$, in pvu). b) Relative vorticity at LRT altitude (ζ_{rel}, in s^{-1}). 66

Figure 4.10 As in Fig. 4.9, for different UTLS features. a) Maximum in static stability within 3 km above the LRT (N^2, in s^{-2}). b) Maximum in vertical shear of the horizontal wind within 1 km vertical distance from the LRT (S^2, in s^{-2}), and d) relative vorticity at LRT altitude (ζ_{rel}, in s^{-1}). 67

Figure 4.11 a) and b): Quasi-horizontal composites derived from the 76 strong cyclones with $\text{MSLP}_{min} \leq 990$ hPa. a) Mean and b) median value of the minimum Richardson numbers within 3 km above the local LRT ($\overline{Ri}_{min}$, (-)). c) and d): Northward aligned vertical cross sections through the cylcone centre, LRT-based average for the 76 strong cyclones, with mean LRT altitude restored. c) Static stability as filled contour (N^2, in s^{-2}), isentropes as black dotted (Θ, in K), LRT altitude as circle markers (z(LRT), in km), potential vorticity isolines as red dotted ($Q = 2$ pvu and $Q = 3$ pvu), and cloud ice water content as blue dashed lines (CIWC, beginning at $5 \cdot 10^{-6}$ kg/kg and in same steps). d) Vertical shear of the horizontal wind as filled contour (S^2, in s^{-2}), zonal (meridional) wind component in blue (red), positive values solid, negative values dashed lines (u and v, in m/s), dashed white contour $N^2 = 6 \cdot 10^{-4}\ \text{s}^{-2}$ isoline, and LRT altitude as in c). 68

Figure 5.1 Synoptic situation on 11 September 2017, 00 UTC over the northern hemisphere. Color contour shows potential temperature at the LRT ($\Theta(LRT)$, in K), black lines isotachs of the horizontal wind at 200 hPa (from 30 ms^{-1} in steps of 15 ms^{-1}). Magenta shaded areas indicate regions with $S^2 \geq S_t^2$ between 1 km below and 2 km above the local LRT. Dashed white lines indicate the location of the vertical cross-sections in Fig. 5.2. . . 75

Figure 5.2 Vertical cross section at the latitudes indicated in Fig. 5.1, i.e., a) 120° W, b) 60° W, and c) 100° E. Color contour shows zonal wind speed (u, in ms^{-1}), and magenta contour indicates region of $S^2 \geq 4 \cdot 10^{-4}$ s^{-2}. Black circle markers indicate LRT altitude, and black dotted lines isolines of the potential temperature (Θ, in K). . . 76

Figure 5.3 Relative occurrence frequency of $S^2 > S_t^2$, zonally averaged over the northern hemisphere on 11 September 2017, at 00 UTC. Logarithmic occurrence frequency contour. Data vertically binned in $dz = 500$ m. a) Absolute height distribution. Dashed black line indicates the effect of the 1.5 km above orography cut-off. b) LRT-relative vertical coordinates. Dashed black line shows LRT altitude. c) As in b) with the average LRT altitude of the vertical profiles with $S^2 \geq S_t^2$ restored. . . . 77

Figure 5.4 Northern hemispheric occurrence frequency distribution of grid volumes that exhibit strong vertical wind shear $S^2 \geq S_t^2$, from 1 January 2008 to 31 December 2017. Logarithmic frequency contour, vertically binned with $dz = 500$ m. a) Geometric altitude as the vertical coordinate. Solid bold black line indicates mean LRT altitude for all 10 years and the whole northern hemisphere. Dashed thin black line indicates the effect of the 1.5 km above orography cut-off. White solid (dotted) line indicates regions where negative (positive) vertical wind shear makes for 75 % of the counts. b) As in panel a, with LRT-relative vertical coordinate and with mean LRT altitude for profiles with $S^2 \geq S_t^2$ restored (dashed bold black line). Solid bold black line as in panel a. c) As in panel b but from $0° - 20°$ N with the cold point tropopause (CPT) as a reference altitude, and north of 20° N with the dynamic tropopause ($Q = 2$ pvu) as a reference altitude. 78

Figure 5.5 Schematical vertical cross section of the tropopause-based averaging method. Left part shows exemplary situation at the tropopause break, right part the key measures after tropopause-based averaging. Black lines indicate the LRT, grey lines the dynamic tropopause. Blue lines show isotachs, and the yellow and blue regions indicate regions of enhanced vertical wind shear above and below the jet core. 79

Figure 5.6 Occurrence frequency distribution of $S^2 \geq S_t^2$ between 1 km below and 2 km above the local LRT and in the northern hemisphere. Averaged over 10 years from 2008 to 2017 for a) DJF, b) MAM, c) JJA and d) SON. Red solid lines indicate isolines of the horizontal wind at 200 hPa, starting at 30 m s^{-1} in steps of 30 m s^{-1}. 81

Figure 5.7 a) and b): Seasonal ten year temporally and zonally averaged dynamic tropopause potential temperature ($\overline{\Theta}(Q = 2$ pvu), in K). c) and d): Seasonal ten year temporally and zonally averaged LRT potential temperature ($\overline{\Theta}$(LRT), in K). Solid lines show mean values, dashed lines interannual standard deviation. Left column North Atlantic region (80° W–0° W). Right column Northeast Pacific region (180° W–120° W). Red dot in a indicates $\overline{\Theta}(Q = 2$ pvu) which Fig. 5.8 is referring to. 83

Figure 5.8 Occurrence frequency of $S^2 \geq S_t^2$ within 1 km below and 2 km above the LRT, depending on $\Theta(Q = 2$ pvu). Blue histogram shows occurrence frequency distribution of $\Theta(Q = 2$ pvu) at 50° N during MAM 2008 – 2017 and averaged over 180° – 120° W. $\Theta(Q = 2$ pvu) in 1 K bins. Dashed black line shows mean value $\overline{\Theta}(Q = 2$ pvu) = 316.4 K (red dot in Fig. 5.6b). Solid black line shows occurrence frequency for $S^2 \geq S_t^2$ in 1 km vertical distance from the LRT within the $\Theta(Q = 2$ pvu) bins. . 84

Figure 5.9 Occurrence frequency of $\Delta\Theta(Q = 2$ pvu$)$ deviations from $\overline{\Theta}(Q = 2$ pvu$)$ as in Fig. 5.8c, with meridional dependency. Dashed (solid) red lines indicate occurrence frequencies isolines, beginning at 0.5 % (1.0 %) and in steps of 1.0 %. Colour contour shows occurrence frequency for $S^2 \geq S_t^2$ between 1 km below and 2 km above the LRT within the $\Theta(Q = 2$ pvu$)$ bins. a) to d) DJF MAM JJA SON over the North Atlantic region. e) to h) Same for the Northeast Pacific region. Blue dashed line in f) indicates location of Fig. 5.8. 85

Figure 5.10 a) Black solid contour lines indicate occurrence frequencies for $S^2 \geq S_t^2$ in 1 km vertical distance from the LRT, for SON and over the North Atlantic. Contour lines start at 5 % and progress in steps of 5 % (compare Fig. 5.9d). Circle markers show overlay of measurements from the WISE campaign in the $\Delta\Theta(Q = 2$ pvu$)$-Latitude space, at reduced frequency for reasons of clarity. Black markers indicate the flight leg from 14:36 to 14:54 UTC during WISE RF07. Red (blue) markers indicate measurements from all WISE flights in regions with occurrence frequencies for $S^2 \geq S_t^2$ larger than (smaller than) 15 %, that were performed within 30 K vertical distance above the tropopause. The 15 % contour is higlighted in magenta. Histograms indicate the relative distribution of measurements performed within each $\Delta\Theta(Q = 2$ pvu$)$-bin, respectively each latitude bin. b) N_2O-CO tracer-tracer correlation for the flight data displayed in panel a. The descent at 11:55 UTC during WISE RF12 is indicated in white circle markers (These measurements were performed north of 60° N, and thus beyond the range of panel a. 86

Figure 5.11 Vertical cross sections of ten year average tropopause properties between 60° E and 180° E longitude: a) winter (DJF) and b) summer (JJA). Upper panels: Solid black line shows $\overline{\Theta}$(LRT) for the zonal region. Blue solid line shows zonally averaged occurrence frequency for $S^2 \geq S_t^2$ between 1 km below and 2 km above the local LRT, and dashed solid line depicts $\overline{\Theta}$(LRT) for such vertical profiles. Bottom panels show interannual standard deviation for every measure. The standard deviation of the occurrence frequency displays absolute percentage values. 88

Figure 5.12 As in Fig. 5.6a for a smaller geographical section, averaged over selected DJF seasons of a) west-located EAJS core years (2008, 2011 and 2012), and b) averagely located EAJS core years (2009 and 2010). For further destails see text and Wu and Sun (2017). 89

Figure 5.13 a) Comparison of the Oceanic Niño sea surface temperature anomaly Index for DJF (ONI, blue graph) with the strong shear occurrence frequency during DJF averaged over the region from 100° E to 130° E and from the equator to 10° N (red graph). The values for January–February 2008 and December 2017 are included (light red). ONI values from https://www.noaa.gov/. b) and c) Temporal mean of a zonal cross-section at the equator, averaged in geometric height coordinates, for the two consecutive DJF seasons 2009/10 and 2010/11. Color contour shows mean zonal wind component (u, in m s^{-1}). Red solid lines show the 10 % and the 50 % isolines of occurrence frequencies for $S^2 \geq S_t^2$. Blue solid lines show the 10 % and the 50 % isolines of occurrence frequencies for $N^2 \geq 4 \cdot 10^{-4}$ s^{-2}. Black circle markers indicate LRT altitude, and black solid lines show isolines of potential temperature (Θ, in K). Light blue dashed lines indicate the isolines of 70 % and 85 % relative humidity over ice. 91

Figure 5.14 a) Relative occurrence frequency distribution of N^2-S^2 pairs in the region between the LRT and 3 km above, for all daily northern hemispheric ERA5 fields from 2008–2017. Logarithmic occurrence frequency color scale. Red dashed line indicates $S^2 = S_t^2$. Dashed black lines indicate the Richardson numbers 0.25, 0.5, 1.0, 2.0 and 4.0. b) Histogram of the relative distribution of Richardson numbers associated with the data displayed in panel a in bins of $\Delta Ri = 0.25$. Orange bars show Ri for grid volumes with $S^2 \geq S_t^2$, and blue bars for the remaining grid volumes between the LRT and 3 km above. Dotted black line indicates $Ri = 1$. 95

LIST OF TABLES

Table 1 Central features of IFS versions used in this work. . . . 21
Table 2 Overview of the research flights conducted during the WISE campaign. The flights which are analysed in Chapter 3 are highlighted in blue. 28

ACRONYMS

ACE-FTS	Atmospheric Chemistry Experiment Fourier Transform Spectrometer
AN	Analysis
BAHAMAS	Basic HALO Measurement and Sensor System
CAPE	Convective available potential energy
CAT	Clear air turbulence
CPT	Cold point tropopause
Cy36r3	IFS model cycle identifier
DJF	December January February
DLR	Deutsches Zentrum für Luft- und Raumfahrt
DNS	Direct numerical simulation
EAJS	East Asian jet stream
EASM	East Asian summer monsoon
ECMWF	European Centre for Medium-Range Weather Forecast
ENSO	El Niño Southern Oscillation
ERA5	Fifth generation of atmospheric reanalysis from the ECMWF
ERA40	Second generation of atmospheric reanalysis from the ECMWF
ERA-Interim	Third generation of atmospheric reanalysis from the ECMWF
ESA	European Space Agency
ESRL	Earth System Research Laboratories
Exif	Exchangeable image file format
ExTL	Extratropcial transition layer

FC	Forecast
FL	Flight level
FZ	Forschungszentrum
GLORIA	Gimballed Limb Observer for Radiance Imaging of the Atmosphere instrument
GPS	Global positioning system
HALO	High Atitude LOng range aircraft
IAGOS	In-service Aircraft for a Global Observing System
IFS	Integrated Forecast System
IGW	Inertia gravity waves
IMILAST	Intercomparison of Mid Latitude Storm Diagnostics
IPV	Isentropic potential vorticity
JGU	Johannes Gutenberg-University
JJA	June July August
KHI	Kelvin-Helmholtz instability
KIT	Karlsruhe Institute for Technology
LC1	Life cycle 1
LC2	Life cycle 2
LMS	Lowermost stratosphere
LRT	Lapse rate tropopause
MAM	March April May
McICA	Monte Carlo Independent Column Approximation
MLT	Mesosphere-lower thermosphere
MST	Mesosphere-stratosphere-troposphere
NCAR	National Center for Atmospheric Research
NOAA	National Oceanic and Atmospheric Administration

ONI	Oceanic Niño sea surface temperature anomaly Index
PFJ	Polar-front jet
PV	Potential vorticity
RF	Research flight
RO	Radio Occultation
RRTM	Rapid Radiative Transfer Model
SON	September October November
STE	Stratosphere-troposphere exchange
STJ	Subtropical jet
STT	Stratosphere to troposphere transport
SVC	Sub-visible cirrus
TEJ	Tropical easterly jet
TIL	Tropopause inversion layer
TST	Troposphere to stratosphere transport
TTL	Tropical tropopause layer
TSL	Tropopause wind shear layer
UMAQS	University of Mainz Airborne Quantum Cascade Laser Spectrometer
UTLS	Upper troposphere lower stratosphere
WACCM	Whole Atmosphere Community Climate Model
WCB	Warm conveyor belt
WISE	Wave driven ISentropic Exchange
WMO	World Meteorological Organization

PHYSICAL SYMBOLS

Symbol	**Unit**	**Description**
$ciwc$	$\mathrm{kg\,kg^{-1}}$	Cloud ice water content
c_p	$\mathrm{J\,kg^{-1}\,K^{-1}}$	Specific heat capacity of air for constant pressure
f	$\mathrm{s^{-1}}$	Frequency
$\vec{F}$	$\mathrm{m\,s^{-2}}$	Vector of non-conservative forces
$\mathcal{F}$	$\mathrm{W\,m^{-2}}$	Radiative flux
f_{LTG}	-	Stability function after Louis, Tiedtke and Geleyn
g	$\mathrm{m\,s^{-1}}$	Gravitational acceleration
K_ϵ	$\mathrm{m^2\,s^{-1}}$	Eddy diffusivity
l	m	Mixing length
m	$\mathrm{m^{-1}}$	Vertical wave number
$MSLP$	Pa	Mean sea level pressure
N^2	$\mathrm{s^{-2}}$	Brunt-Väisälä Frequency
p	Pa	Pressure
q	$\mathrm{kg\,kg^{-1}}$	Specific humidity
q_i	$\mathrm{kg\,kg^{-1}}$	Specific ice water
q_l	$\mathrm{kg\,kg^{-1}}$	Specific liquid water
Q	$\mathrm{m^2\,s^{-1}\,K\,kg^{-1}}$	Potential vorticity
R_d	$\mathrm{J\,kg^{-1}\,K^{-1}}$	Specific gas constant for dry air
r	m	Radius
r_0	m	Cressman filter adius
Ri	-	Richardson number

Ri_c	-	Critical Richardson number
S^2	s^{-2}	Vertical shear of the horizontal wind
S_t^2	s^{-2}	Threshold of S^2
T	K	Temperature
t	s	Time
TAS	$\mathrm{m\,s}^{-1}$	True air speed
u	$\mathrm{m\,s}^{-1}$	Zonal wind component
u_h	$\mathrm{m\,s}^{-1}$	Horizontal wind speed
$\vec{u}$	$\mathrm{m\,s}^{-1}$	Vector of the threedimensional wind
v	$\mathrm{m\,s}^{-1}$	Meridional wind component
$\vec{v}_g$	$\mathrm{m\,s}^{-1}$	Vector of the geostrophic wind
w	$\mathrm{m\,s}^{-1}$	Vertical wind component
$\vec{x}$	degree	Vector of geographic location of MSLP minimum
z	m	Altitude
Γ	$\mathrm{K\,km}^{-1}$	Lapse rate
ζ_{rel}	s^{-1}	Relative vorticity
$\vec{\eta}$	s^{-1}	Vector of absolute vorticity
θ	K	Potential temperature
λ_h	m	Horizontal wave length
ρ	$\mathrm{kg\,m}^{-3}$	Density
Φ	$\mathrm{m}^2\,\mathrm{s}^{-2}$	Geopotential
Φ_{max}	degree	Radius of the rotated polar coordinate system
ω	$\mathrm{Pa\,s}^{-1}$	Vertical velocity in pressure coordinates
$\vec{\Omega}$	s^{-1}	Vector of angular vorticity of the earth

LIST OF PUBLICATIONS

The following articles have been published during my time as doctoral student and are related to the PhD.

PEER REVIEWED PUBLICATIONS

Kaluza, T., Kunkel, D., and Hoor, P. (2019): Composite analysis of the tropopause inversion layer in extratropical baroclinic waves, *Atmospheric Chemistry and Physics*, 19, 1-22, https://doi.org/10.5194/acp-19-6621-2019

Kunkel, D., Hoor, P., **Kaluza, T.**, Ungerman, J., Kluschat, B., Giez, A., Lachnitt, H.-C., Kaufmann, M., Riese, M. (2019): Evidence of small-scale quasi-isentropic mixing in ridges of extratropical baroclinic waves, *Atmospheric Chemistry and Physics*, 19, 12607-12630, https://doi.org/10.5194/acp-19-12607-2019

Kaluza, T., Kunkel, D., and Hoor, P. (2021): On the occurrence of enhanced vertical wind shear in the tropopause region: A 10-year ERA5 northern hemispheric study, *Weather and Climate Dynamics*, https://doi.org/10.5194/wcd-2-631-2021

DANKSAGUNG

Die Danksagung ist in der digitalen Version aus Gründen des Datenschutzes nicht enthalten. Mein Dank gilt allen die mich während der Promotionszeit unterstützt haben, und insbesondere den Menschen die meinen Werdegang bis zu diesem Punkt unterstützt und mit ermöglicht haben.